BIG EASY PROSPECT: A WELL-PRESERVED LOW-SULFIDATION EPITHERMAL Au-Ag SYSTEM IN THE LATE NEOPROTEROZOIC, NEWFOUNDLAND, CANADA

By

© Andrés Eduardo Junco Rojas

B.Sc. Universidad Nacional de Colombia – Bogotá, 2016

A thesis submitted to the School of Graduate Studies in partial fulfillment of the requirements for the degree of

Master of Science – Earth Sciences (Geology)

in the Graduate Academic Unit of Earth Sciences

Memorial University of Newfoundland

November 2022

St. John's – Newfoundland and Labrador

Canada

Dedication

To my mother.

Acknowledgments

I thank Professor Dr. Graham D. Layne for giving me the excellent opportunity to work under his supervision and guidance at the Memorial University of Newfoundland. Thanks to Silver Spruce Resources Inc. and Cartier Iron Corporation for providing diamond drill cores and lithogeochemistry analytical results from samples collected in drilling programs carried out in 2011, 2012, 2014, 2018, and 2021. Dylan Goudie from the CREAIT MAF facility at MUN is thanked for his advice and support for the SEM-MLA analysis.

Thanks to the Graduate Student Fellowship Program (GSFP) of the Society of Economic Geologists (SEG) and Memorial University of Newfoundland for granting me the SGS Fellowship Award and the Dr. Alfred K. Snelgrove Graduate Scholarship Earth Sciences, respectively. Special thanks to Dr. Steve Piercey and Dr. Luke Beranek for their teaching and knowledge provided during graduate courses, and for correcting me and advising me in improving my writing skills.

I give special thanks to my mother for her emotional support, unconditional love, always believing in me, and supporting me when I decided to set out on this adventure. I am very grateful to all my friends in Bogotá for their company and advice despite the distance.

This project was funded by an NSERC Discovery Grant (RGPIN/005037-2017) held by Dr. Graham D. Layne.

Table of Contents

List of Tables

List of Figures

Thesis abstract

The Big Easy prospect is a low-sulfidation epithermal gold occurrence of Neoproterozoic age in the Burin-Bonavista region of Newfoundland, Canada. Mineralization is predominantly hosted in epiclastic rocks of the Musgravetown Group. This well-preserved system lies within the tectonostratigraphic Avalon Zone and is dated as Late Neoproterozoic (ca. 573 Ma). Previous work suggests that the most prospective period for epithermal deposits within the Neoproterozoic Avalon Zone is from ca. 620 Ma until the nominal end of the Neoproterozoic at 541 Ma. This period encompassed three episodes of arc magmatism, as recognized in the Burin Peninsula region: ca. 620 Ma (e.g., Broad Island Group), ca. 585 – 570 Ma (Marystown and Musgravetown Groups), and ca. 565 Ma (Long Harbour Group). Big Easy appears to have been associated with the 585 – 570 Ma episode, as were a number of volcanic/volcaniclastic-hosted occurrences in this region.

The mineralization at Big Easy is subdivided here into four different styles of discrete Au- and Ag-bearing veins, containing characteristic ore mineral assemblages: Type I) Electrum dominant (High Au) – (pyrite + electrum ± sphalerite); Type II) High Au:Ag – (pyrite + electrum + native silver + naumannite + acanthite ± aguilarite ± chalcopyrite ± uytenbogaardtite); Type III) Ginguro (High Ag:Au) – (native silver + acanthite + electrum ± pyrite ± aguilarite ± chalcopyrite ± freibergite-tetrahedrite,); and Type IV) Molybdenite-rich (molybdenite + native silver + acanthite ± pyrite ± chalcopyrite ± sphalerite). Gold is mainly deported in type I and II veins as electrum observable in grains attached to, or enclosed by, pyrite crystals, or as rare uytenbogaardtite (Ag3AuS2).

Geological and numerical models using existing drill hole data exhibit a strong spatial correlation between gold, silver, molybdenum, and arsenic distributions, and illustrate the predominant ambient hydrothermal alteration zone present in the preserved epithermal system. Strong correlations from PCA analysis, Pearson correlation values, and drill hole correlation analysis are observed for Au-Ag, but also for Mo-As. Mo and As in minor concentrations may be contained within pyrite in veins and pyritized selvages directly associated with Au-Ag mineralization. However, the more likely interpretation is that they are a signature of the extensive silicification and intense pyritization evident in the host epiclastic rocks, which predates the ore mineralization. Fluid inclusion microthermometry and SEM imaging were used to characterize the mineralogical and textural features of each vein style, as well as the estimated fluid temperatures and salinities (from 124.7 °C to 321.15 °C, and from 0.18 to 2.74 wt.% NaCl eq., respectively).

Low-sulfidation Au-Ag deposits are a significant source of these metals globally. Big Easy, and other occurrences in the Avalon Zone, are a testament that mineral exploration for preserved epithermal deposits hosted in pre-Cenozoic rocks should not be neglected. New insights documented in this thesis will be useful for future exploration programs in the area. Big Easy represents a highly prospective epithermal system within the Avalon Zone and is one of the most important examples of this deposit type recognized in the Burin-Bonavista region to date.

Chapter 1: General introduction

1.1 BIG EASY PROSPECT: A HISTORICAL REVIEW.

The Big Easy prospect is located approximately 18 km northwest of the town of Clarenville, in the Thorburn Lake area, to the southwest of the Bonavista Peninsula in Newfoundland, Canada (Fig. 1.1). The site is part of the Avalon Zone, a Pan-African terrane situated in the most northeastern section of the Appalachian Orogen (O'Brien et al., 1983).

Historically, the rocks in the property were described by F.D. Anderson in 1962 during a regional mapping program carried out by the Department of Mines and Technical Surveys of the Geological Survey of Canada (Jenness, 1962; p. 51). Subsequently, geological maps, geochemistry and stratigraphy, and structural analysis of the Thorburn Lake area were made by Eric Hussey as part of his MSc thesis (Geology of the Clode Sound Area - Hussey, 1979). Provincial government mapping was subsequently carried out by Sean O'Brien, covering a large area from northeast of Henry's Pond to Bonavista Bay (O'Brien, 1987, 1993).

Samples with anomalous Au and Ag concentrations were collected by prospectors Alex Turpin and Colin Kendall in early 2009. These samples, mainly from along the northeast shore of Grassy Pond, returned mean values of 248 ppb Au, with a high of 997 ppb (1 g/t), and 9.9 ppm Ag with a high of 145 ppm (145 g/t) (Dimmell, 2015). In 2010, follow-up exploration activities, including an IP/Resistivity survey, trenches, channels, and outcrop sampling, were carried out under the management of Silver Spruce Resources. Au values of 30 to 2083 ppb, with a mean of 72 ppb

were obtained from a set of 121 channel samples. Additional anomalies in silver (Ag), molybdenum (Mo), and bismuth (Bi), as well as elevated potassium (K) concentrations, were also noted in these samples. The highest Au value (2083 ppb) occurred in a 0.7 m channel sample from a shallow subcrop of silicified sediments (Dimmell, 2015).

Diamond drilling started in 2011 under the direction of Silver Spruce Resources Inc., with seven holes totaling 1577 m. Significant gold and silver values obtained in this program included 2.5 g/t Au and 74.1 g/t Ag over 7 m, including 1.5 m of 6.05 g/t Au and 174 g/t Ag, and 1 m of 6.04 g/t Au and 114 g/t Ag (DeLazzer & Dimmell, 2012; Dimmell, 2015). Phase 2 of this program commenced in 2012 with five new holes totaling 1070 m, including one that transected a brecciated quartz-adularia vein zone identified previously during Phase 1. Significant intersections included 1.3 g/t Au and 36.7 g/t Ag over 8.7 m, including 7.9 g/t Au and 130 g/t Ag over 1.2 m (Dimmell, 2012, 2015). Native silver was first recognized in this core by Graham Layne in 2012 (G. Layne, pers.comm.), and subsequent SEM work by Layne and B.Sc. student Matthew Clarke (Clarke, 2013) verified the presence of a pyrite-native silver-acanthite “ginguro” (silver-black) assemblage within crenulate veins, a feature characteristic of many low sulfidation epithermal deposits. The final diamond drilling program by Silver Spruce Resources - Phase 3 - was carried out in 2014, consisting of 7 holes totaling 1391 m. High ("bonanza") grades were encountered in narrow quartz-adularia (QA) veins associated with strongly altered, silicified zones and containing ginguro-style banding. The highest values were 10.75 g/t Au and 1094 g/t Ag over 0.2 m (Dimmell, 2015). Drilling exploration programs were accompanied by prospecting/stream sediment geochemistry, soil geochemistry sampling, and IP/airborne surveys.

Additionally, a Bachelor of Science (Honours) thesis and two Master of Science theses that included studies of the host lithologies, regional geological context and interpreted geophysical signature of the Big Easy prospect were completed at Memorial University of Newfoundland between 2013 and 2017 (Clarke, 2013; Ferguson, 2017; Wall, 2017). Clarke (2013) obtained an ID-TIMS U-Pb zircon age of 566 ± 2 Ma from a mafic-intermediate dyke containing abundant plagioclase with pervasive chlorite alteration, cross-cutting a silicified pebble conglomerate that hosts vein mineralization. This is interpreted as a minimum age constraint on the Big Easy precious metal mineralization. Clarke (2013) also contains a reconnaissance overview of ore mineralogy, host lithologies, and alteration mineralogy using petrography, visible/infrared spectroscopy (VIRS)(Terraspec^{TM}), Scanning Electron Microscopy, and Energy Dispersive X-Ray Spectroscopy (SEM-EDX). Findings included the predominance of green pebble conglomerate with volcanic affinity as the predominant host rock, containing extensive hydrothermal brecciation; alteration assemblages dominated by silica (quartz/chalcedony), with minor amounts of adularia, sericite/illite, and chlorite; and ore mineralization containing disseminated pyrite, chalcopyrite, sphalerite, acanthite, native silver, arsenopyrite, Au-rich electrum, Ag-selenides, and minor Ag-tellurides (Clarke, 2013). These initial results were interpreted as indicating that Big Easy represents a low-sulfidation epithermal system of Neoproterozoic age (Clarke, 2013).

Ferguson (2017) undertook a detailed regional survey of the plutonic and volcanic rocks associated with epithermal prospects in the Avalon Zone in the Burin Peninsula region. As part of this study, a U-Pb zircon age of 573 ± 2.7 Ma was obtained on a sample of flow-banded rhyolite (West Princess Rhyolite) from the Musgravetown Group, collected immediately north of the Big Easy prospect. These results suggested that, like most of the epithermal prospects in this region, Big

Easy may also be affiliated with the 570-580 Ma plutonism of the Swift Current and Burin Knee Intrusive Suites (Ferguson, 2017).

Wall (2017) performed a geophysical study of the Big Easy property to delineate alteration zones. The approach included a high-resolution ground magnetic survey, ground-based gravity survey, RTK elevation survey, and ground-penetrating radar (GPR) survey. As a result, new maps of inferred/interpreted alteration zones, and geophysical features attributed to mafic dykes, were generated as a tool to inform future exploration and drilling programs (Wall, 2017). Main findings included an inferred basaltic dyke to the west of the property ("Basalt" in Figure 1.1), interpreted as affiliated with the Bull Arm Formation and represented by a magnetic high with a trend and amplitude similar to other mafic dykes in the study area. These dykes are spatially and directionally related to the main faulting features (Big Easy Fault and Grassy Pond Fault in Figure 1.1), and suggest a potentially extended eastern boundary to the currently recognized zone(s) of epithermal alteration (Fig. 1.1). Further, intense epithermal alteration zone may not extend contiguously as far south as previously believed, but may extend some distance to the north. To the southeast, a small extension of the Big Easy Main Alteration Zone (Fig. 1.1) is interpreted to be located at the intersection between the Grassy Pond Fault and NE trending mafic dykes (Fig. 1.1). To the north, the alteration zone extends to the north side of the Bottle Ponds, close to the intersection between Grassy Pond and Big Easy faults (Fig. 1.1). Finally, based on residual gravity data, the alteration zone is modelled as extending from the surface to a depth of approximately 250 meters, although somewhat shallower toward the north (Wall, 2017).

In late 2017, the property was acquired by Cartier Iron Corporation, which commenced a new drilling program in late 2018. Efforts were focused on testing the potential downdip extension of the Big Easy mineralization in the Main Alteration Zone. This downdip extension is implied by a chargeability anomaly, detected during a new geophysical survey by Cartier Iron, which appears to be stronger with depth (Cartier Iron Corporation, 2018). Several intersections, in combination grading 0.11 g/t Au and 2.65 g/t Ag over 180.4 m, were obtained by drilling on the western edge of the Central Anomaly (Fig. 1.1) located 1.8 km south of the original Big Easy Main Showing area, extending the strike length of the known alteration zone (Cartier Iron Corporation, 2018a). This long intersection of elevated Au-Ag, and the observed chargeability anomaly, are interpreted to reflect an extensive zone of epithermal alteration and mineralization of 200 m in width and at least 250 m in depth (Cartier Iron Corporation, 2018). More recently, diamond drilling was carried out in June 2021, and intersected elevated Au-Ag - 0.62 g/t Au and 16.12 g/t Ag - over 13.0 m in the core silicification of the original Big Easy Main Alteration Zone (Cartier Iron Corporation, 2021; Fig. 1.1). This intersection corresponds to an extensive zone of silicification, up to 200 m wide, with epithermal gold-silver mineralization in the Central Anomaly area. Moreover, a 39.5 km line of additional IP surveys recently completed outline major new targets in the Sleigh Pond Grid area in the southern part of claims (Cartier Iron Corporation, 2021).

1.2 CHARACTERISTICS OF EPITHERMAL AU-AG DEPOSITS: A BRIEF INTRODUCTION.

Epithermal Au-Ag deposits develop at temperatures between 150 °C and 300 °C, at depths in the crust of 1 to 2 km, and lithostatic pressures not exceeding several hundreds of bars (White &

Hedenquist, 1995; Fig. 1.2). It is common to find them within recognizable volcanic structures such as calderas and dome complexes, in host rocks ranging from felsic to intermediate composition. Mineralization is most often concentrated in vein networks, and these are usually controlled by tectonic processes that generate faults and fractures, permitting the flow of hydrothermal fluids and fostering subsequent precipitation of metals due to abrupt physicochemical changes with decreasing depth or confinement pressure. Epithermal deposits are spatially associated with subductive plate boundaries, typically during continental arc development, as well as less frequently, with island arcs and extensional back-arcs (Goldfarb et al., 2004; Hedenquist et al., 2000).

Two end-member styles of epithermal deposits are well described in the literature, high-sulfidation and low-sulfidation, and the characteristic features of each member have been clearly defined and differentiated (e.g., Hedenquist et al., 2000; White & Hedenquist, 1990, 1995; summarized in Table 1.1). The contrasting characteristics are closely related to different fluid chemistry, pH, temperature and pressure profiles, depth in the crust, and timing of formation during magmatism. These differences yield distinctive mineral assemblages, textures, and alteration zones. In general, high-sulfidation deposits are contemporaneous with active subduction and calc-alkaline arc volcanism, and are situated above and proximal to the parent pluton. In contrast, low-sulfidation deposits tend to form during the immediate post-subduction stage. They are often recognized as related to the late extension or rifting of the arc and are often laterally displaced from the parent intrusions. For example, they can occur as far as 5-6 km away from the parent pluton (White & Hedenquist, 1990).

Epithermal precious metal deposits tend to be hosted in felsic to intermediate subaerial volcanic rocks generated mainly in convergent tectonic settings of continental-oceanic or oceanic-oceanic plate subduction (White & Hedenquist, 1990), and this tendency is evident in the global distribution of this deposit type (Fig. 1.3). Volcanic-hosted epithermal deposits occur worldwide in both modern and ancient subduction zones (e.g., Comstock Lode in Nevada, Vikre, 1989; Fresnillo District in Mexico, Simmons, 1991; Creede Mining District in Colorado, USA, Barton et al., 2000; Plumlee, 1994). There is also a smaller sub-class of (usually low-sulfidation) epithermal deposits hosted within associated epiclastic sediments derived from this same style of volcanism.

Late extensional environments are often present in these same tectonic settings, producing back-arc rifting and subsequent development of back-arc basins. Previous literature argued that these basins were predominantly submarine and were therefore not likely to host epithermal deposits (White & Hedenquist, 1990). However, there is now broad agreement that epithermal deposits can occur during the later stages of volcanic arc evolution within incipient extensional back-arc basins (Prihatmoko & Idrus, 2020; Sillitoe, 1993; Vamvoukakis et al., 2005).

1.3 BIG EASY AS A LOW-SULFIDATION EPITHERMAL DEPOSIT.

Based on field observations, analytical and laboratory research, and technical reports compiling results from exploration campaigns conducted by Silver Spruce Resources Inc. and Cartier Iron Corporation, Big Easy is considered to be a low-sulfidation epithermal gold-silver deposit (Cartier

Iron Corporation, 2018b; Clarke, 2013; DeLazzer & Dimmell, 2012; Dimmell, 2012, 2013, 2015; Sparkes et al., 2016).

Features characteristic of the low-sulfidation epithermal deposit type are summarized in Figure 1.2 and Table 1.1. Many of the broad characteristics of these deposits are evident from the previous work at Big Easy: The predominance of gold-silver mineralization, with high Ag/Au ratios, and low base metal contents in the mineralized veins. Dominant adularia and sericite alteration, (minor) carbonate veins as a result of neutral pH hydrothermal fluids, siliceous sinter formed at or near surface, and intra-vein boiling features such as crustiform and colloform textures. Detailed analytical results, images, and other results supporting the classification of Big Easy as a low-sulfidation epithermal occurrence are presented in Chapter 3.

1.4 EXAMPLES OF EPICLASTIC-HOSTED EPITHERMAL DEPOSITS.

Most epithermal precious metal deposits are hosted within primary volcanic rocks (often volcaniclastic lithologies) and/or within contemporaneous shallow dykes that intrude these volcanic rocks. However, there are important examples that are wholly or partially hosted within epiclastic facies of the related volcanic terrane. In this context, the term epiclastic is taken to mean a lithology predominantly comprised of fragments liberated from pre-existing volcanic rock by "weathering or erosion and transported from their place of origin by gravity, air, water, or ice" (Schmid, 1981). It is implied that they are subsequently deposited in lakes (including caldera filling lakes) or other structural depressions. Unlike the other epithermal deposits recognized to date in the Burin Peninsula region, Big Easy is hosted within a sandstone-conglomerate unit, rather than

within volcanic-volcaniclastic rocks. Although they are sparsely documented in the published literature compared to volcanic-volcaniclastic-hosted examples, the comparison to other known sediment-hosted epithermal deposits globally is potentially important to understanding and exploring the Big Easy deposit. Therefore, the most usefully comparable occurrences and deposits are introduced here as background information.

Epithermal deposits associated with intra-volcanic (intra-caldera) basins, back-arc extensions, or structural depressions are sometimes hosted in clastic and epiclastic sediments. Feiss et al. (1993) discuss examples from the Neoproterozoic Carolina terrane of southern Appalachian Piedmont. In this region, the epithermal gold-pyrite mineralization is found at the volcano-sedimentary transition and covered by epiclastic rift-fill sedimentary rocks derived from active and remnant arcs. Within this terrane lies one of the best-studied example of an epithermal deposit hosted in silicified metasedimentary rocks - the Haile Gold Mine (Kershaw, South Carolina), which is found along the boundary between the metavolcanic and overlying metasedimentary rocks (Mobley et al., 2014). Gold mineralization is hosted by silicified laminated metasiltstones and metavolcanic rocks, and is associated with pyrite, pyrrhotite, and molybdenite (Table 2.1). Gold is sometimes associated with detached quartz-sulfide veins within the silicified metasiltstone (Berry et al., 2016; Mobley et al., 2014). Although it is metamorphosed and polydeformed, the Haile deposit has several important similarities to Big Easy (Table 2.1), including the silicified epiclastic sedimentary host rocks, and a comparable late Neoproterozoic age (548.7 ± 2.0 Ma) within the Carolina Terrane.

A limited occurrence of epiclastic-hosted mineralization has recently been reported by Layne et al. (2019) from the Late Neoproterozoic Mira terrane of Cape Breton Island, Nova Scotia. The Mira terrane represents a southeastern extension of the Newfoundland Avalon Zone. Samples collected for the 2019 study from Big Hill Road Quarry include a facies comprising epiclastic sandstone and conglomerate with polymictic volcanic clasts. Parts of this facies are highly silicified and contain abundant fine-grained pyrite and sparse overgrowths of galena (Layne et al., 2019). Accordingly, the Big Hill Road Quarry facies resembles the silicified and pyritized epiclastic conglomerates which host the Big Easy low-sulfidation Au-Ag prospect (Clarke, 2013; Ferguson, 2017). Correlative ages for this portion of the Mira terrane imply that the Big Hill Road mineralization may have been penecontemporaneous with the Big Easy prospect (ca. 575-560 Ma) and occurred in a very similar paleoenvironment (Layne et al., 2019).

A younger example of a significant and well-documented epiclastic-related precious metal deposit is Fruta Del Norte located in southeastern Ecuador (Leary et al., 2016; Lipiec et al., 2016; Stewart et al., 2017). Fruta Del Norte gold-silver vein-stockwork system is considered a low- to intermediate-sulfidation style mineralization with an overlying siliceous sinter horizon (Table 1.2; Stewart et al., 2017) that is analogous to that described at Big Easy (Clarke, 2013;). Mineralization is concentrated in either colloform-crustiform base metal-poor quartz-adularia-calcite veins or base metal-rich quartz veins with disseminated marcasite and silicified chalcedony (Stewart et al., 2017). Fine to coarse visible gold is notably widespread, which gives rise to bonanza gold grades associated with quartz, chalcedony, carbonate, and sulfide gangue, and is hosted in volcanic rocks of the Piuntza unit. These comprise fine-grained basaltic andesite to andesite flows, and monzonite, tonalite, and granodiorite rocks from the Zamora batholith (Leary et al., 2016).

Although Fruta Del Norte is not hosted directly within epiclastic rocks, the deposit exhibits an extensive and evolved epiclastic cover with similarities to the host sediments and sinter at Big Easy, which is associated with the same system that fostered vein-stockwork in the underlying volcanics (Table 1.2). Similar to the Big Easy prospect, the exceptional preservation of the mineralization is a distinctive feature. It can be explained due to the deposition of a thick sequence of barren conglomerates on top of the still-active epithermal paleosurface (Stewart et al., 2017).

1.5 GOALS AND SCOPE OF THESIS STUDY.

The general goal of this research study was to describe and interpret the tectonic and mineralogic features of the Big Easy prospect. Big Easy is a recent discovery, which is still in the early stages of exploration and research. However, the system is extremely well preserved, a potential Au-Ag deposit, and highly informative in assessing the paleoenvironment during the Late Neoproterozoic in the Avalon Zone. It is one of the key examples of known epithermal Au-Ag deposits in the western Avalon Zone – the others being the Heritage Prospect (Pt. May, NL) and the Hickey's Pond Prospect (50 km SSW of Clarenville, NL).

Specific aims of this study include:

- Examine in detail the conformability of Big Easy with general models for low-sulfidation epithermal deposits.
- Define any variation in vein styles and generations (especially vein generation(s) with high Au:Ag such as those important at Fruta Del Norte, and that may be comparable to the Late Neoproterozoic deposit at Haile).

- Use Scanning Electron Microscopy (SEM) analysis to provide a more detailed understanding of mineralogy and assemblages in the system. SEM-BSE (Back Scattered Electron) imaging and SEM-EDX (X-ray spectroscopy) microanalysis deployed to supplement observations made using petrography, as well as to identify ore assemblages, provide semi-quantitative chemical composition information, and describe the texture and paragenesis of mineral phases whose size is smaller than the resolution of an optical microscope.
- Use PCA analysis and geological modelling of the existing core assay database to interrogate: 1) Elemental correlations related to specific vein generations; 2) Provide a 3-dimensional model of the geology, alteration zoning, and Au-Ag envelopes of the system based on drilling to date.
- Use fluid inclusion (FI) microthermometry to define the temperature and salinity ranges of the vein mineralization.
- Combine these observations and results to provide a basis to compare and contrast Big Easy with significant and well-studied epithermal deposits, especially Haile and Fruta Del Norte, which represent significant, well-documented deposits that have substantial components of epiclastic rocks in their host stratigraphy.
- Combine these observations to guide future exploration (including interpretation of drill data).

The scope of the thesis was limited by pandemic restrictions that began in early 2020 and extended through 2021. Limitations included: 1) restricted field access to the project area, drilling activities, and most recent DDH core; and, 2) postponed and limited sample and laboratory equipment access

on the Memorial University campus during 2020 and 2021. The study thus relied heavily on drill core samples previously archived at Memorial University from the Silver Spruce drilling campaigns, and data records from core logging and assay/geochemical analysis by previous and current exploration operators (Silver Spruce Resources and Cartier Iron). Petrography, SEM-BSE-EDX studies, Fluid Inclusion (FI) microthermometry, and other laboratory analyses were conducted at Memorial University, as pandemic restrictions allowed.

1.6 STRUCTURE OF THESIS.

The thesis is presented in four chapters:

- Chapter 1 (this chapter): General introduction.

This chapter provides a historical context of exploration and research activities carried out to date on the Big Easy property., Soil and rock sampling, drilling programs, geophysical prospecting, geochemical assays, and research studies on the property, introduces the existing knowledge base for the prospect.

A brief introduction to epithermal Au-Ag deposits includes geological features (such as temperature, pressure, tectonic setting, host rocks, mineralogy, etc.), and a general classification of the two end-member styles of epithermal deposits.

Finally, a description of Big Easy as an example of a low-sulfidation Au-Ag epithermal deposit, along with a brief comparison with other epiclastic-hosted deposits, especially Haile Gold Deposit in South Carolina and Fruta Del Norte in Ecuador is provided.

- Chapter 2: Geological setting, stratigraphy, and tectonic environment of the Big Easy low-sulfidation epithermal system: Implications for the paleoenvironment of gold-silver mineralization.

This chapter contains information related to the geological setting and tectonic processes that affected the evolution and development of Big Easy. Additionally, a detailed description of the stratigraphy, rock units, host rocks, and pertinent geochronological data is provided. The tectonic evolution is summarized step by step from the amalgamation of the supercontinent Rodinia and development of the primitive Avalonian arc, to the covering of the hydrothermal system by a sedimentary succession in a back-arc basin.

Significant characteristics of the prospect, such as age, epiclastic host rocks, system preservation, and tectonic evolution, are explained and compared with other similar examples globally.

- Chapter 3: Mineralogy, geochemistry, and hydrothermal alteration of the Big Easy low-sulfidation epithermal system: Constraints from SEM-MLA imaging, geological modeling, and fluid inclusion microanalysis.

This chapter contains most of the new data and detailed interpretations generated during the thesis research study. Characterization and description of four distinct mineralized vein types represent the pivotal result in this chapter. A detailed description of the mineral assemblages and paragenetic sequences were generated, using microanalytical techniques. PCA analysis provided elemental correlations related to these specific mineral assemblages, and it was a powerful tool to analyze the large database of geochemical results from core samples obtained during the drilling programs. Using the geochemical results for Au, Ag, Mo and As from core samples, 3D numerical models were generated to visualize the envelopes with higher concentrations of these elements.

Additionally, a fluid inclusion microanalysis study of selected samples from different vein types is presented, enumerating the temperature and salinity ranges of vein-forming fluids.

- Chapter 4: Summary of conclusions and recommendations for future work.

This final chapter includes a summary of the most important conclusions of the research study, as well as some recommendations for additional analyses, modelling, and techniques that could be used in future research work to complement our understanding of Big Easy and other epithermal systems in the Avalon Zone, and globally.

1.7 REFERENCES.

Barton, P. B., Rye, R. O., & Bethke, P. M. (2000). Evolution of the Creede caldera and its relation to mineralization in the Creede mining district, Colorado. Special Paper of the Geological Society of America, 346, 301–326. https://doi.org/10.1130/0-8137-2346-9.301

Berry, J. M., Mobley, R. M., Gillon, K. A., Yogodzinski, G. M., & Bates, C. C. (2016). A Neoproterozoic epithermal gold deposit - The Haile gold mine, South Carolina, USA. GSA Field Guides, 42(01), 1–8. https://doi.org/10.1130/2016.0042(01)

Cartier Iron Corporation. (2018a). Cartier Iron Intersects Major New Anomalous Alteration Zone Grading 0.11 g Au/t and 2.65 g Ag/t over 180.4 m at Big Easy in Newfoundland. Press release, 5p. https://cartieriron.com/news/news/cartier-iron-intersects-major-new-anomalous-altera-1670190/

Cartier Iron Corporation. (2018b). NI 43-101 Technical Report for the Big Easy Property, Newfoundland. Press release, 3p. https://cartieriron.com/news/news/cartier-files-ni-43-101-technical-reportfor-the-bi-1517114/

Cartier Iron Corporation. (2021). Cartier Iron Diamond Drilling Intersects 0.62 g Au/t and 16.12 g Ag/t over 13.0m in Low Sulphidation Epithermal Au-Ag System at the Big Easy Gold Project, Newfoundland. Press release, 6p. https://cartieriron.com/news/news/cartier-iron-diamond-drilling-intersects-0-62-g-au-2243444/

Clarke, M. (2013). Host lithologies, breccia development, alteration and gold mineralization at the Big Easy prospect, B.Sc. (Honours) Thesis, Memorial University of Newfoundland, 85p.

DeLazzer, A., & Dimmell, P. (2012). Report on 2011 Exploration (Diamond Drilling, Trench/DDH Reclamation, Compilation) on the Big Easy (BE) Property, Licences 13446M, 16633M, 17315M, 17342M, 19157M, NTS 2D/1,8, Thorburn Lake Area, Eastern Newfoundland for Silver Spruce Resources Inc., 181p.

Dimmell, P. (2012). Report on 2012 Exploration (Prospecting, Stream Sediment Geochemistry, Airborne Geophysics, Diamond Drilling, Compilation) on the Big Easy (BE) Property, Licences 13446M, 16633M, 17315M, 17342M, 19157M, NTS 2D/1, 8, Thorburn Lake Area, Eastern Newfoundland for Silver Spruce Resources Inc., 271p.

Dimmell, P. (2013). Report on 2013 Exploration (Field Geological Evaluation, Geophysical/Geological, Compilation) on the Big Easy (BE) Property, Licences 13446M, 16633M, 17315M, 20943M, 20944M, NTS 2D/1, 8, Thorburn Lake Area, Eastern Newfoundland for Silver Spruce Resources Inc., 139p.

Dimmell, P. (2015). Report on 2014 Exploration (Prospecting, Soil Sediment Geochemistry, Diamond Drilling, Compilation) on the Big Easy (BE) Property, Licences 13446M, 16633M, 23023M, NTS 2D/1, 8, Thorburn Lake Area, Eastern Newfoundland for Silver Spruce Resources Inc., 154p.

Feiss, P. G., Vance, R. K., & Wesolowski, D. J. (1993). Volcanic rock-hosted gold and base-metal mineralization associated with Neoproterozoic-early Paleozoic back-arc extension in the Carolina terrane, southern Appalachian Piedmont. Geology, 21(5), 439–442. https://doi.org/10.1130/0091-7613(1993)021<0439:VRHGAB>2.3.CO;2

Ferguson, S. A. (2017). Late Neoproterozoic epithermal-style Au mineralization of the Burin Peninsula, Newfoundland: U-Pb geochronology and deposit characteristics, M.Sc. Thesis, Memorial University of Newfoundland, 394p.

Foley, N. (2001). Remnant colloform pyrite at the Haile Gold Deposit, South Carolina: A textural key to genesis. Economic Geology, 96, 891–902. https://doi.org/10.2113/96.4.891

Goldfarb, R. J., Bradley, D., & Leach, D. L. (2004). Secular variation in economic geology. Economic Geology: Bulletin of the Society of Economic Geologists, 105(3), 459–465. https://doi.org/10.1016/B0-12-369396-9/00458-5

Hedenquist, J., Arribas, A., & Gonzalez-Urien, E. (2000). Exploration for Epithermal Gold Deposits. Reviews in Economic Geology, 13(l), 245–277.

Hussey, E. M. (1979). The stratigraphy, structure and petrochemistry of the Clode Sound map area, northwestern Avalon Zone, Newfoundland, M.Sc. Thesis, Memorial University of Newfoundland, 381p.

Jenness, S. E. (1962). Paper 63-1 Summary of Research: Field, 1962. Geological Survey of Canada: Department of Mines and Technical Surveys, 81p.

Layne, G.D., Barr, S.M. and White, C.E. 2019. Metallogeny of the Avalonian Mira terrane, southeastern Cape Breton Island, Nova Scotia: A preliminary study, Geoscience and Mines Branch Report of Activities 2018-2019, Nova Scotia Department of Natural Resources, Report ME 2019-001, p. 23-33.

Leary, S., Sillitoe, R. H., Stewart, P. W., Roa, K. J., & Nicolson, B. E. (2016). Discovery, geology, and origin of the Fruta del Norte epithermal gold-silver deposit, southeastern Ecuador. Economic Geology, 111(5), 1043–1072. https://doi.org/10.2113/econgeo.111.5.1043

Lipiec, I., Brown, J., Allard, S., Malasa, C., Searston, S., Watts, B., Sepúlveda, A., Maycock, T., & Ross, D. (2016). Fruta del Norte Project, Ecuador. NI 43-101 Technical Report on Feasibility Study, Lundin Gold, 385p. https://www.lundingold.com/site/assets/files/1652/2016-04-30_technical_report-en.pdf

Mobley, R. M., Yogodzinski, G. M., Creaser, R. A., & Berry, J. M. (2014). Geologic history and timing of mineralization at the Haile gold mine, South Carolina. Economic Geology, 109(7), 1863–1881. https://doi.org/10.2113/econgeo.109.7.1863

O'Brien, S. J. (1987). Geology of the Eastport (West Half) map area, Bonavista Bay, Newfoundland. Current Research: Newfoundland Geological Survey, Newfoundland Department of Mines and Energy, 87(1), 257–270.

O'Brien, S. J. (1993). A preliminary account of geological investigations in the Clode Sound – Goose Bay region, Bonavista Bay, Newfoundland (NTS 2C/5 NW and 2D/8 NE). Current Research: Newfoundland Geological Survey, Newfoundland Department of Mines and Energy, 93(1), 293–309.

O'Brien, S. J., Wardle, R. J., & King, A. F. (1983). The Avalon Zone: A Pan-African terrane in the Appalachian Orogen of Canada. Geological Journal, 18(3), 195–222. https://doi.org/10.1002/gj.3350180302

Plumlee, G. S. (1994). Fluid chemistry evolution and mineral deposition in the main-stage Creede epithermal system. Economic Geology, 89(8), 1860–1882. https://doi.org/10.2113/gsecongeo.89.8.1860

Prihatmoko, S., & Idrus, A. (2020). Low-sulfidation epithermal gold deposits in Java, Indonesia: Characteristics and linkage to the volcano-tectonic setting. Ore Geology Reviews, 121(April 2019), 103490. https://doi.org/10.1016/j.oregeorev.2020.103490

Schmid, R. (1981). Descriptive nomenclature and classification of pyroclastic deposits and fragments: Recommendations of the lUGS Subcommission on the Systematics of Igneous Rocks. Geology, 9, 41–43. https://doi.org/10.1007/bf01822152

Sillitoe, R. H. (1993). Geotectonic setting of western Pacific gold deposits. Basement Tectonics 8, 8, 665–678. https://doi.org/10.1007/978-94-011-1614-5_47

Simmons, S. F. (1991). Hydrologic Implications of Alteration and Fluid Inclusion Studies in the Fresnillo District, Mexico: Evidence for a Brine Reservoir and a Descending Water Table during the Formation of Hydrothermal Ag-Pb-Zn Orebodies. Economic Geology, 86(8), 1579–1601. https://doi.org/10.2113/gsecongeo.86.8.1579

Sparkes, G. W., Ferguson, S. A., Layne, G. D., Dunning, G. R., Brien, S. J. O., & Langille, A. (2016). The nature and timing of Neoproterozoic high-sulphidation gold mineralization from the Newfoundland Avalon Zone: Insights from new U-Pb ages, ore petrography and spectral data from the Hickey's Pond prospect. Current Research, Newfoundland and Labrador Department of Natural Resources Geological Survey, Report 16-1, p. 91-116.

Stewart, P. W., Stein, H. J., & Roa, K. (2017). Fruta del Norte, Ecuador : a completely preserved Late Jurassic epithermal gold-silver deposit. Proceedings of the 14th Biennial SGA Meeting, 20-23 August 2017, Quebec City, Canada, 99–102.

Taylor, B.E., 2007, Epithermal gold deposits, in Goodfellow, W.D., ed., Mineral Deposits of Canada: A Synthesis of Major Deposit-Types, District Metallogeny, the Evolution of Geological Provinces, and Exploration Methods: Geological Association of Canada, Mineral Deposits Division, Special Publication No. 5, p. 113-139.

Vamvoukakis, C., Seymour, K. S., Kouli, M., Lamera, S., & Denes, G. (2005). Investigation of non pristine volcanic structures acting as probable hosts to epithermal gold mineralization in the back arc region of the active Aegean arc, using combined satellite imagery and field data: examples from Lesvos volcanic terrain. In Developments in Volcanology (Vol. 7, Issue C). Elsevier B.V. https://doi.org/10.1016/S1871-644X(05)80048-8

Vikre, P. G. (1989). Fluid-Mineral Relations in the Comstock Lode. Economic Geology, 84(6), 1574–1613. https://doi.org/10.2113/gsecongeo.84.6.1574

Wall, A. (2017). Delineating the alteration zone at the Big Easy Prospect using geophysical methods, M.Sc. Thesis, Memorial University of Newfoundland, 174p.

White, N. C., & Hedenquist, J. W. (1990). Epithermal environments and styles of mineralization: Variations and their causes, and guidelines for exploration. Journal of Geochemical Exploration, 36(1–3), 445–474. https://doi.org/10.1016/0375-6742(90)90063-G

White, N. C., & Hedenquist, J. W. (1995). Epithermal gold deposits: Styles, characteristics and exploration. SEG Newsletter, 23, 8–13.

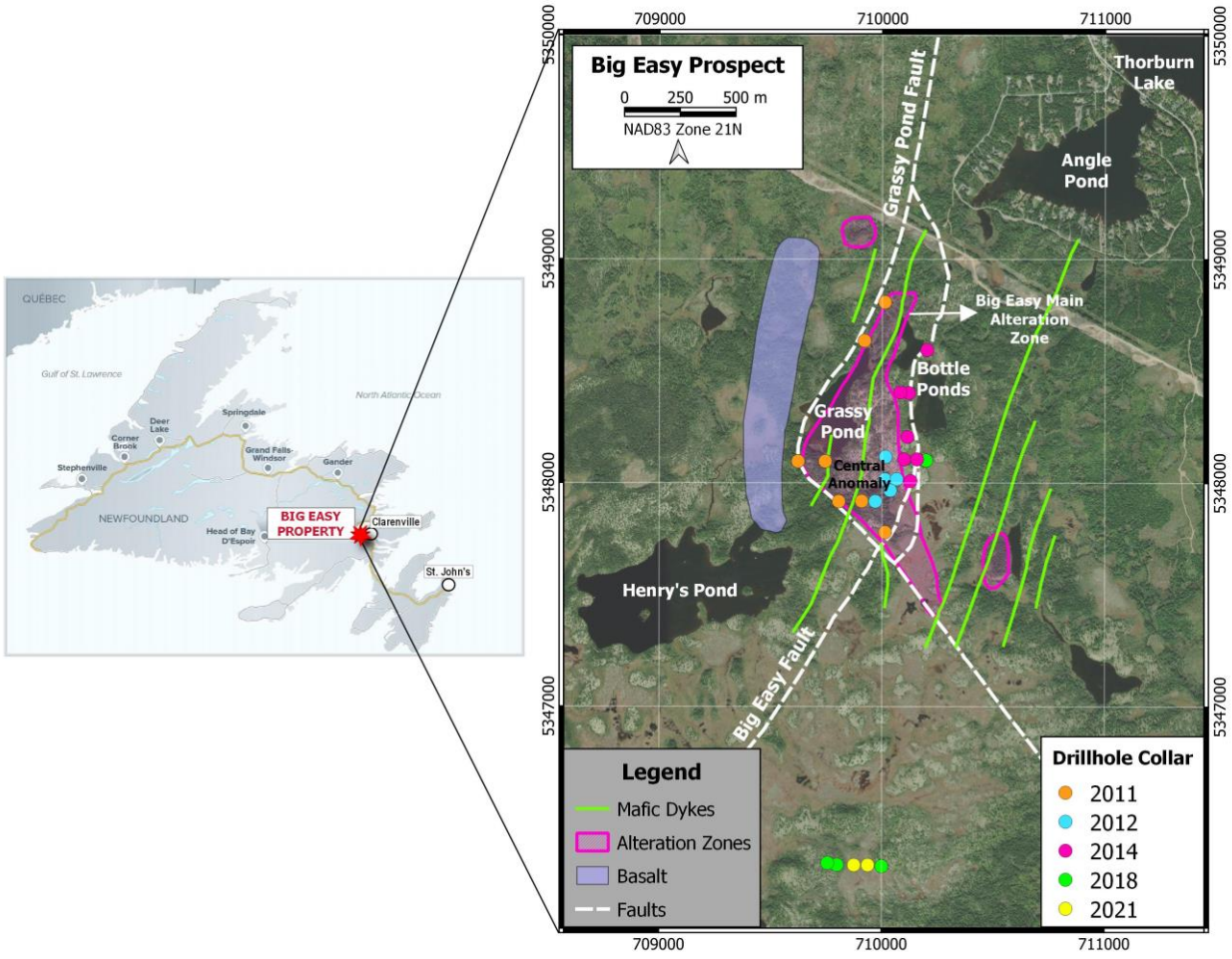

Figure 1.1 Big Easy property location and drill collar map. Drilling programs have been carried out in the vicinity of Grassy Pond, and to the immediate south, by Silver Spruce Resources Inc. (2011-2014) and Cartier Iron Corporation (2018-2021). The twenty-five drill collar locations are displayed in the right-hand frame. Structural and geological features, as inferred by Wall (2017) based on geophysical surveys, are also displayed on this map: Central alteration anomaly, a larger hidden basalt dyke (pale blue outline), other mafic dykes, Grassy Pond Fault (GPF), and Big Easy Fault (BEF). Big Easy Main Alteration Zone is also referred to as Big Easy Showing. New IP surveys recently completed by Cartier Iron in the Sleigh Pond Grid area in southern parts of the claims are outside the field of this figure.

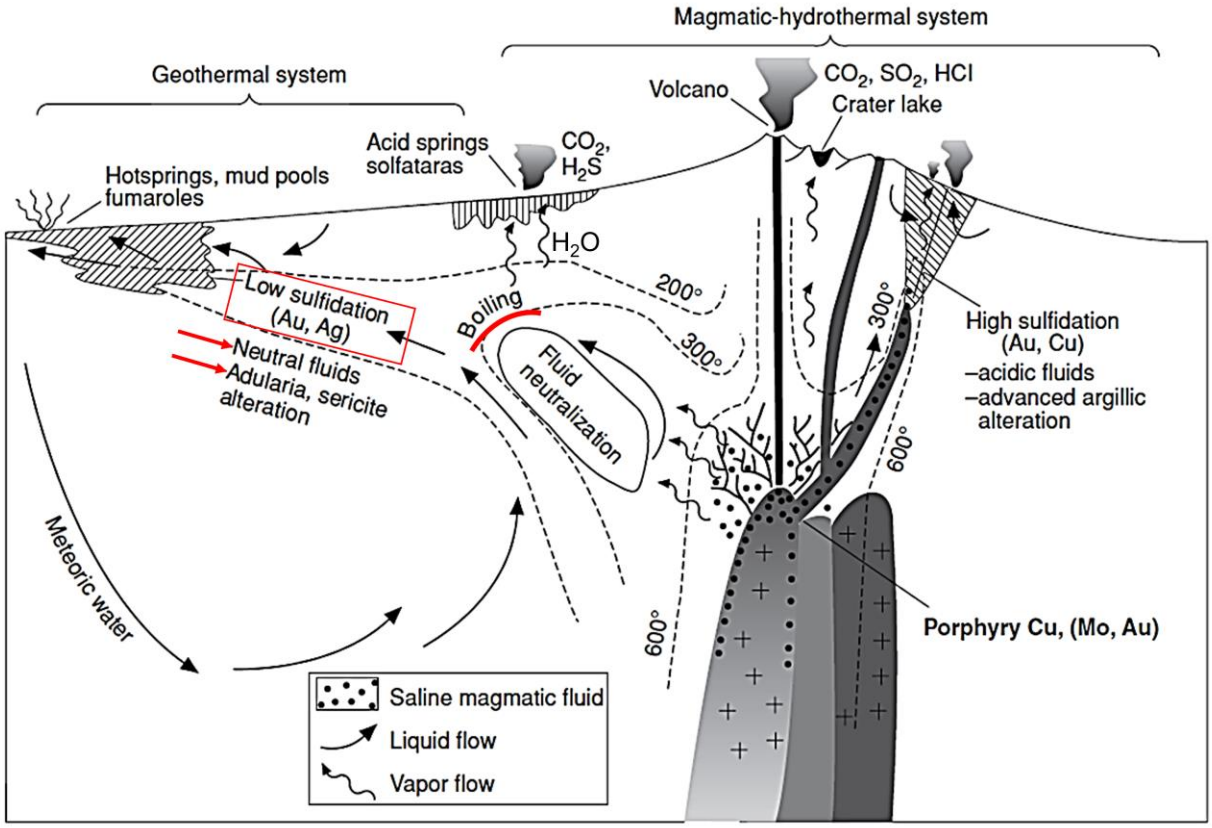

Figure 1.2 Epithermal deposits general model. Diagnostic characteristics of low sulfidation epithermal gold-silver deposits shown here include; adularia/sericite alteration, neutral pH hydrothermal fluids (often reflected by the presence of carbonate veining), hotspring deposits (including siliceous sinter), and boiling-related features (including crustiform and colloform vein textures). Figure modified from Hedenquist et al., 2000. Reproduced with permission (see Appendix 1).

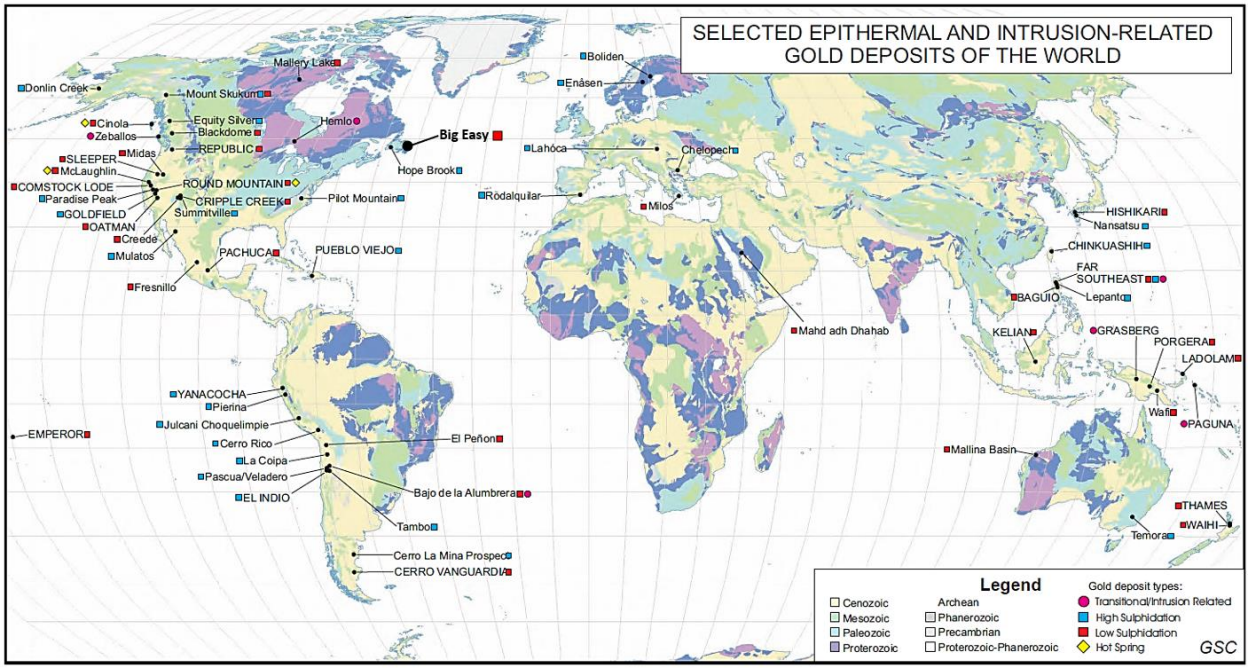

Figure 1.3 Distribution of epithermal and intrusion-related gold deposits worldwide, displaying the location of the Big Easy prospect as a black dot. Figure modified from Taylor, 2007. Reproduced with permission (see Appendix 1).

Feature	Low-Sulfidation*	High-Sulfidation
Sulfur redox state	**Reduced – S^{-2} H_2S**	Oxidized – S^{+4} SO_2
Fluids	**Geothermal systems, hot spring (meteoric source dominant)**	Active magmatic-hydrothermal systems (magmatic source)
Salinity	**Low (<2wt% NaCl)**	Moderate (2-20wt% NaCl)
pH	**Neutral (6-8) – Rock-dominated environment**	Acid (0-2) – Fluid-dominated environment (leaching)
Gold transport	**Bisulfide complex - $Au(HS)^-_2$**	Bisulfide complex - $Au(HS)^0$ Chloride complex - $Au(Cl)^-_2$
Alteration	**Silicification, potassic-sericitic (phyllic) ± chloritization ± carbonatization**	Advanced argillic
Ore style	**Open-space veins, stockwork, breccias – Bladed, banded, sinter**	Disseminated, replacement – Vuggy silica, pyrite-enargite veins
Ore minerals	**Pyrite, electrum, native gold, acanthite, native silver, tellurides/selenides ± Cpy ± Sph ± Gn**	Chalcopyrite, enargite/luzonite, tennantite-tetrahedrite, covellite, native gold ± pyrite
Gangue minerals	**Quartz, chalcedony, calcite, adularia-sericite, chlorite, smectite-illite ± zeolites**	Quartz, kaolinite-alunite, pyrophyllite, dickite, diaspore, native sulfur ± barite

Table 1.1 Comparison of the characteristic features of low-sulfidation and high-sulfidation epithermal gold systems. Compiled from (Hedenquist & Arribas, 2000; White & Hedenquist, 1990, 1995).

Feature	Big Easy	Haile	Fruta del Norte
Age	**573.3 ± 2.7 Ma ($^{206}Pb/^{238}U$ in zircon)**	548.7 ± 2.0 Ma (Re-Os in molybdenite)	169 ± 1.0 Ma (Re-Os in molybdenite)
Classification	**Gold-silver epithermal low-sulfidation**	Disseminated gold/sulfide mineralization. Replacement-type epithermal or exhalative system (?)	Gold-silver epithermal low- and intermediate-sulfidation
Host Terrane	**Avalon Zone**	Carolina Terrane	Amazon Craton (Zamora batholith)
Tectonic Environment	**Back arc/Extensional**	Transition from a volcanic arc-related subaerial constructional phase to a rift-dominated	Continental margin volcanic arc and subsequent pull-apart basin
Host Rocks	**Epiclastic sandstones and polymictic pebble conglomerates of the Musgravetown Group**	Silicified metasedimentary and metavolcanic rocks	Feldspar quartz porphyry (monzonite, tonalite and granodiorite); volcanic andesite
Cover Rocks	**Grey, green and red sandstones, conglomerates, siliceous sinter horizon**	Coastal plain sandstones, saprolitic weathering profile.	Conglomerates and other epiclastic rocks, siliceous sinter horizon
Vein Types	**1) Electrum dominant 2) High Au:Ag 3) Ginguro (High Ag:Au) 4) Molybdenite-rich**	Disseminated mineralization ± sulfide-quartz veins	1) Base metal-poor, quartz-adularia-calcite 2) Base metal-rich quartz, Mn-carbonate
Textures	**Colloform-crustiform, cockade, hydrothermal brecciation, milky to smoky quartz, drusy veins**	Hydrothermal brecciation. Remnant colloform, crustiform, and layered growth textures of pyrite	Vein-Stockworks. Colloform-crustiform, botryoidal, cockade and drusy veins. Finely laminated chalcedonic, and saccharoidal bands
Ore Minerals	**Electrum + pyrite + native silver + acanthite + molybdenite ± sphalerite ± naummanite ± aguilarite ± chalcopyrite ± uytenbogaardtite ± freibergite-tetrahedrite**	Native gold + electrum + pyrite + pyrrhotite + molybdenite ± Au-bearing tellurides ± arsenopyrite ± chalcopyrite ± galena ± sphalerite	Native gold + marcasite ± pyrite ± sphalerite ± galena ± chalcopyrite
Gangue Minerals	**Quartz + adularia ± chlorite ± illite ± sericite ± carbonate**	Sericite + quartz + chlorite + carbonate ± potassium feldspar	Quartz + adularia + calcite + Mn-carbonate
Alteration Zones	**Pervasive silicification, pyritization, chloritization**	Silicification, pyrite + kaolinite/sericite	Chalcedonic silicification, propylitic, marcasite/pyrite + illite

Table 1.2 Comparison of Big Easy to the Haile and Fruta del Norte deposits. Compiled from: Haile: Berry et al., 2016; Foley 2001; Mobley et al., 2014. Fruta del Norte: Leary et al, 2016 Stewart et al., 2017.

Chapter 2: Geological setting, stratigraphy, and tectonic environment of the Big Easy low-sulfidation epithermal system: Implications for the paleoenvironment of gold-silver mineralization

Abstract

The Burin and Bonavista peninsulas make up the western portion of the Avalon Zone in Newfoundland. Late Neoproterozoic volcanic, plutonic, and sedimentary rocks host a wide variety of low- and high-sulfidation epithermal gold occurrences in this region. Most of these are hosted in pyroclastic rocks related to episodes of high-volume volcanic activity in an ancient active margin of the Appalachian Orogen. The pyroclastic and other extrusive rocks range in composition from felsic to intermediate and occur in calderas, dome complexes, and other volcanic structures. The Big Easy prospect is a low-sulfidation epithermal gold occurrence, with mineralization predominantly hosted in epiclastic conglomeratic rocks of the Musgravetown Group, rather than the pyroclastic volcanic rocks of the Marystown Group, which are more typical of the known epithermal occurrences in the Avalon Zone. The host rocks at Big Easy record a distinctive local tectonic setting (at ca. 575 Ma) within the broader volcanic arc paleoenvironment of the late Neoproterozoic Avalon Zone. This study proposes a model that encompasses the tectonic context of the epiclastic rocks that occur in significant volumes throughout the Burin-Bonavista region – these being more prevalent in the northern portion of the peninsula, whereas pyroclastic rocks predominate in the southern part – and its relationship to the genesis of the Big Easy mineralization. Previously, a variety of tectonic settings have been proposed for the epithermal

gold occurrences within this region. Lithogeochemical analyses of host rocks have been used by some authors to suggest an island arc genesis. However, most aspects of the regional geology indicate a continental arc-style environment for the epithermal gold occurrences, with predominantly andesitic volcanic edifices subsequently affected by an extensional tectonic regime within a back-arc basin. Therefore, the epiclastic-hosted Big Easy mineralization is most likely associated with intra-caldera accumulations of sediments from an eroding volcano. These were modified at the surface by hot spring ponding, as well as fluvial reworking and redeposition of penecontemporaneous volcaniclastic rocks. Subsequently, a combination of rapid subsidence and high volume sedimentation in the latest Neoproterozoic (ca. 570 – 540 Ma), after the extensive volcano-plutonism activity around 575 Ma, led to the preservation of this shallow epithermal environment in the modern record.

2.1 INTRODUCTION.

The Big Easy prospect is located in the Avalon Zone, one of the four tectonostratigraphic divisions on the island of Newfoundland. From the west to the east these are: Humber Zone, Dunnage Zone, Gander Zone, and Avalon Zone. The Avalon Zone is perceived as the Avalon lower crustal block and encompasses all geological units to the east of the Dover Fault (Blackwood & Kennedy, 1975), and to the southeast of the Hermitage Bay Fault (Blackwood, 1976; Blackwood & O'Driscoll, 1976; Fig. 2.2 (inset)). The Avalon Zone contains submarine and nonmarine volcanic rocks and turbiditic, deltaic, fluviatile sedimentary rocks of Late Proterozoic age (760 Ma – 570 Ma; Colman-Sadd et al., 1990). These are overlain unconformably by a Late Proterozoic-Early

Paleozoic shallow marine succession, containing a distinctive Acado-Baltic trilobite faunal realm (Fletcher, 2006).

The geographic region broadly described by the Burin and Bonavista peninsulas comprise the western margin of the Avalon Zone (Fig. 2.2). The widespread occurrence of hydrothermally altered rocks and epithermal gold mineralization is one of the significant geological features of this region (O'Brien et al., 1998). These gold occurrences are related to extensive arc volcanism during the evolution of the Appalachian orogenic belt in the Late Neoproterozoic. In the Burin-Bonavista region, the Big Easy, Heritage, and Hickey's Pond prospects are currently being actively explored (Fig. 2.2).

2.2 GEOLOGICAL SETTING.

The Appalachian Orogen formed due to the breakup of supercontinent Rodinia and the subsequent coalescence of continental masses to form supercontinent Pangea (Hatcher, 2010; O'Brien et al., 1983). The preserved Appalachian mountain chain encompasses a series of Paleozoic accretion episodes that culminated with the collision between Gondwana (proto-Africa and South America) and Laurentia (proto-North America) at ca. 300 Ma (Hatcher, 2010). The Laurentian margin of the Appalachian Mountains extended from Newfoundland to the Coastal Plain of South Alabama and Georgia in the USA and was formed at ca. 550 Ma (Cawood et al., 2001; Cawood & Nemchin, 2001; Hatcher, 2010; Williams & Hatcher, 1983; Fig. 2.4).

The Avalon Zone – and the greater Avalonian terrane (Avalonia) – comprise the most northeastern part of the Appalachian Orogen (Williams, 1979: Fig 2.4). This zone is composed of two sequences: 1) Volcanic rocks with minor sedimentary rocks overlain by, 2) Nonmarine and marine sequences, containing some Late Proterozoic volcanic rocks, which extend to the Avalon and Burin peninsulas (Fig. 2.2; Hatcher, 2010). The geological setting of the Burin Peninsula includes a sequence of greenschist pillow basalts, mafic breccias, tuff, and related sedimentary rocks formed at ca. 760 Ma (O'Brien et al., 1996; Strong et al., 1978). Subsequent units comprise a volcano-sedimentary sequence of Neoproterozoic rocks (685 – 552 Ma), followed by a Paleozoic cover sequence unconformably overlain by late Silurian to early Devonian siliciclastic and volcanic rocks (O'Brien et al., 1996). In the Burin-Bonavista region (western Avalon Zone) the Neoproterozoic volcano-sedimentary sequences are divided into two large northeast-southwest trending belts, separated by sedimentary rocks of the Musgravetown Group (Fig. 2.2; Magyarosi et al., 2018).

The Late Neoproterozoic geological evolution of the Avalon Peninsula (eastern Avalon Zone; Fig. 2.2), was similar. It started with a lithologically complex sequence of volcanic rocks, intruded by a plutonic suite (ca. 620 Ma) that is coeval with a fault-bounded horst, with further arc-related volcano-plutonism ca. 580 – 570 Ma. A subsequent sedimentary succession included marine turbidites, deltaic shales, and siliciclastic sedimentary rocks (O'Brien et al., 2001). In the eastern Avalon Zone, lithologies range from Neoproterozoic submarine and nonmarine volcanic rocks, turbiditic, deltaic, and fluvial sedimentary rocks, to lower Paleozoic shallow marine successions overlying the Proterozoic rocks (O'Brien et al., 1998; Sparkes & Dunning, 2014).

2.3 LOCAL HOST STRATIGRAPHY AND TECTONIC EVOLUTION (BURIN – BONAVISTA REGION).

2.3.1 Stratigraphy.

The units that host epithermal Au-Ag deposits on the Burin Peninsula (and extending towards the base of the Bonavista Peninsula to the immediate north of Big Easy) are Late Neoproterozoic rocks of the Ediacaran period, with ages ranging from approximately 590 to 565 Ma (Mills et al., 2021; Fig. 2.5). These include the Marystown (ca. 575 Ma), Musgravetown (ca. 575 Ma), and Long Harbour (ca. 565 - 566 Ma) lithostratigraphic groups (Fig. 2.2; O'Brien et al., 1999).

On the Burin Peninsula, the Marystown Group is the most extensively exposed unit, and is predominantly made up of pyroclastic flows and volcanic rocks. These range in composition from basalt to rhyolite, dominated by more intermediate compositions of andesite (or andesitic basalt) to dacite with variable calc-alkaline and tholeiitic affinities (Ferguson, 2017; O'Brien et al., 1996, 1999). Pyroclastic and epiclastic sequences dominate the western margin of this group, although some massive flows are present, typically of basaltic composition (Ferguson, 2017).

The Musgravetown Group is dominated by fluviatile and lacustrine epiclastic and siliciclastic sedimentary rocks, with lesser subaerial and volcanic rocks (Mills & Sandeman, 2021; O'Brien et al., 1996). The Musgravetown group was first described by Jenness (1962) who recognized the following subdivisions (oldest to youngest): 1) The Cannings Cove Formation, which is predominantly conglomeratic with some basaltic intercalations and is overlain by, 2) The Bull Arm

Formation, which is predominantly volcanic; 3) Immature, cross-stratified sandstone of the Rocky Harbour Formation; and 4) The Crown Hill Formation, which is primarily red-pebble conglomerate and sandstone (Fig. 2.5; Mills et al., 2021).

As will be discussed below, the Musgravetown and Marystown groups are considered here to be penecontemporaneous facies of the same long-lived terrane, formed in a similar maturing volcanic arc environment. Geochemical analyses of a flow banded rhyolite that hosts the West Princess prospect in the Marystown Group, and a crystal lithic lapilli tuff from the Musgravetown Group, display overlapped and similar extended REE patterns, but separate U-Pb zircon ages of 573.3 ± 2.7 Ma (Ferguson, 2017), and 591.3 ± 1.6 Ma (Mills et al., 2017), respectively.This similarity in geochemical patterns despite being separated in time, represents a common feature of felsic volcanic rocks in the Avalon Zone (Mills et al., 2017). Other published U-Pb zircon ages for the Musgravetown Group include 620 ± 2 Ma for the calc-alkaline Broad Island Group (former Love Cove Group); 605 ± 1.2 Ma for rhyolite from near Bull Arm (type area, Bull Arm Formation, lower Musgravetown Group); 589 ± 2.0 Ma for a schist from the Love Cove type locality; 568.7 ± 1.4 Ma for rhyolite of the Rocky Harbour Formation, upper Musgravetown Group; and 572 ± 2 Ma for Louil Hills granite (Mills et al., 2021; Fig. 2.5).

Further west, the Long Harbour Group is younger and compositionally different from Marystown and Musgravetown groups, comprising subaerial felsic volcanic rocks of alkaline to peralkaline affinity, and dominated by rhyolites with lesser mafic volcanics (Ferguson, 2017; O'Brien et al., 1996). A recent U-Pb zircon determination of an epithermally-mineralized flow-banded rhyolite near Long Harbour yielded an age of 566.5 ± 1.9 Ma (Ferguson, 2017). The Long Harbour group

is interpreted as the youngest Neoproterozoic volcanic unit recognized in the Avalon Zone, corresponding to a volcano-plutonic episode between 568 ± 5 and 552 ± 3 Ma (Mills et al., 2021; O'Brien et al., 1996). Additionally, the Grandy's Pond Arenite Belt (GPAB: "Arenite Belt" in Figure 2.2) is predominantly composed of terrestrial and shallow marine epiclastic sedimentary rocks with lesser associated pyroclastic rocks (Dec et al., 1992). The GPAB is mainly derived from the erosion of volcanic rocks from the Marystown Group, and also contains ash detritus from the younger Long Harbour Group, as inferred from geochemical signatures and U-Pb zircon dating of these three units (Ferguson, 2017). A sample of an epiclastic sedimentary rock from the GPAB yielded a detrital zircon age of 566.2 ± 4.4 Ma (Ferguson, 2017), comparable to that determined for the Long Harbour Group.

At the Heritage and Hickey's Pond prospects, mineralization is hosted within predominantly volcanic rocks of the Marystown Group. At Big Easy, the mineralization is mainly hosted by the Musgravetown Group, within interbedded epiclastic sandstones and polymictic pebble conglomerates (Fig. 2.3), which overly predominantly volcanic rocks.

2.3.2 Tectonic evolution.

The early development of a primitive Avalonian arc coincided with the amalgamation of the supercontinent Rodinia at 1.2 – 1.0 Ga (Nance et al., 2002). The onset of this early magmatism and its evolution from an oceanic juvenile arc toward a mature arc setting at 750 Ma was geodynamically related to the breakup of Rodinia (Murphy et al., 2019). The Burin Group mainly records orogenic events related to these Neoproterozoic processes - as a sequence of greenschist

pillow basalts, mafic breccias, tuff, and other associated volcano-sedimentary rocks observed in the southwestern Avalon Zone (O'Brien et al., 1996; Strong et al., 1978).

Subsequent tectonic activity fostered arc-related volcanic rocks between 685 and 670 Ma, locally including basalts, andesites, and minor siliciclastic, mafic volcaniclastic, and sedimentary carbonate rocks (Early Arc/Back Arc in Figure 2.6; O'Brien et al., 1996). This volcanic arc ceased with its accretion to Gondwana at 670 Ma and consequent margin arc-related magmatism and basin formation coeval with the amalgamation and development of Gondwana took place from 635 to 570 Ma (Continental Magmatic Arc to Volcanic Arc Basins in Figure 2.6; Murphy et al., 2019; Nance et al., 2002).

After this mature arc was thoroughly developed, a transition into a continental margin transform boundary due to ridge-trench collision is recognized, along with the propagation of a San Andreas style transform fault (Arc to Rift Transition in Figure 2.6; Murphy et al., 2019). Finally, circa 540 Ma, continental rifting in the earliest Paleozoic led to the separation of Avalonia from Gondwana and later accretion to the Laurentia continental craton (Nance et al., 2002). Early Paleozoic platformal successions have been used to define the eastern flank of the Iapetus – proto-Atlantic Ocean boundary (Platform Sequences in Figure 2.6; Murphy et al., 2019).

Volcanic and plutonic rocks with Neoproterozoic crystallization ages between 635 and 570 Ma correspond to peak magmatism within the Avalon Zone (Mills & Sandeman, 2021; Nance et al., 1991). Ferguson (2017; and references therein) document two peak volcano-plutonic events evident in the Burin Peninsula region – one at circa 620 Ma and one at ca 575 Ma. This observation

is permissive of at least two arc building episodes during the 635 – 570 Ma period of evolution of this terrane.

Volcanic rocks of the Ediacaran Musgravetown Group include a basal ca. 600 Ma calc-alkaline basalt ("HB-calc-alkaline" at the base of the Bull Arm Formation; Fig. 2.5 and 2.6), which is overlain by a continental tholeiite and alkaline rhyolite of the ca. 592 Ma Plate Cove volcanic belt, at the top of the Bull Arm Formation (Mills et al., 2021). This relationship implies a change from subduction-related to extension-related tectonic regimes, which occurred shortly after the eruption of the calc-alkaline basalt section of the Cannings Cove Formation at ca. 600 Ma (Mills & Sandeman, 2021). This subsequent extension-related volcanic activity is consistent with a geodynamic setting that evolved from a mature arc into extensional basins with the subsequent waning of magmatism (Mills & Sandeman, 2021).

Subsequent to the latest volcanic activity recorded in the Bull Arm Formation, evidence of the Gaskiers glaciation event (ca. 580 Ma) was deposited in a forearc basin from a complex arc with continental crust (Retallack, 2013; Fig. 2.5). Based on the presence of oxidized palaeosols and a re-evaluation of sedimentary facies during this period, Retallack (2013) inferred a humid temperate climate and marked marine regression evinced by the Gaskiers event during the early Ediacaran (Retallack, 2013). A transition to bimodal within-plate magmatism and continental clastic sedimentation along significant faults, indicates the cessation of a second episode of arc-related magmatism around 570 – 565 Ma. (arc to rift transition in Figure 2.6; Murphy et al., 1999; Nance et al., 2002; O'Brien et al., 1996). Coeval sedimentary successions dominated by volcaniclastic turbidites with interlayered mafic volcanic rocks (Rocky Harbour Formation; Fig. 2.5) are directly

associated with this late-magmatic and volcanic activity. These volcaniclastic sediments have been interpreted as subsequently deposited into intra-arc and back-arc basins (Nance et al., 2002; Pe-Piper & Murphy, 1989). Passive-margin development resulted in the most significant inundation of the interior of Laurentia during the Late Cambrian and Early Ordovician and the formation of the Appalachians Mountains (Hatcher, 2010).

2.4 DISCUSSION.

The Big Easy prospect is hosted by sandstones and polymictic conglomerates that are clearly epiclastic in nature. These units comprise part of the mapped Musgravetown Group and are interpreted here as equivalent to the Rocky Harbour Formation (<580 Ma; Mills et al, 2021; Fig. 2.5). The host rocks are heavily silicified within an envelope that surrounds the known vein stockwork of the Big Easy occurrence, and this envelope is crosscut by later (566 ± 2 Ma) intermediate dykes (Clarke, 2013), representing a minimum age limit for the mineralizing hydrothermal activity. The U-Pb zircon age of 573.3 ± 2.7 Ma of Ferguson (2017) for the West Princess Rhyolite, a flow-banded dome rhyolite that outcrops 3 km immediately to the north of the Big Easy prospect provides a tentative estimate for the age of the host stratigraphy at Big Easy that would be compatible with inclusion in the Rocky Harbour Formation.

Other epithermal systems currently recognized on the Burin Peninsula (e.g., Heritage, Hickey's Pond) are hosted mainly in felsic to intermediate volcanic rocks of the 580 – 570 Ma Marystown Group. This makes the Big Easy epiclastic-hosted mineralization comparatively unusual – at least in terms of currently recognized epithermal occurrences in this region.

Epiclastic conglomerates, and subsidiary breccias, within this portion of the Musgravetown Group (Rocky Harbour Formation), consist of rocks that reflect the reworking of particles and fragments of volcanic material previously deposited (Mills et al., 2017). The origin of the clasts is consistent with the weathering of one or more volcanic centres, and their subsequent transport and sedimentation. Based on the characteristics of the stratigraphy at Big Easy, these host rocks are interpreted to have formed by intracaldera deposition, in part within sulfidic geothermal ponds, with a later crosscutting event(s) of epithermal veins after the sediments were fully indurated (Ferguson, 2017).

The host lithologies the Big Easy prospect, including the presence of abundant epiclastic sediments, can be considered typical of a caldera-type environment during a later stage of volcanic activity. A generalized model of arc tectonic evolution for an analogous intra-caldera paleoenvironment, which potentially explains the genesis of epiclastic sediments and their relationship with epithermal gold deposits, was proposed by Feiss et al., 1993, with specific reference to gold-bearing deposits recognized within the Neoproterozoic Carolina Slate Belt (Fig. 2.7). Primary arc volcanism is followed by extension and coeval rift expansion as volcanism wanes. This environment is recorded by the accumulation of intracaldera epiclastic sediments and hot spring deposits, such as sinter, associated with the development of meteoric water-dominant hydrothermal systems. In the late stage of the volcanic arc system, continued extension and subsidence result in the burial and preservation of pyroclastic successions and epithermal ore deposits under epiclastic rift-fill sediments derived from active and remnant arcs (Feiss et al., 1993).

Evidence for sinter, characteristic of a paleosurface within a subaerial geothermal environment, is observed at Big Easy and demonstrates exceptional preservation of the hydrothermal system as a whole (Dimmell, 2013; Ferguson, 2017). This is an unusual feature for an epithermal deposit of Neoproterozoic age. Most recognized epithermal deposits were formed during the Cenozoic and it is traditionally perceived that older deposits are almost inevitably removed by erosion (Goldfarb et al., 2010). An additional characteristic of these paleosurface features at Big Easy is the presence of epiclastic host rocks deposited in intracaldera lacustrine environments, marginal to the volcanic center, and accumulating in surface hot spring ponds (Layne et al., 2019). Additional evidence for near-surface hydrothermal activity is present at Big Easy as coeval interbedded banded colloidal silica within the sedimentary host rock, which is found within the vein mineralization zone (Ferguson, 2017). This is interpreted as having formed in the "chalcedony blanket" zone where hot spring fluids encountered the submerged meteoric water table (Hedenquist et al., 2000). Sustained clastic sedimentation, with periodic phreatic eruptions (as evidenced by brecciated textures in the host rocks), as well as reworking of volcanic-rock fragments by running water (extensive rounding of conglomerate clasts) appears to have taken place. All of these features support the interpretation that the host sediments accumulated in an intracaldera (or caldera-proximal) setting consistent with incipient extensional tectonics.

2.5 CONCLUSIONS.

The most prospective period for epithermal deposits within the Neoproterozoic Avalon Zone is from ca. 620 Ma until the nominal end of the Neoproterozoic at 541 Ma, including prospects like

Hickey's Pond at ca. 585 Ma, and Big Easy at ca. 573 Ma. This period encompassed extended episodes of arc magmatism at ca. 620 Ma (e.g., Broad Island Group) and ca. 585 – 570 Ma, and a third episode at ca. 565 Ma (Long Harbour Group). Big Easy appears to have been associated with the 585 – 570 Ma episode, as were most of the other recognized epithermal occurrences in the Avalon Zone (Ferguson, 2017).

The atypical epiclastic host rocks, and other features of the Big Easy prospect, suggest a specific paleoenvironment existed in this location during the Late Neoproterozoic. The development of an extensional basin within a continental volcanic arc margin can explain the tectono-magmatic context of the genesis of the Big Easy low-sulfidation epithermal gold occurence. This tectonic context is comparable to the transition from a volcanic arc-related subaerial constructional phase to a rift-dominated environment that occurred at Haile Gold Mine (Feiss et al., 1993). Likewise, similar tectonic processes formed Fruta Del Norte Gold Deposit during the transition from an active continental margin volcanic arc to a pull-apart basin (Leary et al., 2020; Stewart et al., 2017).

In all three examples, tectonic processes generated a sequence of epiclastic rocks, that are spatially related to the mineralized system. At Haile, the mineralization mainly occurs as disseminated gold-iron sulfide near the transition between a thick sequence of metavolcanic rocks and crystal tuffs and siltstones and an overlying sequence of other volcaniclastic and epiclastic rocks. The crystal tuff-siltstone sequence, in particular, has subsequently been heavily metamorphosed and polydeformed. In contrast, at Fruta Del Norte the mineralization is mostly concentrated in auriferous base metal-poor veins hosted by andesitic volcanic rocks, which are covered by silicified epiclastic and volcaniclastic sequences. The presence of epiclastic sandstones and

polymictic conglomerates as the predominant host rocks at Big Easy, with mineralization concentrated in quartz-adularia veins, represents a differential feature compared to these two homologous epithermal systems. Overall, the three deposits have distinct timing relationships with respect to the emplacement, silicification and induration of the associated epiclastic sediment sequences and the emplacement of epithermal mineralization. Further study of this charactersitic of Big Easy, and similar deposits, is recommended, including rigorous comparisons with the limited known occurrences of epiclastic-hosted and epiclastic-associated epithermal deposits within greater Avalonia.

Detailed whole-rock lithogeochemistry and Sm-Nd isotope analysis – to compare regional volcanics with the epiclastic sediment lithologies – would help to clarify the arc-related source(s) of the sediments, as well as the timing of deposition and its relationship with the local tectonic setting. The Avalon Zone is a complex terrane, but renewed mapping, and paleoenvironmental reconstruction, using models incorporating the most recent data will help to further clarify the tectonic evolution of this terrane, and the Burin-Bonavista region in particular. There is a strong implication that the peak period for epithermal precious metal deposition in the Late Neoproterozoic, especially in the Burin Peninsula region, coincided with the incipient re-extension of the host volcanic arc, yielding regionally extensive epiclastic sediments (e.g., Grandy's Pond Arenite Belt) on the flanks of the evolving basin, as well as more localized intracaldera accumulations. Both of these environments could potentially host epithermal mineralization. Subsequent rapid subsidence to below sea level and consequent rapid accumulation of marine sediments within the submerged extensional basin would further explain the exceptional preservation of the mineralization at Big Easy.

Globally, and through time, the tectonic setting for epithermal deposits is diverse, with a combination of physical processes occurring within a variety of very dynamic paleoenvironments. The Big Easy prospect's local tectonic and lithological characteristics should serve to expand potential exploration targets for other epithermal gold deposits, especially those hosted in non-volcanic rocks, throughout the Avalon Zone.

2.6 REFERENCES.

Barton, P. B., Rye, R. O., & Bethke, P. M. (2000). Evolution of the Creede caldera and its relation to mineralization in the Creede mining district, Colorado. Special Paper of the Geological Society of America, 346, 301–326. https://doi.org/10.1130/0-8137-2346-9.301

Berry, J. M., Mobley, R. M., Gillon, K. A., Yogodzinski, G. M., & Bates, C. C. (2016). A neoproterozoic epithermal gold deposit - The Haile gold mine, South Carolina, USA. GSA Field Guides, 42(01), 1–8. https://doi.org/10.1130/2016.0042(01)

Blackwood, R. F. (1976). The relationship between the Gander and Avalon zones in the Bonavista Bay region, Newfoundland. MSc Thesis, Memorial University of Newfoundland, 156p.

Blackwood, R. F., & Kennedy, M. J. (1975). The Dover Fault: Western Boundary of the Avalon Zone in Northeastern Newfoundland. Canadian Journal of Earth Sciences, 12(2), 320–325. https://doi.org/10.1139/e75-027

Blackwood, R. F., & O'Driscoll, C. F. (1976). The Gander–Avalon Zone boundary in southeastern Newfoundland. Canadian Journal of Earth Sciences, 13(8), 1155–1159. https://doi.org/10.1139/e76-118

Cawood, P. A., McCausland, P. J. A., & Dunning, G. R. (2001). Opening Iapetus: Constraints from the Laurentian margin in Newfoundland. Bulletin of the Geological Society of America, 113(4), 443–453. https://doi.org/10.1130/0016-7606(2001)113<0443:OICFTL>2.0.CO;2

Cawood, P. A., & Nemchin, A. A. (2001). Paleogeographic development of the East Laurentian margin: Constraints from U-Pb dating of detrital zircons in the Newfoundland Appalachians. Bulletin of the Geological Society of America, 113(9), 1234–1246. https://doi.org/10.1130/0016-7606(2001)113<1234:PDOTEL>2.0.CO;2

Clarke, M. (2013). Host lithologies, breccia development, alteration and gold mineralization at the Big Easy prospect, B.Sc. (Honours) Thesis, Memorial University of Newfoundland, 85p.

Colman-Sadd, S. P., Hayes, J. P., & Knight, I. (1990). Geology of the Island of Newfoundland. In Geological Survey Branch, Newfoundland Department of Mines and Energy, Government of Newfoundland and Labrador. Map, 1p.

de Ronde, C. E. J., Walker, S. L., LeBlanc, C., Davy, B. W., Fornari, D. J., Tontini, F. C., Scott, B. J., Seebeck, H., Stewart, T. J., Mazot, A., Nicol, A., & Tivey, M. A. (2016). Reconstruction of the geology and structure of Lake Rotomahana and its hydrothermal systems from high-resolution multibeam mapping and seismic surveys: Effects of the 1886 Tarawera Rift eruption. Journal of Volcanology and Geothermal Research, 314, 57–83. https://doi.org/10.1016/j.jvolgeores.2016.02.002

Dec, T., O'Brien, S. J., & Knight, I. (1992). Late Precambrian volcaniclastic deposits of the Avalonian Eastport basin (Newfoundland Appalachians): petrofacies, detrital clinopyroxene geochemistry and palaeotectonic implications. Precambrian Research, 59(3–4), 243–262. https://doi.org/10.1016/0301-9268(92)90059-W

Dimmell, P. (2013). Report on 2013 Exploration (Field Geological Evaluation, Geophysical/Geological, Compilation) on the Big Easy (BE) Property. Licences 13446M, 16633M, 17315M, 20943M, 20944M, NTS 2D/1, 8, Thorburn Lake Area, Eastern Newfoundland for Silver Spruce Resources Inc., 139p.

Feiss, P. G., Vance, R. K., & Wesolowski, D. J. (1993). Volcanic rock-hosted gold and base-metal mineralization associated with Neoproterozoic-early Paleozoic back-arc extension in the Carolina terrane, southern Appalachian Piedmont. Geology, 21(5), 439–442. https://doi.org/10.1130/0091-7613(1993)021<0439:VRHGAB>2.3.CO;2

Ferguson, S. A. (2017). Late Neoproterozoic epithermal-style Au mineralization of the Burin Peninsula, Newfoundland: U-Pb geochronology and deposit characteristics, M.Sc. Thesis, Memorial University of Newfoundland, 394p.

Fletcher, T. P. (2006). Bedrock geology of the Cape St. Mary's Peninsula, southwest Avalon Peninsula, Newfoundland. (Includes parts of NTS map sheet 1M/1, 1N/4, 1L/16 and 1K/13). Report 06-02, 137p.

Goldfarb, R. J., Bradley, D., & Leach, D. L. (2010). Secular variation in economic geology. Economic Geology, 105(3), 459–465. https://doi.org/10.2113/gsecongeo.105.3.459

Goldfarb, R. J., & Groves, D. I. (2015). Orogenic gold: Common or evolving fluid and metal sources through time. Lithos, 233, 2–26. https://doi.org/10.1016/j.lithos.2015.07.011

Hatcher, R. D. (2010). The Appalachian orogen: A brief summary. Memoir of the Geological Society of America, 206(01), 1–19. https://doi.org/10.1130/2010.1206(01)

Hedenquist, J., Arribas, A., & Gonzalez-Urien, E. (2000). Exploration for Epithermal Gold Deposits. Reviews in Economic Geology, 13(l), 245–277.

Izawa, E., Urashima, Y., Ibaraki, K., Suzuki, R., Yokoyama, T., Kawasaki, K., Koga, A., & Taguchi, S. (1990). The Hishikari gold deposit: high-grade epithermal veins in Quaternary volcanics of southern Kyushu, Japan. Journal of Geochemical Exploration, 36(1–3), 1–56. https://doi.org/10.1016/0375-6742(90)90050-K

Jenness, S. E. (1962). Paper 63-1 Summary of Research: Field, 1962. Geological Survey of Canada: Department of Mines and Technical Surveys, 81p.

Layne, G. D., Barr, S. M., & White, C. E. (2019). Metallogeny of the Avalonian Mira Terrane, Southeastern Cape Breton Island, Nova Scotia: A Preliminary Study. Report of activities 2018-2019, 12p.

Leary, S., Sillitoe, R. H., Lema, J., Téliz, F., & Mena, D. (2020). Geology of the Fruta del Norte Epithermal Gold-Silver Deposit, Ecuador. Society of Economic Geologists - SEG Special Publications, 23, 431–450. https://doi.org/10.5382/sp.23.21

Leary, S., Sillitoe, R. H., Stewart, P. W., Roa, K. J., & Nicolson, B. E. (2016). Discovery, geology, and origin of the Fruta del Norte epithermal gold-silver deposit, southeastern Ecuador. Economic Geology, 111(5), 1043–1072. https://doi.org/10.2113/econgeo.111.5.1043

Magyarosi, Z., Layne, G., & Sparkes, G. (2018). GAC NL 2018 Fall FieldTrip Mineral Deposits of the Burin Peninsula Open File NFLD/3338. Geological Association of Canada, Newfoundland and Labrador Section, 47p.

Mills, A. J., Dunning, G. R., & Langille, A. (2016). New Geochronological Constraints on the Connecting Point Group, Bonavista Peninsula, Avalon Zone, Newfoundland. Current Research: Newfoundland Geological Survey, Newfoundland Department of Mines and Energy, Report 16-, 153–171. https://doi.org/10.13140/RG.2.1.2015.7200

Mills, A. J., & Dunning, G. R. (2017). New geochronological constraints on the timing of magmatism for the Bull Arm Formation, Musgravetown Group, Avalon Terrane, Northeastern Newfoundland. Current Research: Newfoundland Geological Survey, Newfoundland Department of Mines and Energy, Report 17-, 1–17. https://doi.org/10.13140/RG.2.2.35619.04648

Mills, A. J., Dunning, G. R., Murphy, M., & Langille, A. (2017). New geochronological constraints on the timing of magmatism for the Bull Arm Formation, Musgravetown Group, Avalon Terrane, Northeastern Newfoundland. Current Research: Newfoundland Geological Survey, Newfoundland Department of Mines and Energy, Report 17-, 1–17. https://doi.org/10.13140/RG.2.2.35619.04648

Mills, A. J., Dunning, G. R., & Sandeman, H. A. (2021). Lithogeochemical, isotopic, and U-Pb (Zircon) age constraints on arc to rift magmatism, northwestern and central Avalon Terrane, Newfoundland, Canada: Implications for local lithostratigraphy. Canadian Journal of Earth Sciences, 58(4), 332–354. https://doi.org/10.1139/cjes-2019-0196

Mills, A. J., & Sandeman, H. (2021). Lithostratigraphy and lithogeochemistry of Ediacaran alkaline basaltic rocks of the Musgravetown Group, Bonavista Peninsula, northeastern Newfoundland, Canada: An extensional volcanogenic basin in the type-Avalon terrane. Atlantic Geology, 57(1), 207–234. https://doi.org/10.4138/atlgeol.2021.010

Murphy, J. B., Keppie, J. D., Dostal, J., & Nance, R. D. (1999). Neoproterozoic-early Paleozoic evolution of Avalonia. Special Paper of the Geological Society of America, 336, 253–266. https://doi.org/10.1130/0-8137-2336-1.253

Murphy, J. B., Nance, R. D., Keppie, J. D., & Dostal, J. (2019). Role of Avalonia in the development of tectonic paradigms. Geological Society Special Publication, 470(1), 265–287. https://doi.org/10.1144/SP470.12

Nance, R. D., Murphy, J. B., & Keppie, J. D. (2002). A Cordilleran model for the evolution of Avalonia. Tectonophysics, 352(1–2), 11–31. https://doi.org/10.1016/S0040-1951(02)00187-7

Nance, R. D., Murphy, J. B., Strachan, R. A., D'Lemos, R. S., & Taylor, G. K. (1991). Late Proterozoic tectonostratigraphic evolution of the Avalonian and Cadomian terranes. Precambrian Research, 53(1–2), 41–78. https://doi.org/10.1016/0301-9268(91)90005-U

O'Brien, S. J. (1993). A preliminary account of geological investigations in the Clode Sound – Goose Bay region, Bonavista Bay, Newfoundland (NTS 2C/5 NW and 2D/8 NE). Current Research: Newfoundland Geological Survey, Newfoundland Department of Mines and Energy, 93(1), 293–309.

O'Brien, S. J., Dube, B., & O'Driscoll, C. F. (1999). High-Sulphidation, Epithermal-Style Hydrothermal Systems in Late Neoproterozoic Avalonian Rocks on the Burin Peninsula, Newfoundland: Implications for Gold Exploration. Geological Survey, 99–1, 275–296.

O'Brien, S. J., Dubé, B., O'Driscoll, C. F., & Mills, J. (1998). Geological setting of gold mineralization and related hydrothermal alteration in Late Neoproterozoic (post-640Ma) Avalonian Rocks of Newfoundland, with a review of coeval gold deposits elsewhere in the Appalachian Avalonian Belt. Current Research: Newfoundland Geological Survey, Newfoundland Department of Mines and Energy, 93–124.

O'Brien, S. J., Dunning, G. R., Dubé, B., Driscoll, C. F. O., Sparkes, B., Israel, S., & Ketchum, J. (2001). New Insights Into the Neoproterozoic Geology of the Central Avalon Peninsula (Parts

of Nts Map Areas 1N/6, 1N/7 and 1N/3), Eastern Newfoundland. Current Research: Newfoundland Geological Survey, Newfoundland Department of Mines and Energy, 169–189.

O'Brien, S. J., O'Brien, B. H., Dunning, G. R., & Tucker, R. D. (1996). Late Neoproterozoic Avalonian and related peri-Gondwanan rocks of the Newfoundland Appalachians. Special Paper of the Geological Society of America, 304, 9–28. https://doi.org/10.1130/0-8137-2304-3.9

O'Brien, S. J., Wardle, R. J., & King, A. F. (1983). The Avalon Zone: A Pan-African terrane in the Appalachian Orogen of Canada. Geological Journal, 18(3), 195–222. https://doi.org/10.1002/gj.3350180302

Pe-Piper, G., & Murphy, J. B. (1989). Geochemistry and tectonic setting of the late Precambrian Folly River Formation, Cobequid Highlands, Avalon Terrane, Nova Scotia: a continental rift within a volcanic-arc environment. Atlantic Geology, 25(2), 143–151. https://doi.org/10.4138/1679

Pu, J. P., Bowring, S. A., Ramezani, J., Myrow, P., Raub, T. D., Landing, E., Mills, A., Hodgin, E., & Macdonald, F. A. (2016). Dodging snowballs: Geochronology of the Gaskiers glaciation and the first appearance of the Ediacaran biota. Geology, 44(11), 955–958. https://doi.org/10.1130/G38284.1

Retallack, G. J. (2013). Ediacaran gaskiers glaciation of Newfoundland reconsidered. Journal of the Geological Society, 170(1), 19–36. https://doi.org/10.1144/jgs2012-060

Simpson, M. P., Mauk, J. L., & Simmons, S. F. (2001). Hydrothermal alteration and hydrologic evolution of the golden cross epithermal Au-Ag deposit, New Zealand. Economic Geology, 96(4), 773–796. https://doi.org/10.2113/gsecongeo.96.4.773

Sparkes, G. W., & Dunning, G. R. (2014). Late Neoproterozoic Epithermal Alteration and Mineralization in the Western Avalon Zone: a summary of mineralogical investigations and new U/Pb geochronological results. Current Research, Newfoundland and Labrador Department of Natural Resources Geological Survey, Report 14-1, p. 99-128.

Sparkes, G. W., Ferguson, S. A., Layne, G. D., Dunning, G. R., Brien, S. J. O., & Langille, A. (2016). The nature and timing of Neoproterozoic high-sulphidation gold mineralization from the Newfoundland Avalon Zone: Insights from new U-Pb ages, ore petrography and spectral data from the Hickey's Pond prospect. Current Research, Newfoundland and Labrador Department of Natural Resources Geological Survey, Report 16-1, p. 91-116.

Stewart, P. W., Stein, H. J., & Roa, K. (2017). Fruta del Norte , Ecuador : a completely preserved Late Jurassic epithermal gold-silver deposit. Proceedings of the 14th Biennial SGA Meeting, 20-23 August 2017, Quebec City, Canada, p. 99–102.

Strong, D. F., O'Brien, S. J., Taylor, S. W., Strong, P. G., & Wilton, D. H. (1978). Aborted Proterozoic Rifting in Eastern Newfoundland. Canadian Journal of Earth Sciences J Earth Sci, 15(1), 117–131. https://doi.org/10.1139/e78-010

Williams, H. (1979). Appalachian Orogen in Canada. Canadian Journal of Earth Sciences, 16(3), 792–807. https://doi.org/10.1139/e79-070

Williams, H., & Hatcher, R. D. (1983). Appalachian suspect terranes. Contributions to the Tectonics and Geophysics of Mountain Chains, p. 33–53. doi:10.1130/mem158-p33

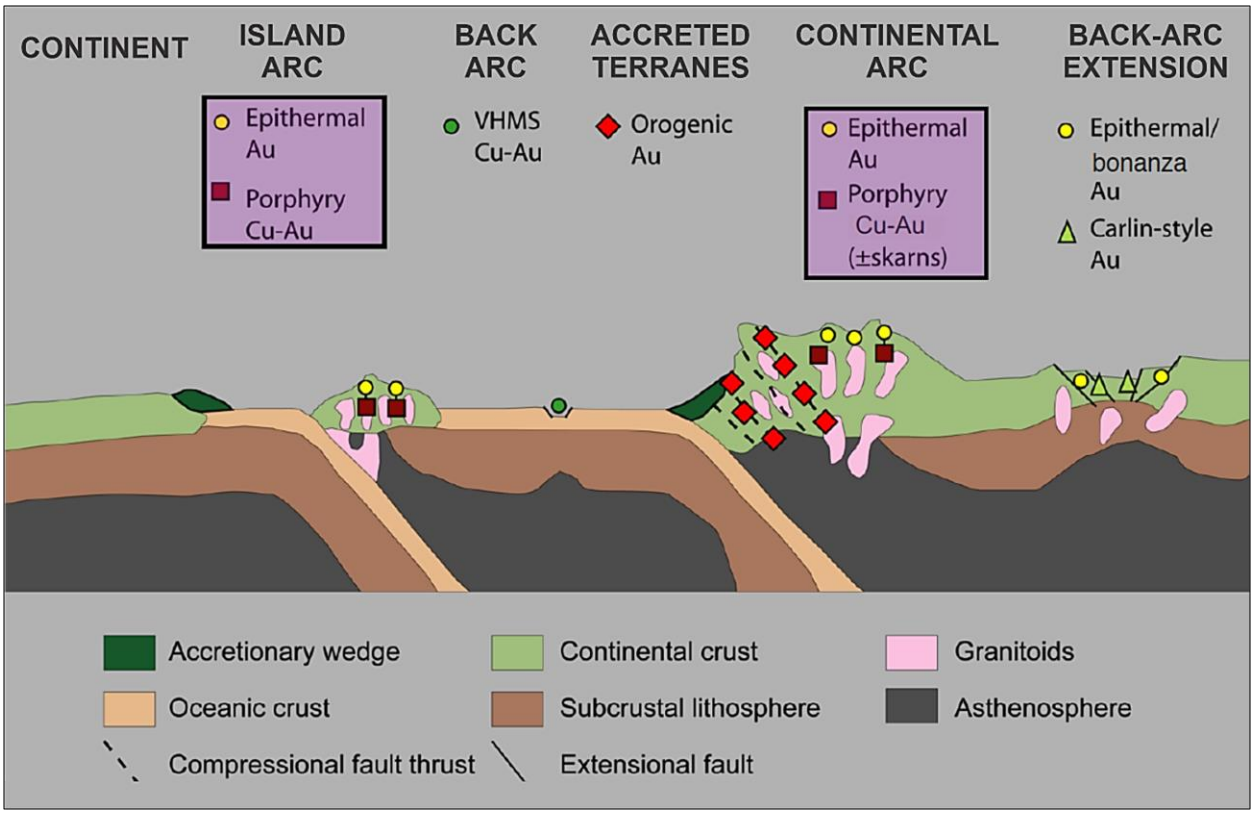

Figure 2.1 Tectonic setting of epithermal deposits and other gold deposit types. Figure modified from Goldfarb & Groves, 2015. Epithermal gold deposits form in shallow subaerial environments associated with volcanism in continental arcs, oceanic arcs, or back-arc basins. For Big Easy, the tectonic environment is interpreted as related to a continental-arc to back-arc transition. This incipience of back-arc extension is a natural evolution of continental arcs and represents an important environment where volcanic caldera-related epithermal deposits can be generated and preserved. Reproduced with permission (see Appendix 1).

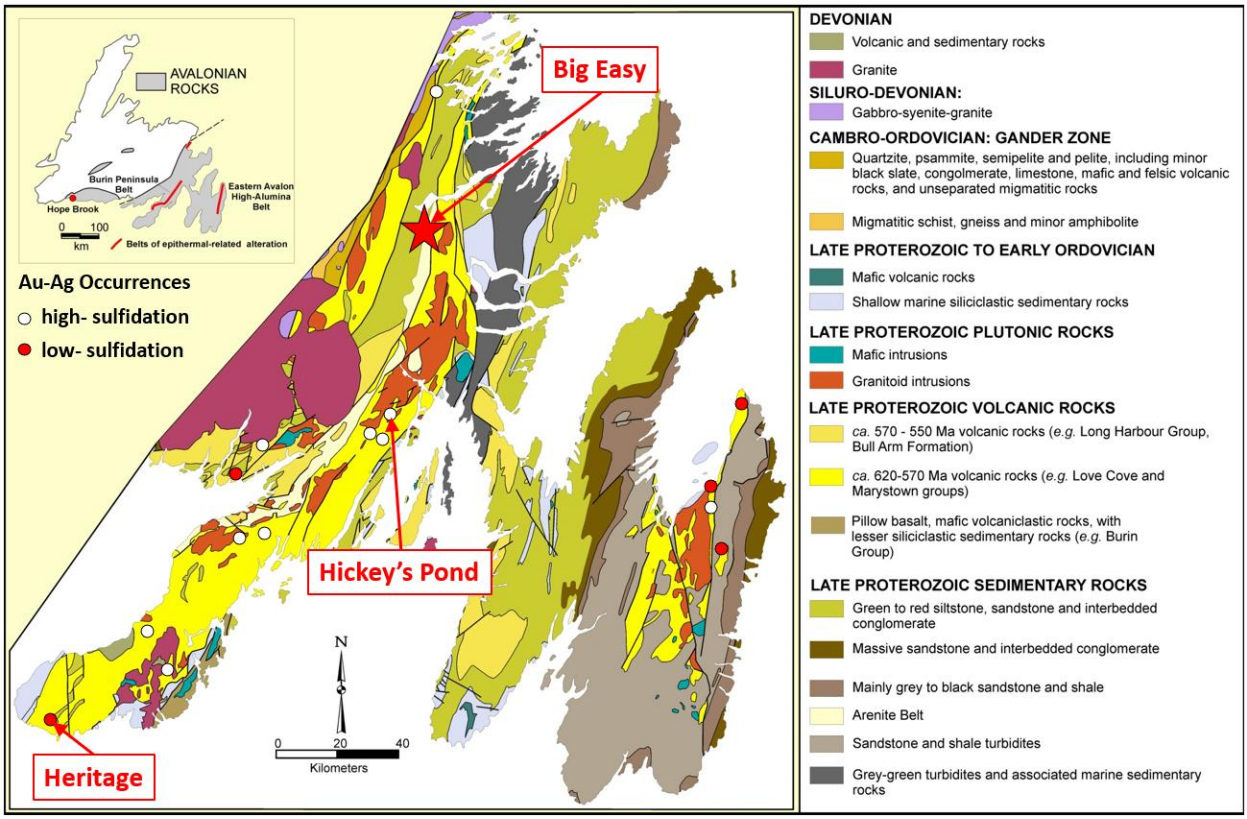

Figure 2.2 Geological map of the Avalon Zone showing known occurrences of porphyry-style and epithermal mineralization. The Burin Peninsula-Bonavista Bay region ("western Avalon Zone") contains two broad northeast-southwest trending belts (in yellow) predominated by the ca. 620-570 Ma volcanic rocks of the Love Cove (western belt) and Marystown (eastern belt) groups, and associated granitoid plutons (orange-red). These two belts are separated on the map by Neoproterozoic sedimentary rocks of the Musgravetown Group (in green) and the subsidiary Grandy's Pond Arenite Belt (cream). The bulk of recognized epithermal precious metal prospects (including Hickey's Pond and Heritage) are hosted within volcaniclastic rocks of the Marystown Group (Burin Peninsula belt in inset). The Big Easy prospect is the only epithermal occurrence currently recognized within the mapped extent of the Musgravetown Group. A small number of epithermal prospects are also recognized hosted in the younger (ca 570 -550 Ma) Long Harbour Group volcanic rocks (mustard yellow) along the eastern edge of the main map frame. Figure

modified from Sparkes et al., 2016 (after O'Brien et al., 1998). Reproduced with permission (see Appendix 1).

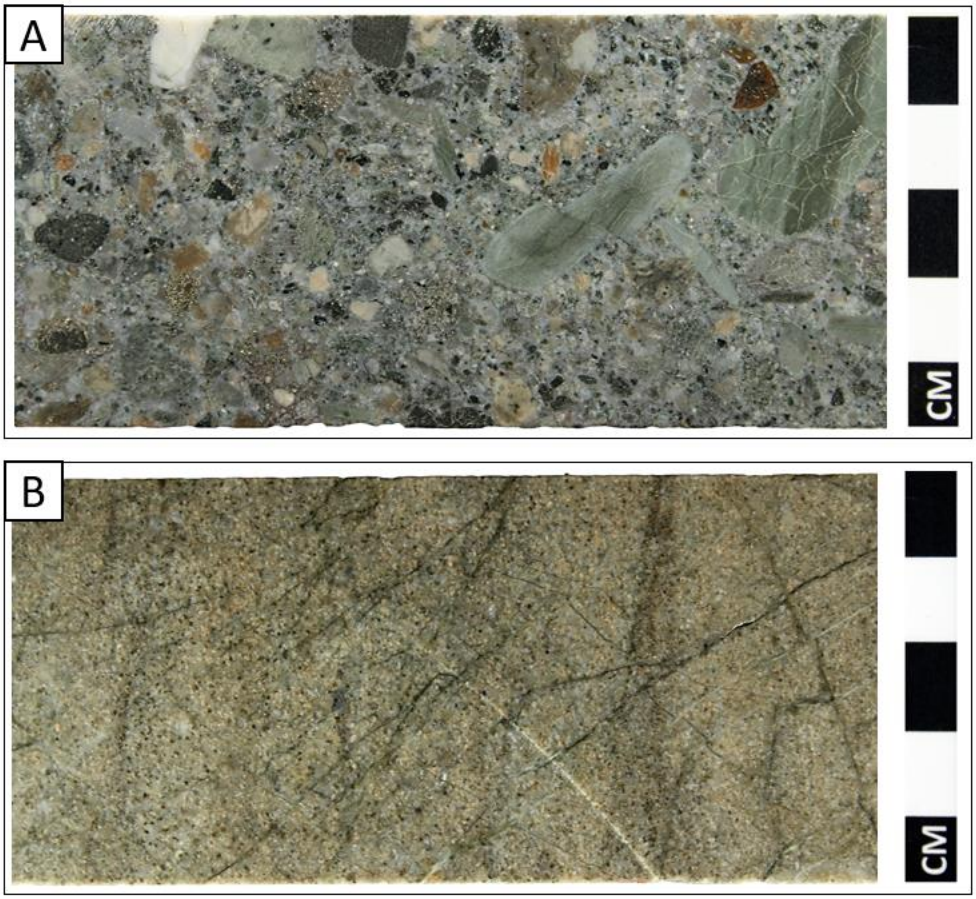

Figure 2.3 Epiclastic rocks hosting the Big Easy prospect: A) Polymictic conglomerate showing sedimentary and volcanic clasts in a matrix of the same composition; and B) Pale green altered sandstone exhibiting multidirectional chlorite-rich vein alteration.

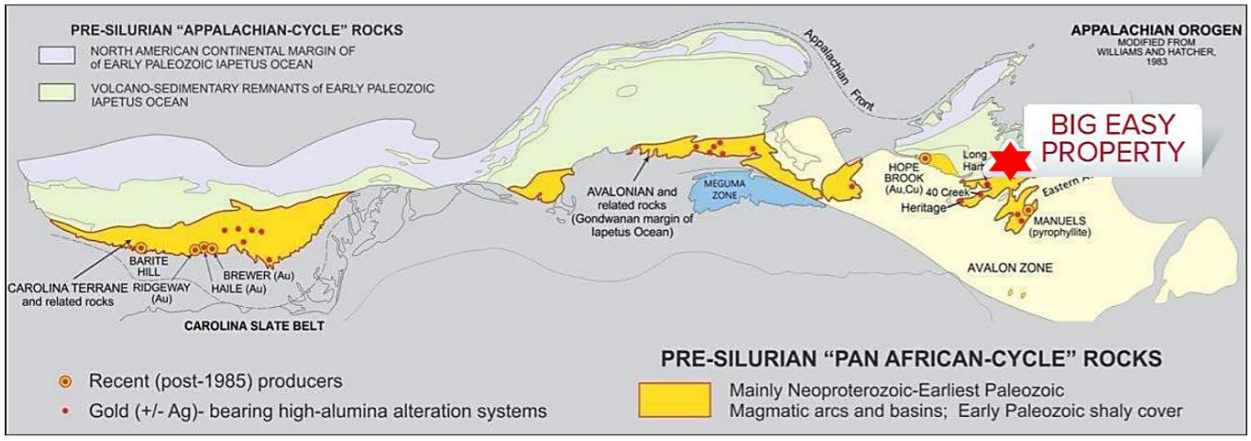

Figure 2.4 Pre-Silurian "Pan African-cycle" rocks of the Appalachian orogen (shown in golden yellow). These include the Avalon Zone in Newfoundland (host of the Big Easy prospect), Avalonia (Nova Scotia, New Brunswick, and New England), and the Carolina Slate Belt (host of the Haile deposit). Figure modified after Williams & Hatcher, 1983. Reproduced with permission (see Appendix 1).

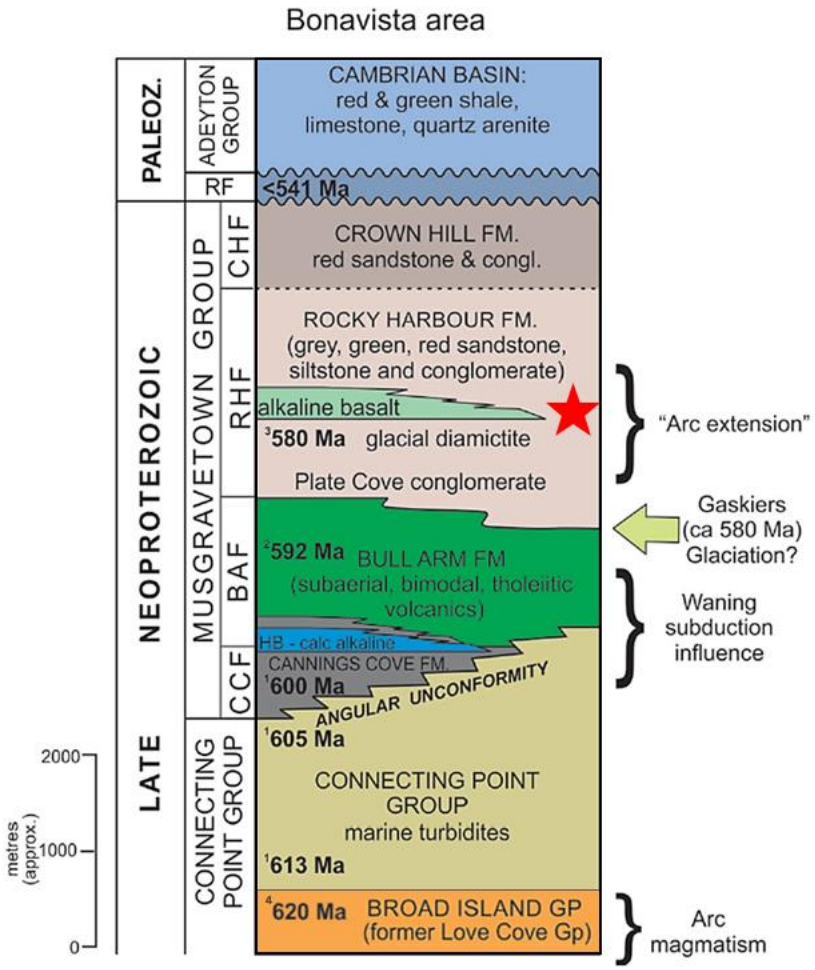

Figure 2.5 Schematic lithostratigraphic columns for Eastport, Bonavista, and Isthmus of Avalon areas of the Avalon Terrane in Newfoundland. Figure modified from Mills et al., 2021. Bedrock age dates from [1]Mills et al., 2016; [2]Mills & Dunning, 2017; [3]Pu et al., 2016; and [4]Mills et al., 2021. Gaskiers glaciation age date from Retallack, 2013. BAF, Bull Arm Formation; CCF, Cannings Cove Formation; CHF, Crown Hill Formation; RHF, Rocky Harbour Formation; HB, Calc-alkaline basalts; RF, Random Formation (Paleozoic; mainly quartz arenite). The red star shows the inferred age of the Big Easy prospect (ca 573 Ma), as discussed in text. Reproduced with permission (see Appendix 1).

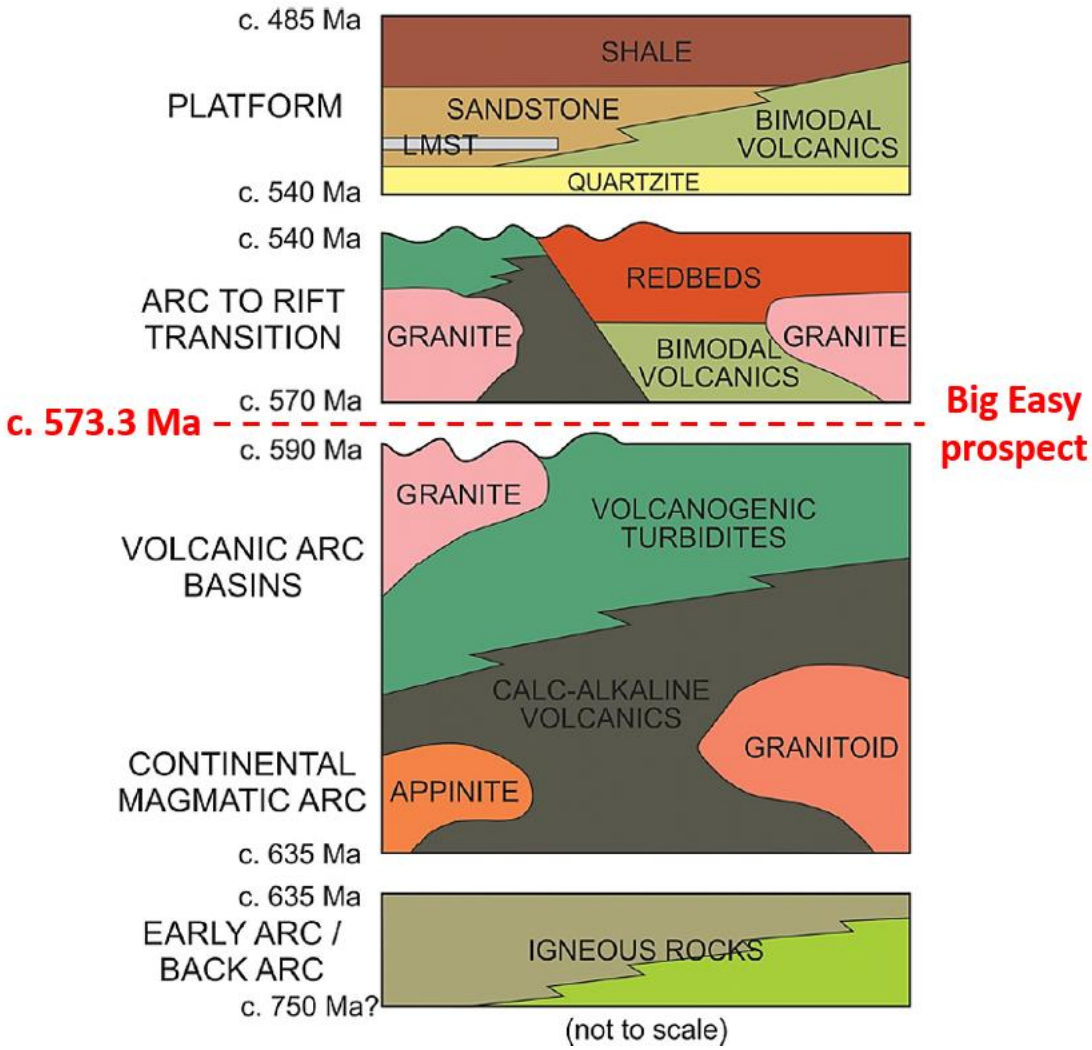

Figure 2.6 Tectonostratigraphic evolution for the Neoproterozoic–lower Paleozoic rocks of Avalonia and its association with tectono-magmatic events. Big Easy age and tectonostratigraphic position are displayed (Ferguson, 2017). Figure modified from Murphy et al., 2019. Reproduced with permission (see Appendix 1).

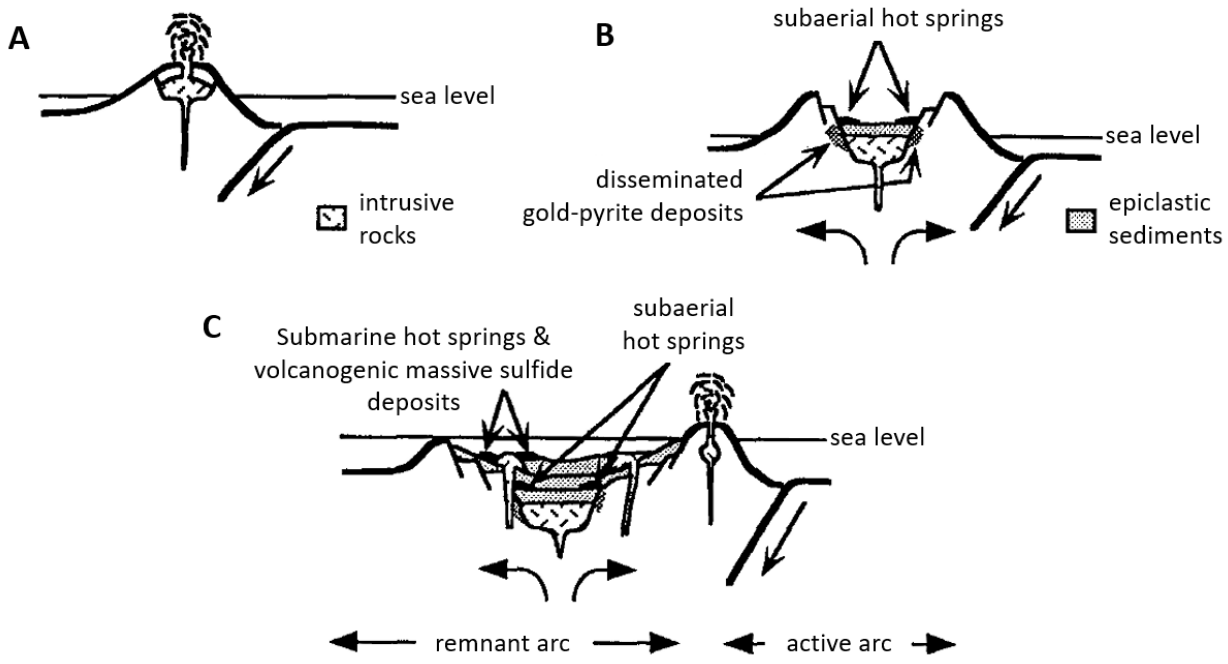

Figure 2.7 Generalized model showing arc tectonic and metallogenic evolution for an epithermal environment analogous to the Big Easy prospect. A) Coeval expansion and cessation of arc volcanism in a major andesitic to rhyolitic pyroclastic eruption; B) Development of an extensional basin within a continental volcanic arc environment, followed by rapid subsidence and sedimentation of epiclastic sediments. At Big Easy, the known Au-Ag mineralization is observed as post-indurational veins that traverse the epiclastic sediments themselves, rather than disseminated gold-pyrite as drawn by Feiss for the Carolina Slate Belt example; C) Continued extension and subsidence result in burial and preservation of pyroclastic sequences and epithermal ore deposits in epiclastic rift-fill sediments derived from active and remnant arc. Volcanogenic Massive Sulfide deposits, as shown in the figure, have not been documented in the this time interval in the Avalon Zone. Figure modified from Feiss et al., 1993. Reproduced with permission (see Appendix 1).

Chapter 3: Mineralogy, geochemistry, and hydrothermal alteration of the Big Easy low-sulfidation epithermal system: Constraints from SEM-MLA imaging, geological modeling, and fluid inclusion microanalysis

Abstract

The Burin Peninsula contains most of the western portion of the Avalon Zone in Newfoundland. Late Neoproterozoic volcanic, plutonic, and sedimentary rocks host numerous low- and high-sulfidation epithermal gold prospects in the region. Most of these are hosted in penecontemporaneous pyroclastic rocks derived from the same arc-related magmatism that fostered the parent hydrothermal systems. The Big Easy low-sulfidation epithermal Au-Ag system is situated in the northern part of the Burin Peninsula, close to the town of Clarenville. The mineralization here is hosted in epiclastic sandstones and polymictic pebble conglomerates of the Musgravetown Group, rather than the primary volcanic/volcaniclastic hosts of other known epithermal occurrences in the Avalon Zone (such as those within the Marystown Group). The well-preserved epithermal system at Big Easy is dated as Late Neoproterozoic (ca. 573 Ma), and the vast majority of volcanic/volcaniclastic-hosted occurrences on the Burin peninsula have returned dates of 569-585 Ma as well. These Neoproterozoic ages are quite unusual globally, with the majority of epithermal deposits recognized worldwide having Cenozoic ages. The mineralized zone at Big Easy is characterized by hydrothermal brecciation, diverse vein textures, pervasive silicification and pyritization of the host rocks, and vein selvages containing quartz, adularia, chlorite, illite, sericite, and carbonate. Four different Au- and Ag-bearing vein styles are

recognized, based on ore mineral assemblage and Au-Ag content: Type I) Electrum dominant (High Au) – (pyrite + electrum ± sphalerite); Type II) High Au:Ag – (pyrite + electrum + native silver + naumannite + acanthite ± aguilarite ± chalcopyrite ± uytenbogaardtite); Type III) Ginguro (High Ag:Au) – (native silver + acanthite + electrum ± pyrite ± aguilarite ± chalcopyrite ± freibergite-tetrahedrite,); and Type IV) Molybdenite-rich (molybdenite + native silver + acanthite ± pyrite ± chalcopyrite ± sphalerite). The predominant deportment of gold as electrum is mainly observed in grains attached and enclosed to pyrite crystals. Geological and numerical models were produced from existing drill hole data to compare the gold, silver, molybdenum, and arsenic distributions and illustrate the predominant ambient hydrothermal alteration zones present in the preserved epithermal system. Fluid inclusion microthermometry and SEM imaging were used to characterize the mineralogical and textural features of each vein style, as well as the estimated fluid temperatures and salinities (from 124.7 °C to 321.15 °C, and from 0.18 to 2.74 wt.% NaCl eq., respectively).

Low-sulfidation Au-Ag deposits are a significant source of these metals globally. Big Easy, and other occurrences in the Avalon Zone, are a testament that mineral exploration for preserved epithermal deposits hosted in pre-Cenozoic rocks should not be neglected.

3.1 INTRODUCTION.

The Big Easy Au-Ag prospect contains relatively low-temperature ore minerals mainly deported in quartz-adularia-pyrite veins and breccias that are hosted within extensively pyritized-silicified epiclastic sedimentary rocks. Surface exposure of ore mineralization at Big Easy is sparse, and

consequently most of this study was conducted using drill core. Characterization of vein and wallrock alteration assemblages was performed using petrography and SEM-BSE imaging techniques, resulting in the recognition of four distinct vein assemblages distributed within the system. Based on this assemblage classification, a representative subset of samples was selected for fluid inclusion microthermometry. Gold-bearing mineral grains were analyzed by SEM-MLA to characterize gold deportment and textural features relative to host minerals.

Geological and numerical modeling for gold, silver, molybdenum, arsenic, and hydrothermal alteration envelopes was performed on descriptive core logging and assay/geochemical analysis results available from diamond drilling on the Big Easy property carried out by Silver Spruce Resources Inc. Additionally, using geochemical results acquired from these programs, and from additional drilling programs carried out by Cartier Iron Corp. in 2018 and 2021, a Principal Component Analysis (PCA) was performed for ten significant metallic elements: gold, silver, arsenic, molybdenum, iron, copper, lead, antimony, selenium and zinc.

3.2 SAMPLES AND ANALYTICAL METHODS.

Core samples from drilling programs carried out on the property by Silver Spruce Resources Inc. from 2012 to 2015 were studied by hand and thin sections. These archived samples had been chosen to emphasize intersections where ore minerals occurred in significant quantity confined in discrete veins, and those that returned high Au and/or Ag values from Au fire assay and/or ICP geochemical analyses performed during the original exploration assessment. Additionally, a representative surface hand specimen exhibiting silica sinter layers was examined and described.

Principal Component Analysis (PCA) was used to interrogate the database of geochemical analyses from the exploration drill core. The original database comprised 4269 geochemical analyses of specific core intervals derived from filed assessment reports of Silver Spruce Resources Inc. (DeLazzer, A. & Dimmell, P., 2012; Dimmell, P., 2012; Dimmell, P., 2015). These data are provided in digital form in Appendix 2. PCA was applied to reduce the original data's dimensionality and describe most of the variance without losing information (Walden et al., 1992; Zhou et al., 1983). The analysis was deployed to detect multi-element associations, their relationship to known ore mineral assemblages, and their potential for mapping zoning. Before inputting the data into the PCA analysis section of the ioGAS-64 software, and once the original database was organized and filtered, a Centre Log Ratio-Transformation (CLR) was performed to minimize possible effects from closure and outliers. This CLR procedure was also performed with ioGAS-64.

Scanning Electron Microscopy (SEM) and Mineral Liberation Analysis (MLA) was conducted in the CREAIT MAF (Microanalysis Facility) SEM Lab at Memorial University using an FEI MLA 650FEG instrument (Fig. 3.1), equipped with a Field Emission Gun (FEG) electron source and Bruker dual high-throughput energy-dispersive X-ray spectroscopy (EDX) detectors. SEM-BSE (Back Scattered Electron) imaging and SEM-EDX microanalysis were used to supplement observations made using petrography, as well as identify ore assemblages, provide semi-quantitative chemical compositional information, and aid in the description of the texture and paragenesis of mineral phases whose size was smaller than the resolution of an optical microscope. This instrument is also equipped with Mineral Liberation Analysis (MLA) software capability (Gu,

2003), which was used to derive information about ore mineral grain size and shape, digital textural maps, nature of grain boundaries in complexly intergrown minerals, and quantitative evaluation of abundances and mineral associations.

Based on the SEM analysis, core sections that clearly displayed the main characteristic vein mineral assemblages were selected to produce double-polished sections to perform fluid inclusion microthermometry. Vancouver Petrographics prepared ten doubly-polished thin sections with 60 µm thickness. Fluid inclusion analysis and temperature measurements were conducted using a Linkam THMSG600 heating freezing stage, mounted on an Olympus BX51 microscope with 4x, 10x, 50x, and 100x Olympus long-working distance objective lenses. This equipment allows microthermometric observations of phase changes over the range of -193 to + 600 °C. Images of fluid inclusions shown herein were obtained using a QImaging Rolera-XR camera and QCapture software.

Before measurements of Big Easy samples, a calibration of the Linkam stage was made using Syn Flinc synthetic fluid inclusions (Sterner & Bodnar, 1984). Three reference samples were measured: 1) H_2O-CO_2 system, triple point (-56.6 °C); 2) Pure H_2O, freezing point (0.0 °C) and critical point (374.1 °C); and 3) H_2O-NaCl, final ice melting (-10.7 °C). Additionally, heating and freezing ranges and rates were pre-set for the LINKAM TMS 94 temperature programmer and LNP 95 nitrogen controller, as follows:

From room temperature to -120 °C:	10 °C/min
From -120 °C to -50 °C:	10 °C/min
From -50 °C to 10 °C*:	2-5 °C/min

*range for first and final melting ice temperatures observation

From 10 °C to 100 °C: 10 °C/min

From 100 °C to 300 °C**: 2-5 °C/min

**range for observing homogenization temperature

Fluid salinities and pressures were calculated from observational data using the BULK V. 01/03 software from FLUIDS "Package of computer programs for fluid inclusions studies" (Bakker, 2003) and the sowatflinc_inclusion version 2007 (Driesner & Heinrich, 2007). Input data included the first ice melting temperature, the system type [e.g., H_2O, H_2O-NaCl, H_2O-CO_2], the homogenization temperature, and the phase into which each fluid inclusion homogenized.

3.3 RESULTS.

3.3.1 Mineralogy, alteration, and textural features.

A variety of macroscopic hydrothermal textures were observed in rock samples from Big Easy, including siliceous sinter, crustiform and cockade veins, and breccias.

A sample exhibiting sinter layers was collected at the surface at Big Easy (Fig. 3.2A). A portion of the sample shows the finely layered texture characteristic of cyclical deposition from near-surface hot spring activity. The original down-to-up direction can be determined observing the curvature of the layers (from left to right in figure 3.2A). Dark gray material covering layered sinter is heavily silicified polymictic epiclastic sandstone-conglomerate.

Breccias in Big Easy are comprised of angular fragments of greenish volcano-sedimentary rocks altered by chlorite and sericite minerals, cemented by milky to dark gray quartz (Fig. 3.2B, C). Breccias observed in drill cores are interpreted to be hydrothermal-type, consequent of a fracturing process during the interaction between rocks and over-pressured hydrothermal fluids.

Crustiform textures represent the most common disposition of quartz-adularia veins in the Big Easy prospect (Fig. 3.2D, E). This texture is characterized by successive, narrow, and subparallel bands, distinguished by contrasts in texture or mineral composition (Dong et al., 1995). These textures represent one of the most prospective features in low-sulfidation epithermal deposits because of their primary origin and metal precipitation significance. They originate from changes in fluid conditions, such as cooling, mixing of two fluids, reactions between wall rocks and the fluid, and boiling (Buchanan, 1981; Dong et al., 1995). At Big Easy, crustiform texture veins comprise narrow width (5 mm or less) quartz, chalcedony, and adularia bands disposed in a centro-symmetrical arrangement (Fig. 3.2D, E). In core specimens and petrographic observations, ore minerals are usually located along the center of the band, surrounded by tiny comb quartz crystals. The presence of crustiform texture is commonly associated with elevated gold and silver values in the Big Easy prospect.

Cockade textures are also observable in Big Easy drill cores (Fig. 3.2F). These comprise concentric crustiform bands of massive pyrite surrounding isolated fragments of wall rocks (e.g., silicified mudstone) and early quartz/chalcedony veins. These textures form due to the separation of rock fragments in a loose breccia by the force of growing crystals from the hydrothermal fluid pulses

(Adams, 1920). Hydrothermal brecciation observed in Big Easy frequently displays cockade textures, as brecciation allowed a pathway for the deposition of silica minerals, mainly quartz and chalcedony, around fragments of previously chlorite/sericite altered wall rock (Fig. 3.2B; Dong et al., 1995).

Certain repetitive and diagnostic rock alterations are consistently exhibited in the Musgravetown Group host lithologies (Fig. 3.3). In polymictic conglomerates, chlorite represents the most common and pervasive alteration (Fig. 3.3A), routinely affecting the surfaces of both volcanic and sedimentary clasts. In some strongly altered conglomerates, chlorite is also associated with disseminated euhedral pyrite crystals and quartz, formed before the main vein mineralizing processes occurred (Fig. 3.3B). In fine-grained host rocks, such as mudstones, chloritization is not common. Instead, strong silicification, characterized by densely packed arrays of quartz veins and pervasive silica alteration is dominant. Likewise, successive arrays of quartz-adularia veins are also a common feature. (Fig. 3.3C, D). Similar crustiform bands and prismatic aggregates of fine-grained adularia occur in some quartz-chalcedony veins in the deeper parts of other sediment-hosted/sediment-covered epithermal deposits (e.g., Fruta Del Norte, Ecuador, Leary et al., 2020). It is also common to observe the presence of large volcano-sedimentary clasts completely chloritized, pyritized, and oxidized, surrounded by late quartz, suggesting a large volume silicification process (Fig. 3.3E). Secondary minerals of alteration also include subhedral carbonate crystals embedded in chloritized volcanic rock fragments (Fig. 3.3F). In contrast to other low- to intermediate-sulfidation deposits, where carbonate crystals are mainly of manganoan composition (e.g. rhodochrosite in Fruta Del Norte in Ecuador, Leary et al., 2020; and Masara

Gold District in the Philippines, Gabo-Ratio et al., 2020), at Big Easy carbonate is predominantly calcite.

3.3.2 Ore mineral assemblages and mineralization style.

As imaged and characterized by SEM-BSE-EDX, gold and silver occur in their native state, as Au and Ag sulfides (and the Au-Ag sulfide uytenbogaardtite (Ag_3AuS_2)), selenides (Ag), sulfosalts (Au, Ag), and rare tellurides (Ag, Pd). These minerals typically form micron-sized inclusions within pyrite and chalcopyrite or are disseminated within quartz or adularia.

Gold occurs in electrum (Au-Ag alloy), and in rare uytenbogaardtite. Gold as electrum/uytenbogaardtite occurs in five forms: Attached, fracture controlled, enclosed, exposed, and free (shown schematically in Figure 3.4). Of the 140 gold-bearing grains enumerated by MLA, 62% were found attached to pyrite grains, 17% enclosed by pyrite, 10% as free grains, and 7% exposed from within pyrite crystals (Fig. 3.5B). There is a strong association between electrum and pyrite, and their geochemical association within vein-mineralizing fluids. The size for more than 70% of electrum grains ranges from 0.6 to 4 μm with a few larger grains of >4-30 μm (Fig. 3.5A).

Four distinct ore mineral assemblages localized in veins were identified using hand samples, petrographic, and SEM analysis (Table 3.1; Fig. 3.6). These veins are mainly part of crustiform sequences and represent the dominant gold and silver mineralization style within the Big Easy prospect. Some minor, narrow (cm-scale) disseminated areas of these same ore minerals were also

observed proximal to veining assemblages. Gold is predominantly deported as electrum, containing variable Au:Ag ratios. Silver is predominantly deported as native silver, silver sulfide (acanthite), and sulfo-selenides (naumannite, aguilarite), as well as minor freibergite-tetrahedrite.

3.3.2.1 Vein Type I - Electrum dominant (High Au).

The ore mineral assemblage is characterized by electrum, pyrite (FeS_2), and sphalerite ((Zn, Fe)S). Most electrum grains occur attached to euhedral to subhedral pyrite crystals, interstitial to clusters of pyrite crystals, or as free grains floating in the vein matrix (Fig. 3.7). Alteration minerals mainly comprise quartz and carbonate, with minor sericite. Pyrite in close textural association with sphalerite is not associated with electrum, suggesting a separate low-Au pyrite-sphalerite generation in these veins or a remnant assemblage from earlier wall rock pyritization. Electrum grains range from slightly less than 0.5 µm to 10 µm in size. This vein type contains the highest assay values of gold recorded to date. The 1 m drill interval that contained the main example of this type of vein (sample BE11-7 43.5) returned gold values of 7645 ppb, along with relatively low silver (10 ppm), low arsenic (30 ppm), molybdenum (18 ppm), antimony (<5 ppm) and copper (6 ppm).

3.3.2.2 Vein Type II - High Au:Ag.

Vein Type II contains a more complex and variable assemblage of ore minerals (Fig. 3.8). Gold is deported mainly as isolated electrum grains (Fig. 3.8A, B). These are coarser than in type I (reaching 20-30 µm). Gold is also deported in vugs or pores within seleniferous acanthite as uytenbogaardtite (Ag_3AuS_2; Fig. 3.8C). This complex assemblage also contains acanthite (Ag_2S),

native silver (Ag), naumannite (Ag_2Se), and aguilarite (Ag_4SeS) (Fig. 3.8D), as well as pyrite (FeS_2) and chalcopyrite ($CuFeS_2$) (Fig. 3.8A, D). In contrast to the type I veins, pyrite crystals tend to be anhedral, displaying irregular shapes and a spongy-porous texture (Fig. 3.8A). Alteration minerals are mainly comprised of quartz and sericite/illite. The drill intervals that contained this type of vein returned gold values of 421-6229 ppb, silver (70.6-98.7 ppm), arsenic (45-219 ppm), molybdenum (37-34 ppm), antimony (<5 ppm), and copper (12-28 ppm).

3.3.2.3 Vein Type III - Ginguro (High Ag:Au).

The most widespread vein type recognized in the archived drill core is type III Ginguro-style (Fig. 3.6C). The "Ginguro" (or "Silver-Black") vein texture was initially described in the Sado Au-Ag mine, Sado island, Japan, as black bands or streaks, where silver sulfides are predominant (Mukaiyama, 1950). In tis vein type, the pyrite content is less pronounced and silver minerals are more prominent (Fig. 3.9). The main assemblage comprises relatively coarser-grained native silver (30-50 μm), with acanthite and aguilarite (Fig. 3.9A, B, D). Other minerals include chalcopyrite ($CuFeS_2$), argentiferous chalcopyrite (Ag-chalcopyrite), and minerals from the freibergite–tetrahedrite series ($([Ag_6]^{4+}((Cu, Ag)_4\mathbf{C}^{2+}_2)Sb_4S_{12}S_{0-1}$ to $Cu_6(Cu_4\ \mathbf{C}^{2+}_2)Sb_4S_{12}S$, where $\mathbf{C}^{2+}$ is mainly represented by Fe^{2+} and Zn) (Fig. 3.9C). The predominant non-ore vein mineral observed is quartz. The drill intervals that contained this type of vein returned the highest silver values recognized in Big Easy (1094 ppm), along with gold (1909-9967 ppm), arsenic (20-74 ppm), antimony (<5 ppm), molybdenum (20-29 ppm) and copper (11-45 ppm).

3.3.2.4 Vein Type IV - Molybdenite-rich.

Type IV represents the only vein type where electrum was not observed. It is characterized by abundant molybdenite (MoS_2), ranging from a feathery texture around pyrite (Fig. 3.10A), which is the most dominant, to mottled grains of Fe-rich molybdenite (Fig. 3.10B). The ore mineral assemblage also includes pyrite + acanthite + chalcopyrite + native silver ± sphalerite (Fig. 3.10A-D). The non-ore vein minerals include quartz, adularia, and titanite (Fig. 3.10A-D). The 0.2 m drill interval that contained the best example of this type of vein (sample BE14-18 120.3) returned gold values of 1729 ppb, silver (34.3 ppm), arsenic (118 ppm), molybdenum (7220 ppm), antimony (<5 ppm) and copper (16 ppm).

Cross-cutting relationships between veins of different types were not clearly observed in the existing sample set, either in core sample or in petrography or SEM-BSE imaging. Therefore, relative timing between them cannot be determined with certainty. However, the mineral assemblage and paragenetic sequence for each vein type described here are summarized in Figure 3.11. In type I, euhedral to subhedral pyrite is the predominant mineral in the vein and the first that occurs, followed by anhedral sphalerite, which fills fractures in pyrite. Later anhedral electrum occurs attached to pyrite and occupying spaces between clusters of pyrite grains. Electrum is paragenetically later than sphalerite. In type II, anhedral pyrite and chalcopyrite are the earliest minerals, followed by acanthite. A characteristic association of naumannite, aguilarite, and acanthite suggests that these minerals were introduced in the same mineralizing pulse(s) and postdate earlier pyrite/chalcopyrite. Electrum occurs only as isolated grains and does not seem to be paragenetically associated with silver minerals, suggesting an even later introduction. Gold mineralization is also observed as minor uytenbogaardtite included within acanthite. In type III,

tiny (few μm) electrum grains appear to have been introduced in the earliest stage, and they are surrounded by later acanthite and chalcopyrite. Acanthite and native silver are closely associated, forming larger subhedral clusters, suggesting they were introduced at the same time. Freibergite-tetrahedrite constitutes a later mineral phase, surrounding and possibly replacing earlier chalcopyrite. Finally, in type IV, early subhedral pyrite grains are surrounded by feathery molybdenite, which represents the most abundant ore mineral in this vein type. A later progression comprises euhedral chalcopyrite crystals surrounded, and partially replaced, by anhedral acanthite and native silver.

3.3.3 Principal Component Analysis (PCA).

The ten elements essential to the characteristic ore minerals described above for the vein types at Big Easy (Fig. 3.11) were taken as variables to perform correlation and PCA analyses: Au, Ag, Mo, Fe, Cu, As, Sb, Se, Zn, and Pb. The full available set of 4269 analyses were utilized after applying a few basic filters: 1) for any value that was recorded as below the minimum detection limit, that value was represented by the (stated minimum limit of detection)/2; 2) for any value that exceeded the maximum detection limit (and for which no supplementary analysis was provided), that value was represented by the stated maximum detection limit; 3) for any analysis run in duplicate, these data were represented by a single record representing the mean of the duplicates.

The Pearson correlation coefficient table (Fig. 3.12) represents a measure of linear dependence between quantitative random variables (i.e., the ten elements selected here from the geochemical results database) and is an important primary tool for examining this type of data (e.g., Brueckner

et al., 2015; Ghezelbash et al., 2019). A coefficient of 1 means a total positive correlation, -1 is a total negative correlation, and 0 represents no correlation between the variables. The Pearson coefficient values for Big Easy display a robust positive correlation between gold and silver (Au-Ag; 0.68) and a strong negative correlation between iron and gold (Fe-Au; -0.33) and iron and silver (Fe-Ag; -0.37). Other significant correlations (> ±0.25) include positive correlations for As-Au (0.55), As-Ag (0.50), As-Mo (0.49), Mo-Ag (0.42), Mo-Au (0.35), and Fe-Zn (0.54), and negative correlations for Ag-Zn (-0.27), and Au-Zn (-0.29). These element correlations are also displayed in PCA biplots (Fig. 3.13 and 3.14).

PCA biplots represent a quantitative means to visualize the relationships between samples and chemical elements. Two separate sets of four biplots are shown here (Fig. 3.13 and 3.14), with 1) Symbols coded by Au concentration ranges, and 2) Symbols coded by Ag concentration ranges. This method allows the visualization of individual samples and populations with high Au-Ag values and their relationship with chemical elements in the system. Additionally, a second subdivision was applied to each set of biplots. One set involved PCA of Au, Ag, As, Cu, Fe, Mo, Pb, Sb, Se, and Zn, and another of As, Cu, Fe, Mo, Pb, Sb, Se, and Zn (excluding Au and Ag). In this way, it is possible to examine the influence of gold and silver in the system and make a comparison between plots to relate the results with the mineral assemblages of the four vein types. Finally, two additional plotting symbol attributes were applied to samples (coloured symbols and bubble sizes), based on the concentrations of gold and silver.

Also shown are the scree plots (Fig. 3.15) for the PCA analyses. For the Big Easy analyses, all data analyzed can be reasonably explained using three Principal Components (PCs), suggesting a

relatively low heterogeneity or variability of the data. Scree plots for the two element sets used (in Figure 3.15A: Au, Ag, As, Cu, Fe, Mo, Pb, Sb, Se, and Zn; in Figure 3.15B: As, Cu, Fe, Mo, Pb, Sb, Se, and Zn, excluding Au and Ag), display similar cumulative total variances for the first three PCs (58.0% and 59.2%, respectively), but slightly different behaviours between the PCs. This is apparent in the respective PC 1 and PC 2 components generated, which in scree plot A) explain a higher cumulative variability compared to PC1 and PC2 of scree plot B).

3.3.4 Geological and numerical modeling.

Leapfrog Geo is a modelling software developed to provide an integrated workflow approach to building geological and numerical models. The software allows a 3D visualization of a dataset containing core logging information, alteration descriptions and numerical assay results. A general modeling of major alteration zones was performed using Leapfrog Geo 6.0 based on the descriptive core logs available from the 2011, 2012, and 2014 programs (DeLazzer, A. & Dimmell, P., 2012; Dimmell, P., 2012; Dimmell, P., 2015). Holes from the 2018 and 2021 programs were drilled in locations remote from the more densely drilled main area shown in the modelling. Alteration descriptions from the core logging activity by the exploration operators were extracted, classified, and organized to create an alteration database (Appendix 3). A generalized classification was performed to obtain four subsets of information described in the core logging activity: Overburden, silicification, chloritization, and mixed silicification-chloritization. Numerical modelling of geochemical assays for gold, silver, molybdenum and arsenic were performed using the same database presented in Appendix 2.

Silicification is the predominant and pervasive alteration in the upper parts of the prospect (Fig. 3.16). Multiple generations of quartz and chalcedony arranged in crustiform veins are visible in shallow levels (<100 m), as well as abundant adularia-sericite veins (Fig. 3.2). In deeper and mineralized levels (>~225 m below surface), silicification is accompanied by propylitic alteration, mainly represented by chlorite, minor calcite, and local adularia (Fig. 3.2 and 3.3). Finally, the lowermost zone is dominated by a pervasive chloritization, representing the effective footwall of the Au-Ag mineralized zone (Fig. 3.16).

In addition to the alteration model of Figure 3.16, numerical models for gold, silver, arsenic and molybdenum distribution were produced – to interrogate any zonation in these elements related to either vein distribution, or the composition of the volumetrically extensive envelope of silicification (Fig. 3.17, 3.18, 3.19, and 3.20). Models for gold and silver distribution using data from all five drilling programs –2011, 2012, 2014, 2018, and 2021– imply a larger prospective zone located to the southeast of Grassy Pond (Fig. 3.17). Additionally, numerical models for As and Mo distribution (Fig. 3.19 and 3.20) display a strong spatial relationship in this same southeast zone, forming envelopes around zones with higher Au and Ag. These models are broadly consistent with results presented in the Pearson correlation table, where Au and Ag are both strongly correlated with As and Mo (Au-As: 0.55, Au-Mo: 0.35, Ag-As: 0.50, and Ag-Mo: 0.42).

3.3.5 Fluid inclusion microthermometry.

Ten representative samples containing quartz ± adularia veining were selected for fluid inclusion microthermometry. Samples were classified based on the four recognized types of veins described

above, with an emphasis on those samples that had returned significant Au and/or Ag concentrations. Reconnaissance for measurable primary fluid inclusion assemblages was performed on the ten polished thin sections before final selection for fluid inclusion wafer preparation. Table 3.1 summarizes the information for each sample – sample number (i.e., assay tag number for interval), drill hole number (DDH #), depth of archived core sample, metal concentrations (for the assay interval), and vein type.

Microthermometry was performed on two-phase (liquid and vapor) primary fluid inclusions hosted by quartz or adularia (Table 3.2; Fig. 3.21). Liquid:Vapor (L:V) ratio ranges from 1:1 in the largest fluid inclusion from the type IV vein to as high as 5:1 in vein type II. Figure 3.22 shows the homogenization temperature range for each vein type, representing the minimum trapping temperature of the hydrothermal fluid (Rankin, 2004; Wilkinson, 2001). For interpretive purposes, it was assumed that fluids were trapped homogeneously, as is usually assumed in microthermometric studies where CO_2-rich systems are not recognized (Ramboz et al., 1982). Additionally, any bulk leakage was not directly considered, and possible compositional or volumetric variations in the fluid inclusions over geological time were deemed insignificant.

Fluid inclusion size in the samples examined ranges from 5 to 30 μm, with an average size of 15 μm for inclusions found in Type II, III, and IV (Fig. 3.21B, C, D). In Type I veins, the fluid inclusions were routinely smaller, with most of them 5 μm or less (Fig. 3.21A). This small average size may be a consequence of the predominance of adularia (versus quartz) as a host, and made it more difficult to obtain a high quantity of reliable measurements, despite the high population density of inclusions present. Quartz was the main mineral associated with Type II-IV veins and

hosted larger, more easily measurable fluid inclusions. For all vein types, primary liquid-rich fluid inclusions were selected for microthermometry.

Type I and II veins returned the lowest ranges of homogenization temperature, from 141.3 °C to 155.1 °C with a mean of 149.9 °C, and from 124.7 °C to 252.6 °C with a mean of 170.3 °C, respectively (Fig. 3.22). For type III veins, homogenization temperatures ranged from 132.6 °C to 276.9 °C with a mean of 198.8 °C. Finally, type IV veins returned the highest homogenization temperatures in the system, from 162.4 °C to 321.5 °C (with a single higher measurement of 344.3 °C; Fig. 3.23) and a mean of 215.5 °C. All inclusions measured homogenized to a liquid phase (L). Due to the small size of fluid inclusions in high-Au samples from vein type I, no boiling assemblages were observed (i.e., mixed L:V ratio assemblages that homogenized at a single temperature).

Fluid salinity (as equivalent to wt.% NaCl) was calculated based on the final melting temperature of ice and generated in the Package Fluids 1 software (Bakker, 2003). The temperature of the final melting point of ice ranged from -1.6 to -0.1 °C, with an average of -0.5 °C, across all vein types. The calculated salinities in Big Easy are generally low, ranging from 0.18 to 2.74 wt.% NaCl eq., with an average of 0.85% (Fig. 3.23; Table 3.2). Only three examples, from type III, contained salinities greater than 1.6 wt.% NaCl eq. (2.24-2.74 wt.% NaCl eq.). The average for all other samples was 0.73 wt.% NaCl eq. (Fig. 3.23).

3.4 DISCUSSION.

3.4.1 Mineralization processes.

In low-sulfidation systems, the ore-forming fluids circulate through rock fractures, and the mineralization is most often localized in those structures. Sometimes these fluids transit permeable lithologies (or even non-indurated sediments) leading to disseminated mineralization. However, no evidence of a disseminated mineralization style was found at Big Easy. Instead, all evidence suggests that Au-Ag mineralization at Big Easy is associated with veining of fully indurated (epiclastic) host rocks. The mineralization is predominantly localized in veins containing minor gold and silver minerals, and thus represents a structurally controlled style of mineralization (Fig. 3.3). Therefore, the wide zone of silicification and disseminated pyrite that demarcates the Big Easy Main Zone on the surface and is observable in the geological model (Fig. 3.16) was related to processes that predate Au-Ag veining. A possibly analogous mineralization style, where gold is hosted within silicified meta-sediments containing fine-grained disseminated pyrite, can be found at the Haile mine in South Carolina – the USA, a gold deposit located within the same extended Neoproterozoic terrane as Big Easy (Berry et al., 2016; Mobley et al., 2014). Although a disseminated style mineralization process has been proposed by these authors for Haile, the deposit also contains vestiges of what may be original discrete mineralized veins that have been disrupted by intense post-depositional polydeformation of the deposit.

3.4.2 Mineral associations and paragenesis.

Four different Au- and Ag-bearing vein styles are recognized, based on ore mineral assemblage and Au-Ag content: Type I) Electrum dominant (High Au) – (pyrite + electrum ± sphalerite); Type II) High Au:Ag – (pyrite + electrum + native silver + naumannite + acanthite ± aguilarite ± chalcopyrite ± uytenbogaardtite); Type III) Ginguro (High Ag:Au) – (native silver + acanthite + electrum ± pyrite ± aguilarite ± chalcopyrite ± freibergite-tetrahedrite); and Type IV) Molybdenite-rich (molybdenite + native silver + acanthite ± pyrite ± chalcopyrite ± sphalerite).

The vein textures described at Big Easy represent characteristic low-sulfidation epithermal features that can be found in deposits globally (e.g., Haile, USA; Pueblo Viejo, Dominican Republic; Marmato, Colombia; John et al., 2010). Bonanza-grade ore zones of epithermal Au-Ag deposits usually contain multiple generations of veins and textures, most often related to cyclical boiling processes – such as the crustiform and cockade textures described here for Big Easy –, and observable in other bonanza-type deposits (e.g. Fruta Del Norte, Ecuador; Leary et al., 2016, 2020). In Big Easy, these vein textures are exceptionally well preserved despite their Neoproterozoic age and are associated with the presence of sinter terraces, which further implies that known veins were located at less than 250 m from paleosurface, based on drilling to date. Additional hydrothermal features observed at Big Easy, such as stockwork veins, hydrothermal breccias, and sinter terraces, are also common in low-sulfidation epithermal deposits globally.

Silica sinter can be used as a prospective indicator of possible low-sulfidation epithermal activity in an area and reflects the surface expression of a deeper geothermal reservoir (Lynne, 2013;

Sillitoe, 2015). Silica sinter in Big Easy is overlain by heavily silicified polymictic epiclastic sandstone-conglomerate indicating an episodic deposition of epiclastic sediments in the surface hot spring environment. This in turn is covered by radiating silica that implies that surface hot spring precipitation resumed after the sediment influx. The original depositional textures can be preserved for millions of years, long after hot spring discharge ceases and throughout subsequent tectonic processes. Sinter forms in geothermal systems when near-neutral pH fluids discharge and cool at the surface, precipitating silica (Lynne et al., 2007; Slagter et al., 2019). Thus, sinter also provides a valuable stratigraphic marker for the paleotopographic surface. Sinter horizons have often been important in early exploration stages, such as in the case of Fruta Del Norte, where a significant sinter horizon at the base of a sedimentary cover sequence was described in the first drill testing carried out after the deposit discovery (Leary et al., 2020). Other outstanding and well-described examples of these classic hydrothermal features include the Favona vein in the Waihi deposit and Golden Cross in New Zealand, and Koryu No. 3 Au-Ag veins in Japan (John et al., 2010; Shimizu, 2014; Simpson et al., 2001).

At Big Easy, gold is deported as electrum in type I and II veins (and in far lesser abundance in type III - Ginguro veins). No electrum or native gold grains were observed in type IV veins, even using SEM-BSE. Silver is found in a high proportion to gold in vein types II, III, and IV, predominantly as native silver and acanthite. Discrete silver minerals were not observed in the electrum-dominant type I veins. These mineral associations strongly resemble those reported in other low-sulfidation deposits located in Japan (e.g., Hishikari Epithermal Gold Deposit, Ibaraki & Suzuki, 1993; Izawa et al., 1990; Tohma et al., 2010). Molybdenite, characteristic of type IV

veins, has been described at the Haile mine as fine-grained aggregates commonly visible in drill core samples, associated with large grains of pyrite and native gold (Mobley et al., 2014).

Some less abundant ore minerals recognized at Big Easy are also common to epithermal gold and silver deposits. Uytenbogaardtite was first described in Tambang Sawah, Benkoelen district, Sumatra, Indonesia, and the Comstock Lode, Storey County, Nevada, USA, two examples of hydrothermal Au-Ag quartz vein-style deposits (Barton et al., 1978). Uytenbogaardtite (Fig. 3.8C) at Big Easy is found in a typical low-temperature paragenesis, filling vugs in acanthite crystals. Similarly, naumannite (Ag_2Se) and aguilarite (Ag_4SeS) are characteristic of low-temperature hydrothermal deposits rich in silver and selenium but relatively deficient in sulfur (Petruk et al., 1974). The presence of these Se-bearing minerals can be explained as reflecting a high Se:S ratio in the parent fluids for these deposits (Kullerud et al., 2018). In epithermal deposits from the western USA, an assemblage of electrum and naumannite has been described as an indicator of strongly precious-metals-enriched ore-forming fluids, leading to the presence of remarkable bonanza grades – a notable example being the low sulfidation Sleeper deposit (Nevada; Saunders et al., 2010). The presence of base metal sulfides in Big Easy is relatively small. This is in contrast to some low sulfidation examples that also possess intermediate sulfidation zones, where galena, sphalerite, and chalcopyrite are more abundant (e.g., Fruta Del Norte in Ecuador; Leary et al., 2020).

Only 2% of drill hole samples assayed to date have returned values of more than 0.4 g/t Au (Fig. 3.24A). These data are displayed in the form of a gold histogram in Figure 3.24B, where vertical lines demarcate values of >0.4 g/t Au and >3.0 g/t Au (“Bonanza Zone”). Precious metals tenor at

Big Easy is mainly concentrated in electrum grains, and these have high Ag/Au ratios, as inferred from core assay results (Table 3.4). Based on all samples with (Au + Ag/65) >1 ppm (to emulate a cutoff grade of 1 g/t Au) Big Easy has a bulk Au:Ag ratio of approximately 1:33. This is displayed as a sloped line in Figure 3.25, along with symbols for all Big Easy samples meeting the cutoff criterion. Also plotted are ratio lines for epithermal Au-Ag deposits worldwide (Chizhova & Volkov, 2014) as well as for several important low-sulfidation deposits (Fruta Del Norte, Haile, and Hishikari). Despite similarities described between these deposits and Big Easy in Chapter 2, one marked difference can be observed in ore mineral associations, which is reflected in a disparity between Au:Ag ratios. These comparable deposits display similar Au:Ag ratios (1:1.6, 1:2.1, and 1:1.9, respectively), suggesting a smaller contribution from silver minerals in the mineralization style, and higher gold values. However, for the limited samples recognized as type I veins during the current study, where the content of silver minerals is low relative to the other vein types and there are higher gold values, the ratio increases to 1:1.3 (similarly to Fruta Del Norte), as is observed in Table 3.1, sample BE-11-7 43.5. This implies that Big Easy may have a generation of high Au:Ag veins that are under-represented in drill intersections to date.

3.4.3 Principal Component Analysis (PCA).

As described above in Results for PCA analyses, in Figure 3.13, symbols were coded by colour for the following characteristics: High gold (red) = Au > 0.4 ppm; and High silver (blue) = Ag > 10 ppm; High gold + silver (green) have both these characteristics and coded by diameter for Au concentration ranges: Small bubbles (<100 ppb), medium bubbles (100-400 ppb) and large bubbles (>400 ppb). In both RQ2 vs RQ1 and RQ3 vs RQ1 plots (Fig. 3.13A, B), samples with higher Au

(and/or Ag) values are, as expected, dispersed along clustered Au-Ag vectors, and lie almost exclusively in the positive RQ1 portion of the plots. However, there are some informative additional features apparent. There are pronounced Mo and As vectors subparallel to the closely paired Au and Ag vectors in both plots. Samples with values below the legend thresholds for Au and Ag are dispersed in an opposite direction along the Fe-Zn vector cluster into negative RQ1 space. In the RQ2 vs RQ1 plot, a population of high Au samples is dispersed toward an Sb(-Se) vector cluster. Likewise, without the direct influence of Au and Ag as variables (Fig. 3.13C, D), similar features are still apparent. In the RQ2 vs RQ1 plot, a subpopulation of samples with higher Au are dispersed toward an Sb(-Se) cluster (similarly to the behavior observed in A). Samples with higher Ag are dispersed in a direction along the Mo-As vector cluster. In the RQ3 vs RQ1 plot, the behavior and relationship between variables and samples are not as clear. In both RQ2 vs RQ1 and RQ3 and RQ1 plots, samples below the legend thresholds for Au and Ag are dispersed once again toward the Fe-Zn vector cluster.

In Figure 3.14, symbols were coded by colour as for Figure 3.13, and coded by diameter for Ag rather than Au concentration ranges: Small bubbles (<10 ppm), medium bubbles (10-100 ppm), and large bubbles (>100 ppm). In both RQ2 vs RQ1 and RQ3 vs RQ1 plots (Fig. 3.14A, B), there is some apparent dispersal of higher Ag samples along Mo and As vectors. Samples below threshold values are dispersed in an opposite direction toward Fe and Zn vectors. Additionally, in both RQ2 vs RQ1 and RQ3 vs RQ1 plots, Cu, Pb, Se, and Pb vectors do not exhibit a relationship (either positive nor negative) with samples with high Ag values. Without the direct influence of Au and Ag as variables, some useful details are more apparent (Fig. 3.14C, D). In the RQ2 vs RQ1 plot of C) there is a dispersal of higher Ag samples along the Mo (±As) vector. In the RQ3 versus

RQ1 plot of D) there is a small subpopulation of higher Ag samples dispersed along the Pb vector. Both plots show a small set of higher Ag outliers dispersed along the Cu vector.

PCA results and Pearson correlation analysis are consistent with ore mineral assemblages observed in SEM analysis, including: i) The predominant deportment of gold as electrum, where gold and silver are naturally occurring together in variable ratios, ii) The assemblages of vein types II and III, where additional gold- and silver-bearing minerals are present (Fig. 3.11), as well as a more complex assemblage of additional ore minerals, and iii) the presence of substantial pyrite (unrelated to subsequent vein mineralization) disseminated in the host rocks.

The negative correlation between Fe-Au and Fe-Ag is explained due to the pervasive presence of ambient pyrite throughout the epiclastic host rocks, which took place before or during the induration of the epiclastic sediments, and before the veins were emplaced in fractures in indurated rocks. This relationship is also observed for Zn, which is interpreted to be a minor element in this generation of pyrite. Pyritization of the epiclastic hosts (in surface ponds) can be considered a localized feature encompassed by the area of hydrothermal/geothermal activity in a broader intracaldera system that fostered the epigenetic mineralization. The pyritized host rock comprises a large volume envelope observed for vein mineralization and represents a useful tool for district-scale prospection and exploration.

Cu-Sb and Au have a negligible correlation. This implies that the process of Au enrichment in the veins was not uniformly linked to that for Cu, Se, and Sb, and vice-versa. For example, in type III veins, chalcopyrite and freibergite-tetrahedrite are paragenetically simultaneous with electrum. On

the other hand, a population of high Au samples is dispersed toward an Sb(-Se) vector cluster (Fig. 3.13A), implying a strong relationship for some samples. This behaviour is observed to a lesser degree for high Ag samples in Figure 3.14B, but appears dominated by the gold content. These observations might be explained by the characteristics of type II (High Au:Ag) veins. Se-bearing minerals are encountered in type II veins in close association with electrum, but the deportment of Sb in this vein generation is unclear, as there is no discrete Sb-bearing mineral recognized to date.

A strong correlation of Mo and As is observed in vectors resulting from the PCA analysis (Fig. 3.13A and 3.14A), in the Pearson Correlation table (0.49; Fig. 3.12), and in the comparative columns resulting from the drill hole correlation analysis (Fig. 3.26B, D). Although a contemporaneous paragenesis of As-bearing minerals (e.g., freibergite-tetrahedrite series) and molybdenite is not observed in the vein mineralization, As and Mo could comprise minor elements within vein pyrite. However, a more likely explanation is that they are minor elements within the pyrite disseminated in the silicified epiclastic host rocks. This relationship can also be inferred from the numerical modelling results (Fig. 3.19 and 3.20), where both elements exhibit an envelope shape covering similar volumes.

Exploration efforts in recent years have been focussed on the Big Easy Main Alteration Zone, once high gold values were found in 2011 and 2012 drilling programs (DeLazzer & Dimmell, 2012; Dimmell, 2012). Due to the intrinsically strong relationship between gold- and silver-bearing mineral assemblages, as documented with SEM analysis (Fig. 3.8), and their geochemical association and linear dependence observed in PCA (Fig. 3.13 and 3.14), most veins with high gold values also contained high silver values. This observation reinforces the idea of exploring Big

Easy as an epithermal gold and silver prospect. However, one object of interest for exploration is obviously a better understanding of the distribution of the different vein types described here – especially the high Au type I veins.

3.4.4 Fluid inclusion analysis.

Microthermometry was performed on two-phase (liquid and vapor) primary fluid inclusions hosted by quartz or adularia. These are the predominant gangue (non-ore) minerals present in mineralized veins, and it is assumed they formed at approximately the same time, temperature, and pressure as the associated ore minerals. Homogenization temperatures calculated from fluid inclusions suggest a relatively low-temperature mineralization system, typical of epithermal deposits. Overall, most Big Easy Au-Ag mineralization occurred between 140 °C and 250 °C (Fig. 3.22). However, electrum in the type I vein sample was deposited in a tighter and lower range, from approximately 140 °C to 155 °C. The type IV molybdenite-rich vein example was deposited at the highest temperatures observed, up to 344 °C. Finally, type II and type III returned wider ranges of intermediate temperatures, from 125 °C to 253 °C and 132 °C to 278 °C, respectively.

The pattern and trends observed in the homogenization temperatures suggest different pulses of hydrothermal fluid, of variable composition, circulating through the host rock structures over the life of the system. Figure 3.22 implies a hierarchy of increasing temperature for types I through IV. However, as discussed above, to date there are no samples that show definitive cross-cutting relationships between the four vein types, so it is not possible to establish a timing progression on this basis.

The temperature range from fluid inclusions suggests a marked influence of geothermal fluids and some mixing with localized meteoric waters that have percolated to the subsurface. In modern geothermal fields, fluid inclusions have highly variable vapor/liquid proportions, homogenization temperatures of generally <250 °C, and salinities <2 wt.% NaCl eq., like those observed in Big Easy (Canet et al., 2011; Etoh et al., 2002). For low-sulfidation systems like Big Easy, gold precipitation is believed to occur predominantly when the fluid boils as it approaches the surface; however, no evidence for boiling was found during fluid inclusions analysis. Boiling is characterized by the coexistence of liquid-rich inclusions and vapor-rich inclusions not associated with necking phenomena and other post-entrapment and disruptive processes (Camprubí & Albinson, 2007). Although this condition is not commonly found and difficult to detect/measure in low-sulfidation epithermal deposits due to the small size of inclusions and the uncertainty to obtain reliable measurements, at Big Easy there is indirect petrographic evidence suggesting the occurrence of boiling in the system. Boiling was likely present at Big Easy - but difficult to document through FI – based on textures observed in core samples, such as crustiform veins and sinuous to crenulated bands containing quartz and adularia (Dong et al., 1995; Fig. 3.2D, E), sinter presence and steam heated alteration zones.

Homogenization temperature represents the minimum temperature of the hydrothermal fluid entrapment (less than the true trapping temperature) because the pressure at which an inclusion is trapped is not known explicitly. Usually, a pressure correction (entrapment T (ºC) – homogenization T (ºC)) is necessary for minerals formed at high temperatures, from low salinity fluids, and at depths greater than 10 km (Potter, 1977). However, pressure correction is not

significant in deposits formed at low temperatures by shallow and low-salinity fluids, such as Big Easy (for average salinities of 0.85 wt.% NaCl eq. and average homogenization temperature of 183.4 °C, amounting to 1 degree or less; Potter, 1977). Additionally, considering that Big Easy veins were emplaced at a maximum interpreted depth of 250 m, along with observed low temperatures and salinities, any pressure correction can be considered negligible.

In this context, homogenization temperatures are an excellent approximation for shallow electrum-dominated systems (Shikazono, 1985), such as the Big Easy prospect. Homogenization temperatures and salinities for Big Easy are closely comparable to many low-sulfidation epithermal districts in Japan – including the well-known Hishikari Gold Deposit – as well as the Golden Cross Deposit in New Zealand, the intermediate-sulfidation Creede Mining District in Colorado, and examples of low- and intermediate-sulfidation epithermal deposits in Mexico, Romania, and Russia (Canet et al., 2011; Etoh et al., 2002; Izawa & Urashima, 1983; Mango et al., 2014; Prokof'ev et al., 2012; Robinson & Norman, 1984; Simpson et al., 2001; Volkov et al., 2012; Wallier et al., 2006). These deposits represent low-temperature and low-salinity epithermal deposits, with averages of 170 to 270 °C and 0.0 to 3.4 wt.% NaCl eq., respectively – with the exception that in some examples of intermediate-sulfidation deposits, such as Creede in the USA and Bolaños in Mexico, the salinity is higher, with an average of 6.5 and 8.3 wt.% NaCl eq., respectively. This higher salinity can be considered a characteristic of intermediate-sulfidation deposits and represents an important difference between these types (Table 3.3). The upper limit for homogenization temperatures in Big Easy is slightly higher than other comparative examples due to the single high temperature measured in type IV molybdenite-rich vein. However, the

average value of 183.6 °C for all homogenization temperatures obtained in this study is closely comparable to the other examples summarized here.

Concerning Table 3.3, the minimum homogenization temperature at Big Easy (183.4 ºC) is lower than for most of the comparable deposits. However, it resembles some worldwide epithermal deposits such as Todoroki and Koryu in Japan, uppers levels of Creede Mining District in the USA, and the Golden Cross deposit in New Zealand. On the other hand, the low salinity average value at Big Easy (0.18 wt.% NaCl eq.) is coincident with the majority of deposits summarized in Table 3.3, with values below 0.8 wt.% NaCl eq. These fluid inclusion results further document Big Easy as an example of a low-sulfidation epithermal Au-Ag system, despite its Neoproterozoic age.

3.4.5 3D Modelling and drill core correlations.

Observations from the 3-d numerical models (Fig. 3.17 to 3.20) are compatible with the Pearson Correlation table (Fig. 3.12) in showing a significant spatial correlation of Au-Ag with As-Mo. These relationships can be observed in Mo and As envelopes that closely encompass the high Au/high Ag envelopes, and represent a potential target enlargement tool for future drill planning and sample programs in the area.

Graphic logs that exemplify the mineralization style described for Big Easy, as well as its relationship with mineral alteration and host-rock lithologies, were compiled from existing core logs, and are displayed in Figure 3.26. Information such as core drilling code, depth, lithology, mineral alteration, and Au, Ag, Mo, and As contents were plotted to help visualize the

characteristics of the most prospective areas within the system. These models may prove useful in the design of further drilling exploration to enlarge the volumes and ore grades within the mineralization zone(s).

The example for vein type I: High Au was taken from hole BE11-07 (Fig. 3.26A). High gold mineralization is located within a 12 cm wide quartz-vein at 43.5 m depth within rocks affected by silica alteration. No significant amounts of silver and molybdenum were observed in this section. For vein type II: High Au:Ag, an example was taken from the hole BE14-19 (Fig. 3.26B). Gold and silver mineralization are located at 148.6 m depth in a host rock comprised of a silica-altered sandstone and conglomerate sequence. For vein type III: High Ag:Au (Ginguro) an example was taken from the hole BE14-13 at 226.5 m depth (Fig. 3.26C). This example is at the contact between a silica-altered sandstone sequence and a 4 cm wide layer of colloidal silica. Significant gold and silver were observed. Finally, an example for vein type IV: Molybdenite-rich was selected from hole BE14-18 at 120.3 m depth (Fig. 3.26D). The molybdenite-bearing vein was located within a silica-altered sandstone sequence, along with elevated gold and silver values. No discrete gold-bearing minerals were detected in this sample with SEM-BSE, but minor acanthite was present.

The element variograms in Figure 3.26 obtained for Au, Ag, Mo, and As reflect similar correlations noted in the Pearson correlation values and PCA analyses results. However, there are no obvious differences in host rock or broad alteration zone for the vein type examples presented in the graphic logs. Likewise, all four examples occur within the silicification zone, which is the predominant alteration in the upper parts of the system (around <200 m depth; Fig. 3.16). These characteristics

imply that forward exploration should incorporate an attempt to further delineate the structural deployment of the veins themselves, within the broad envelope of silicification and Mo and As enrichment.

3.5 CONCLUSIONS.

Multiple characteristics documented in this study, including i) a mineralization style dominated by crustiform/cockade veins and hydrothermal breccias, ii) an outer envelope of pervasive chlorite and silica alteration, iii) electrum associated with low-sulfidation mineral phases such as native silver-acanthite, iv) intact sinter found in the upper parts of the system and the presence of opaline silica in some veins ("chalcedony blanket"), and v) low temperature – low salinity fluids recorded in fluid inclusions, attest that Big Easy is a clear example of a low-sulfidation epithermal gold and silver prospect (Fig. 3.27). These features are exceptionally well preserved, despite the Neoproterozoic age. Overall, mineralization at Big Easy occurs as in stockwork veins (quite typical in other epithermal deposits), but these are hosted in silicified pyritized epiclastic host rocks (less typical than the usual volcanoclastic host rocks).

Four different Au- and Ag-bearing vein styles were identified within the system through petrographic and SEM analysis, each one with specific mineral assemblages: Type I) Electrum dominant (High Au) – (electrum, pyrite, sphalerite); Type II) High Au:Ag – (electrum, native silver, acanthite, naumannite, aguilarite, uytenbogaardtite, pyrite); Type III) Ginguro (High Ag:Au) – (native silver, acanthite, aguilarite, freibergite-tetrahedrite, pyrite); and Type IV) Molybdenite-rich (molybdenite, native silver, acanthite).

Gold is mainly deported as electrum grains, either attached to (62%) or enclosed by (17%) pyrite grains, or as free grains along the margins of mineralized veins (10%). The mean size range for electrum grains in the samples measured was from 1.1 to 2.0 µm, with some free grains reaching 30 µm. These data will be of particular value for any future geometallurgical assessment.

Homogenization temperatures obtained from fluid inclusions suggest a low-temperature mineralization system, typical of this type of deposit. Gold- and silver-bearing veins exhibited fluid temperatures ranging from 140 °C to 260 °C, and low salinities, between 0.18 and 2.7 wt.% NaCl eq., which are comparable to low-sulfidation epithermal examples in Japan, the United States, and New Zealand.

Based on all exploration drilling to date, Big Easy displays a nominally lower Au:Ag average ratio of 1:33, compared to the worldwide epithermal deposits average of 1:22 and other specific epithermal deposits (1:1.6 for Fruta Del Norte, Ecuador; 1:1.9 for Hishikari Gold Deposit, Japan; and 1:2.1 for Haile Gold Mine, South Carolina). However, the comparison ratio data are based on mining production statistics, rather than bulk exploration data. Some vein intersections at Big Easy have Au:Ag ratios that approach these global values from producing deposits, and the possibility of more extensive occurrence of the high Au type I veins, in particular, is of considerable interest for future exploration.

The integrated SEM-BSE-EDX, PCA, and numerical modelling analysis allows an improved understanding of the relationships between DDH core analyses and mineral assemblages observed

in the system. The negative correlation between Fe-Zn and Au-Ag bearing samples is explained by the pervasive presence of ambient, non-vein related, pyrite throughout the epiclastic host rocks. This alteration process took place before or during the induration of the epiclastic sediments, and before the veins were emplaced in fractures in the indurated rocks. The pyrite-silica alteration of the host sediments comprises a large volume envelope for vein mineralization and thus represents a useful tool for district-scale prospection and exploration. Strong correlations from PCA analysis, Pearson correlation values, numerical modeling, and drill hole correlation analysis are observed in Au-Ag and Mo-As. As and Mo in minor concentrations might be contained within pyrite in veins and pyritized selvages directly associated with Au-Ag mineralization. However, the halos of high Mo and As values that envelope the recognized Au and Ag mineralized veins are more likely a consequence of trace amounts of these elements in the disseminated host rock pyrite, and so represent an additional broader scale indicator for future exploration programs.

Graphic logs of drill core lithology and assay data show that gold mineralization is observed in a variety of quartz(±adularia)-veins that crosscut diverse host lithologies: silicified and chloritized conglomerates, colloform silica layers, and silicified sandstones.

Results obtained from these integrated analyses represent potentially useful tools for planning and executing more efficient exploration programs in the future. Low-sulfidation epithermal Au-Ag deposits are a significant source of these metals globally. Big Easy represents a prospective epithermal system within the Avalon Zone, and one of the important examples of this deposit type recognized in the district to date.

3.6 REFERENCES.

Adams, S. F. (1920). A microscopic study of vein quartz. Economic Geology, 15(8), 623–664. https://doi.org/10.2113/gsecongeo.15.8.623

Bakker, R. J. (2003). Package FLUIDS 1. Computer programs for analysis of fluid inclusion data and for modelling bulk fluid properties. Chemical Geology, 194(1–3), 3–23. https://doi.org/10.1016/S0009-2541(02)00268-1

Barton, M. D., Kieft, C., Burke, E. A. J., & Oen, I. S. (1978). Uytenbogaardtite, a new silver-gold sulfide. Canadian Mineralogist, 16, 651–657.

Berry, J. M., Mobley, R. M., Gillon, K. A., Yogodzinski, G. M., & Bates, C. C. (2016). A Neoproterozoic epithermal gold deposit - The Haile gold mine, South Carolina, USA. GSA Field Guides, 42(01), 1–8. https://doi.org/10.1130/2016.0042(01)

Brueckner, S. M., Piercey, S. J., Layne, G. D., Piercey, G., & Sylvester, P. J. (2015). Variations of sulphur isotope signatures in sulphides from the metamorphosed Ming Cu(−Au) volcanogenic massive sulphide deposit, Newfoundland Appalachians, Canada. Mineralium Deposita, 50(5), 619–640. https://doi.org/10.1007/s00126-014-0567-7

Buchanan, L. J. (1981). Precious metal deposits associated with volcanic environments in the Southwest. In W. R. Dickinson & W. D. Payne (Eds.), Relations of tectonics to ore deposits in the southern Cordillera: Arizona Geological Society Digest, v. 14 (p. 237–262).

Camprubí, A., & Albinson, T. (2007). Epithermal deposits in México - Update of current knowledge and an empirical reclassification. In Special Paper of the Geological Society of America (Vol. 422, Issue 14). https://doi.org/10.1130/2007.2422(14)

Canet, C., Franco, S. I., Prol-Ledesma, R. M., González-Partida, E., & Villanueva-Estrada, R. E. (2011). A model of boiling for fluid inclusion studies: Application to the Bolaños Ag-Au-Pb-Zn epithermal deposit, Western Mexico. Journal of Geochemical Exploration, 110(2), 118–125. https://doi.org/10.1016/j.gexplo.2011.04.005

Chizhova, I., & Volkov, A. V. (2014). Variations of Gold-silver Ratio in Ores of Epithermal Deposits: Comparative Analysis. 16th IAMG Meeting, June, 6p.

DeLazzer, A., & Dimmell, P. (2012). Report on 2011 Exploration (Diamond Drilling, Trench/DDH Reclamation, Compilation) on the Big Easy (BE) Property. Licences 13446M, 16633M, 17315M, 17342M, 19157M, NTS 2D/1,8. Thorburn Lake Area, Eastern Newfoundland for Silver Spruce Resources Inc., 181p.

Dimmell, P. (2012). Report on 2012 Exploration (Prospecting, Stream Sediment Geochemistry, Airborne Geophysics, Diamond Drilling, Compilation) on the Big Easy (BE) Property. Licences 13446M, 16633M, 17315M, 17342M, 19157M, NTS 2D/1, 8. Thorburn Lake Area, Eastern Newfoundland for Silver Spruce Resources Inc., 271p.

Dimmell, P. (2015). Report on 2014 Exploration (Prospecting, Soil Sediment Geochemistry, Diamond Drilling, Compilation) on the Big Easy (BE) Property, Licences 13446M, 16633M, 23023M, NTS 2D/1, 8, Thorburn Lake Area, Eastern Newfoundland for Silver Spruce Resources Inc., 154p.

Dong, G., Morrison, G., & Jaireth, S. (1995). Quartz textures in epithermal veins, Queensland - classification, origin, and implication. Economic Geology, 90(6), 1841–1856. https://doi.org/10.2113/gsecongeo.90.6.1841

Driesner, T., & Heinrich, C. A. (2007). The system H2O-NaCl. Part I: Correlation formulae for phase relations in temperature-pressure-composition space from 0 to 1000 °C, 0 to 5000

bar, and 0 to 1 XNaCl. Geochimica et Cosmochimica Acta, 71(20), 4880–4901. https://doi.org/10.1016/j.gca.2006.01.033

Etoh, J., Izawa, E., & Taguchi, S. (2002). A Fluid Inclusion Study on Columnar Adularia from the Hishikari Low-Sulfidation Epithermal Gold Deposit, Japan. Resource Geology, 52(1), 73–78.

Gabo-Ratio, J. A., Buena, A. E., Villaplaza, B. R. B., Payot, B. D., Dimalanta, C. B., Queaño, K. L., Andal, E. S., & Yumul, G. P. (2020). Epithermal mineralization of the Bonanza-Sandy vein system, Masara Gold District, Mindanao, Philippines. Journal of Asian Earth Sciences: X, 4(December), 1–13. https://doi.org/10.1016/j.jaesx.2020.100041

Ghezelbash, R., Maghsoudi, A., & Daviran, M. (2019). Prospectivity modeling of porphyry copper deposits: recognition of efficient mono- and multi-element geochemical signatures in the Varzaghan district, NW Iran. Acta Geochimica, 38(1), 131–144. https://doi.org/10.1007/s11631-018-0289-0

Gu, Y., (2003). Automated Scanning Electron Microscope Based Mineral Liberation Analysis: An Introduction to JKMRC/FEI Mineral Liberation Analyser, Journal of Minerals and Materials Characterization and Engineering, 2(1), 33–41. https://doi.org/10.4236/jmmce.2003.21003

Hedenquist, J., Arribas, A., & Gonzalez-Urien, E. (2000). Exploration for Epithermal Gold Deposits. Reviews in Economic Geology, 13(l), 245–277.

Ibaraki, K., & Suzuki, R. (1993). Gold-silver quartz-adularia veins of the Main, Yamada and Sanjin deposits, Hishikari gold mine: A comparative study of their geology and ore deposits. Resource Geology, 14, 1–11.

Izawa, E., & Urashima, Y. (1983). Hydrothermal alteration of drilling core of Hishikari gold deposits. Mining Geology, 33, 50.

Izawa, E., Urashima, Y., Ibaraki, K., Suzuki, R., Yokoyama, T., Kawasaki, K., Koga, A., & Taguchi, S. (1990). The Hishikari gold deposit: high-grade epithermal veins in Quaternary volcanics of southern Kyushu, Japan. Journal of Geochemical Exploration, 36(1–3), 1–56. https://doi.org/10.1016/0375-6742(90)90050-K

John, D. A., Vikre, P. G., du Bray, E. A., Blakely, R. J., Fey, D. L., Rockwell, B. W., Mauk, J. L., Anderson, E. D., & Graybeal, F. T. (2010). Descriptive Models for Epithermal Gold-Silver Deposits. In Mineral deposit models for resource assessment, 264p. https://pubs.usgs.gov/sir/2010/5070/q/sir20105070q.pdf

Kullerud, K., Kotková, J., Šrein, V., Drábek, M., & Škoda, R. (2018). Solid solutions in the system acanthite (Ag2S)–naumannite (Ag2Se) and the relationships between Ag-sulfoselenides and Se-bearing polybasite from the Kongsberg silver district, Norway, with implications for sulfur–selenium fractionation. Contributions to Mineralogy and Petrology, 173(9), 1–17. https://doi.org/10.1007/s00410-018-1500-3

Leary, S., Sillitoe, R. H., Lema, J., Téliz, F., & Mena, D. (2020). Geology of the Fruta del Norte Epithermal Gold-Silver Deposit, Ecuador. Society of Economic Geologists - SEG Special Publications, 23, 431–450. https://doi.org/10.5382/sp.23.21

Leary, S., Sillitoe, R. H., Stewart, P. W., Roa, K. J., & Nicolson, B. E. (2016). Discovery, geology, and origin of the Fruta del Norte epithermal gold-silver deposit, southeastern Ecuador. Economic Geology, 111(5), 1043–1072. https://doi.org/10.2113/econgeo.111.5.1043

Lynne, B. (2013). Siliceous sinter: An early exploration tool and direct link to a geothermal reservoir. Thirty-Eight Workshop on Geothermal Reservoir Engineering, SGP-TR-198, p. 1–6.

Lynne, B., Campbell, K. A., James, B. J., Browne, P. R. J., & Moore, J. (2007). Tracking crystallinity in siliceous hot-spring deposits. American Journal of Science, 307(3), 612–641. https://doi.org/10.2475/03.2007.03

Mango, H., Arehart, G., Oreskes, N., & Zantop, H. (2014). Origin of epithermal Ag-Au-Cu-Pb-Zn mineralization in Guanajuato, Mexico. Mineralium Deposita, 49(1), 119–143. https://doi.org/10.1007/s00126-013-0478-z

Mobley, R. M., Yogodzinski, G. M., Creaser, R. A., & Berry, J. M. (2014). Geologic history and timing of mineralization at the Haile gold mine, South Carolina. Economic Geology, 109(7), 1863–1881. https://doi.org/10.2113/econgeo.109.7.1863

Mukaiyama, H. (1950). On some gold-silver ores from the Sado Mine, Sado Island, Niigata Prefecture, Japan. Chemical Pharmaceutical Bulletin, 56(655), 181–187. https://www.jstage.jst.go.jp/article/bpb1993/17/11/17_11_1460/_pdf/-char/ja

Petruk, W., Owens, D. R., Stewart, J. M., & Murray, E. J. (1974). Observations on acanthite, aguilarite and naumannite. The Canadian Mineralogist: Journal of the Mineralogical Association of Canada, 12(6), 365–369.

Potter, R. W. (1977). Pressure correction for fluid inclusions homogenization temperatures based on the volumetric properties of the system NaCl - H2O. Journal of Research of the U.S. Geological Survey, 5(5), 603–607.

Prokof'ev, V. Y., Volkov, A. V., Sidorov, A. A., Savva, N. E., Kolova, E. E., Uyutnov, K. V., & Byankin, M. A. (2012). Geochemical peculiarities of ore-forming fluid of the Kupol Au-Ag

epithermal deposit (Northeastern Russia). Doklady Earth Sciences, 447(2), 1310–1313. https://doi.org/10.1134/s1028334x12120057

Ramboz, C., Pichavant, M., & Weisbrod, A. (1982). Fluid immiscibility in natural processes: Use and misuse of fluid inclusion data: II Interpretation of fluid inclusion data in terms of immiscibility. Chemical Geology, 37, 29–48.

Rankin, A. H. (2004). Fluid Inclusions. Encyclopedia of Geology, p. 253–260. https://doi.org/10.1016/B0-12-369396-9/00097-6

Robinson, R. W., & Norman, D. I. (1984). Mineralogy and fluid inclusion study of the southern Amethyst vein system, Creede mining district, Colorado. Economic Geology, 79(3), 439–447. https://doi.org/10.2113/gsecongeo.79.3.439

Saunders, J. A., Vikre, P. G., Unger, D. L., & Beasley, L. (2010). Colloidal and physical transport textures exhibited by electrum and naumannite in bonanza epithermal veins from western USA, and their significance. In Great Basin evolution and metallogeny : Geological Society of Nevada, 2010 Symposium (p. 8). https://doi.org/10.1521/bumc.2012.76.4.393

Shikazono, N. (1985). Gangue Minerals from Neogene Vein-Type Deposits in Japan and an Estimate of their CO2 Fugacity. Economic Geology, 80, 754–768.

Shikazono, N. (2003). Geochemical and Tectonic Evolution of Arc-Backarc Hydrothermal Systems: Implication for the Origin of Kuroko and Epithermal Vein-Type Mineralizations and the Global Geochemical Cycle. Developments in Geochemistry, 8, 463p.

Shikazono, N. & Shimizu, M. (1992). Associated metals in vein-type deposits in Japan; interpretation using the HSAB principle. The Canadian Mineralogist, 30(1), 137–143.

Shimizu, T. (2014). Reinterpretation of quartz textures in terms of hydrothermal fluid evolution at the Koryu Au-Ag deposit, Japan. Economic Geology, 109, 2051–2065.

Sillitoe, R. H. (2015). Epithermal paleosurfaces. Mineralium Deposita, 50(7), 767–793. https://doi.org/10.1007/s00126-015-0614-z

Simpson, M. P., Mauk, J. L., & Simmons, S. F. (2001). Hydrothermal alteration and hydrologic evolution of the golden cross epithermal Au-Ag deposit, New Zealand. Economic Geology, 96(4), 773–796. https://doi.org/10.2113/gsecongeo.96.4.773

Slagter, S., Reich, M., Munoz-Saez, C., Southon, J., Morata, D., Barra, F., Gong, J., & Skok, J. R. (2019). Environmental controls on silica sinter formation revealed by radiocarbon dating. Geology, 47(4), 330–334. https://doi.org/10.1130/G45859.1

Sterner, S. M., & Bodnar, R. J. (1984). Synthetic fluid inclusions in natural quartz I. Compositional types synthesized and applications to experimental geochemistry. Geochimica et Cosmochimica Acta, 48(12), 2659–2668. https://doi.org/10.1016/0016-7037(84)90314-4

Tohma, Y., Imai, A., Sanematsu, K., Yonezu, K., Takahashi, R., Koyama, M., Sekine, R., Duncan, R., & Watanabe, K. (2010). Characteristics and mineralization age of the fukusen no. 1 vein, hishikari epithermal gold deposits, southern Kyushu, Japan. Resource Geology, 60(4), 348–358. https://doi.org/10.1111/j.1751-3928.2010.00140.x

Volkov, A. V., Prokof'ev, V. Y., Savva, N. E., Sidorov, A. A., Bayankin, M. A., Uyutnov, K. V., & Kolova, E. E. (2012). Ore formation at the Kupol epithermal gold-silver deposit in northeastern Russia deduced from fluid inclusion study. Geology of Ore Deposits, 54(4), 295–303. https://doi.org/10.1134/S107570151204006X

Walden, J., Smith, J. P., & Dackombe, R. V. (1992). The use of simultaneous R- and Q-mode factor analysis as a tool for assisting interpretation of mineral magnetic data. Mathematical Geology, 24(3), 227–247. https://doi.org/10.1007/BF00893748

Wallier, S., Rey, R., Kouzmanov, K., Pettke, T., Heinrich, C. A., Leary, S., O'Connor, G., Tămaş, C. G., Vennemann, T., & Ullrich, T. (2006). Magmatic fluids in the Breccia-hosted epithermal Au-Ag deposit of Roşia Montană, Romania. Economic Geology, 101(5), 923–954. https://doi.org/10.2113/gsecongeo.101.5.923

Wilkinson, J. J. (2001). Fluid Inclusions in Hydrothermal Ore Deposits. Lithos, 55, 229–272.

Zhou, D., Chang, T., & Davis, J. C. (1983). Dual extraction of R-mode and Q-mode factor solutions. Mathematical Geology, 15(5), 581–606. https://doi.org/10.1007/BF01093413

Figure 3.1 FEI MLA 650FEG Scanning Electron Microscope in the CREAIT Microanalysis Facility (MAF) at Memorial University. Photographed during use for this study. At the upper left is an SEM-BSE image of Sample BE14-18 85.2-4.

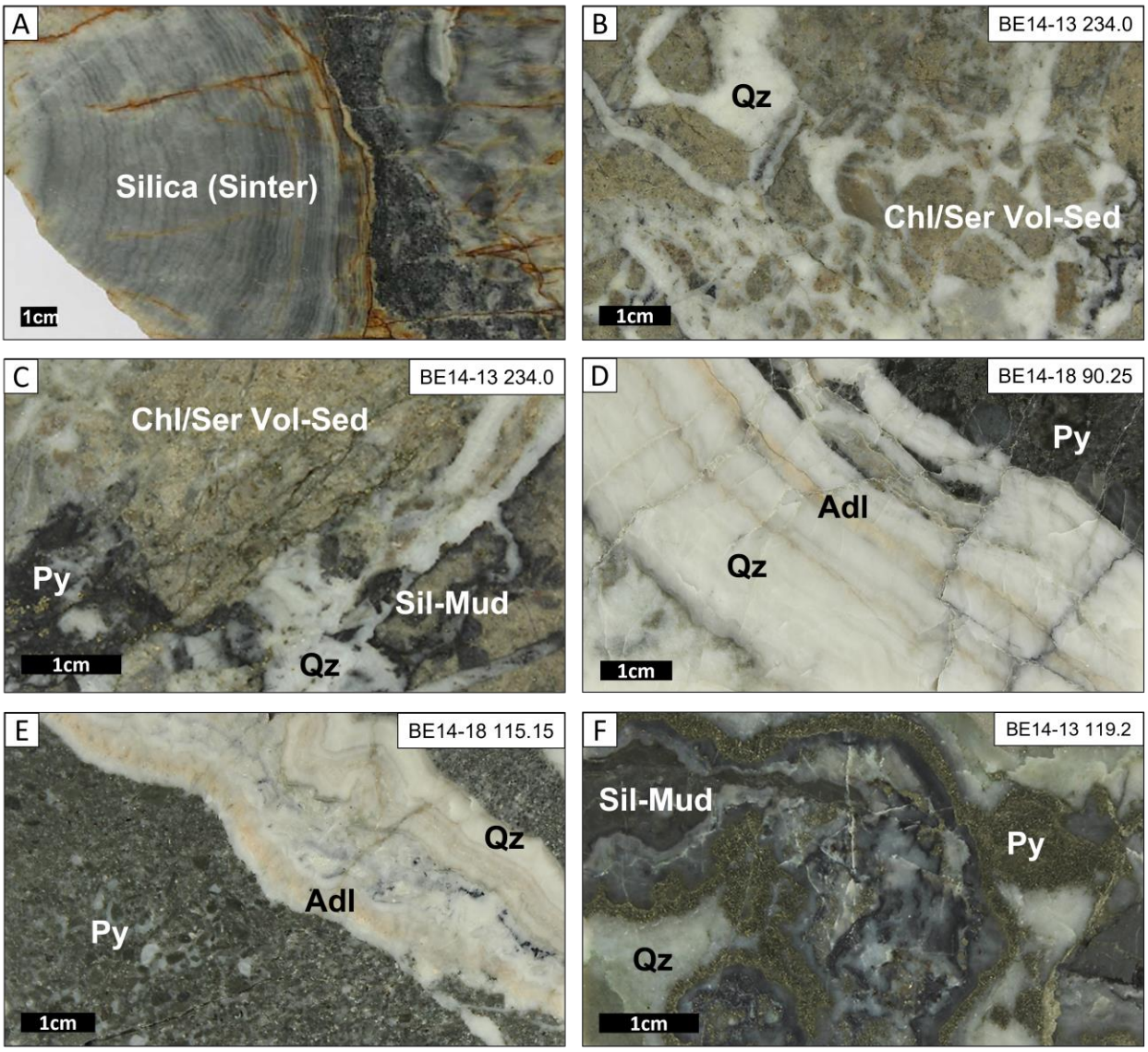

Figure 3.2 Common rock and vein textures in Big Easy: A) Hand sample of sinter material showing finely layered texture characteristic of cyclical deposition from near-surface hot spring activity. The original down-to-up direction is from left to right in the photograph. Dark gray material covering layered sinter is heavily silicified polymictic epiclastic sandstone-conglomerate. This is in turn covered by radiating silica on the right margin of the frame. B) Hydrothermal breccia with a matrix made up almost entirely of milky quartz. Angular fragments are comprised of chloritized/sericitized volcano-sedimentary host rock. The 1.4 m interval (233.9-235.3 m)

containing this sample (BE14-13 234.0) returned a value of 140 ppb Au and 13.6 ppm Ag; C) Hydrothermal breccia exhibiting two different types of host rocks in the breccia fragments: Chloritized/sericitized volcano-sedimentary rock (same colour as for frame B) and silicified mudstone (dark gray) containing disseminated pyrite. This sample corresponds to the same interval as the sample in B (BE14-13 234.0); D) Crustiform vein composed of successive alternating fine bands of quartz and adularia. Dark gray wallrock is a silicified pyritiferous coarse-grained sandstone. The 0.35 m interval (89.9-90.25 m) containing this sample (BE14-18 90.25) returned a value of 164 ppb Au and 11.5 ppm Ag; E) Crustiform vein exhibiting sinuous to crenulate bands of quartz, adularia, and small inclusions of wall rock in the quartz-adularia vein. Wallrock is a pyritiferous silicified sandstone-conglomerate composed of both rounded and subangular altered clasts. The 0.35 m interval (115.15-115.50 m) containing this sample (BE14-18 115.15) returned a value of 89 ppb Au and 12.1 ppm Ag; and F) Cockade texture characterized by massive pyrite and quartz precipitated in the form of encrustation surrounding fragments of silicified mudstone and silica. The 1.0 m interval (118.4-119.4 m) containing this sample (BE14-13 119.2) returned a value of 203 ppb Au, 23.3 ppm Ag, and >220 ppm Mo. Qz: Quartz, Adl: Adularia, Chl: Chlorite, Py: Pyrite, Ser: Sericite, Vol-Sed: Volcano-sedimentary rock, Sil-Mud: Silicified mudstone.

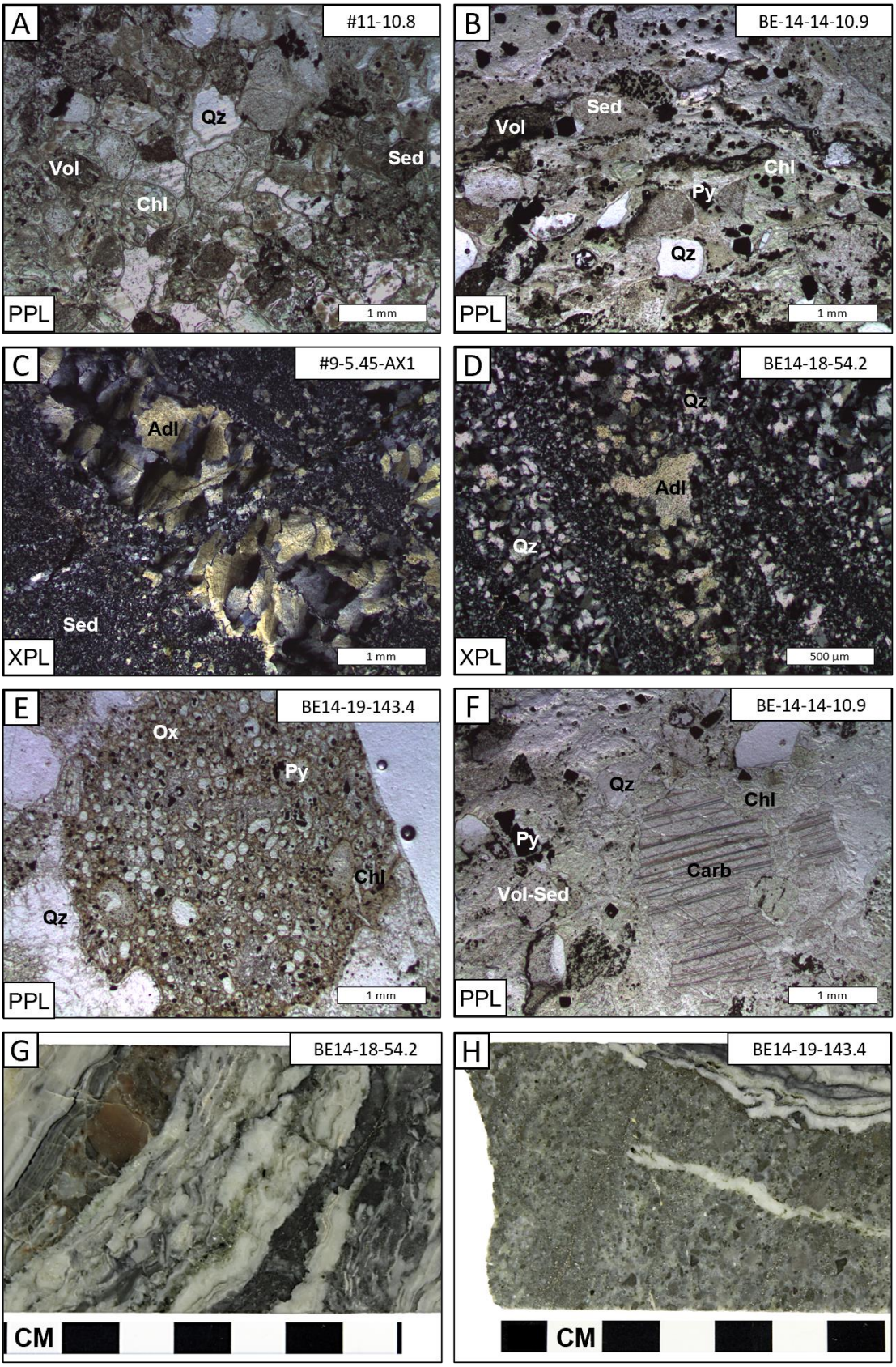
A
#11-10.8
Qz
Vol
Sed
Chl
PPL
1 mm
B
BE-14-14-10.9
Sed
Vol
Chl
Py
Qz
PPL
1 mm
C
#9-5.45-AX1
Adl
Sed
XPL
1 mm
D
BE14-18-54.2
Qz
Adl
Qz
XPL
500 µm
E
BE14-19-143.4
Ox
Py
Chl
Qz
PPL
1 mm
F
BE-14-14-10.9
Qz
Chl
Py
Carb
Vol-Sed
PPL
1 mm
G
BE14-18-54.2
CM
H
BE14-19-143.4
CM

Figure 3.3 Petrographic photomicrographs of Big Easy host rocks from Musgravetown Group from Figure 3.2. (PPL: Plane Polarized Light; XPL: Cross Polarized Light). A) Altered polymictic conglomerate composed of chloritized volcanic and sedimentary clasts; B) Chloritized conglomerate with disseminated subhedral pyrite crystals; C) Adularia as sub-rhombic and radiating crystals exhibiting low first-order interference colors, arranged in veins crosscutting a fine-grained sedimentary rock; D) Subparallel quartz-adularia veins traversing a mudstone host.; E) Chloritized/pyritized volcano-sedimentary fragment in host rock. This fragment also exhibits a dark brown halo-style "oxidization" alteration that does not seem directly related to gossanization of pyrite. The fragment is surrounded by relatively clear hydrothermal quartz; F) Hydrothermal breccia composed of chloritized volcanic rock fragments in a matrix of hydrothermal quartz, pyrite, and carbonate; G) Core sample from which photomicrograph D was obtained; and H) Core sample from which photomicrograph E was obtained. Qz: Quartz, Vol: Volcanic rock, Sed: Sedimentary rock, Chl: Chlorite, Py: Pyrite, Adl: Adularia, Ox: Oxidation, Carb: Carbonate.

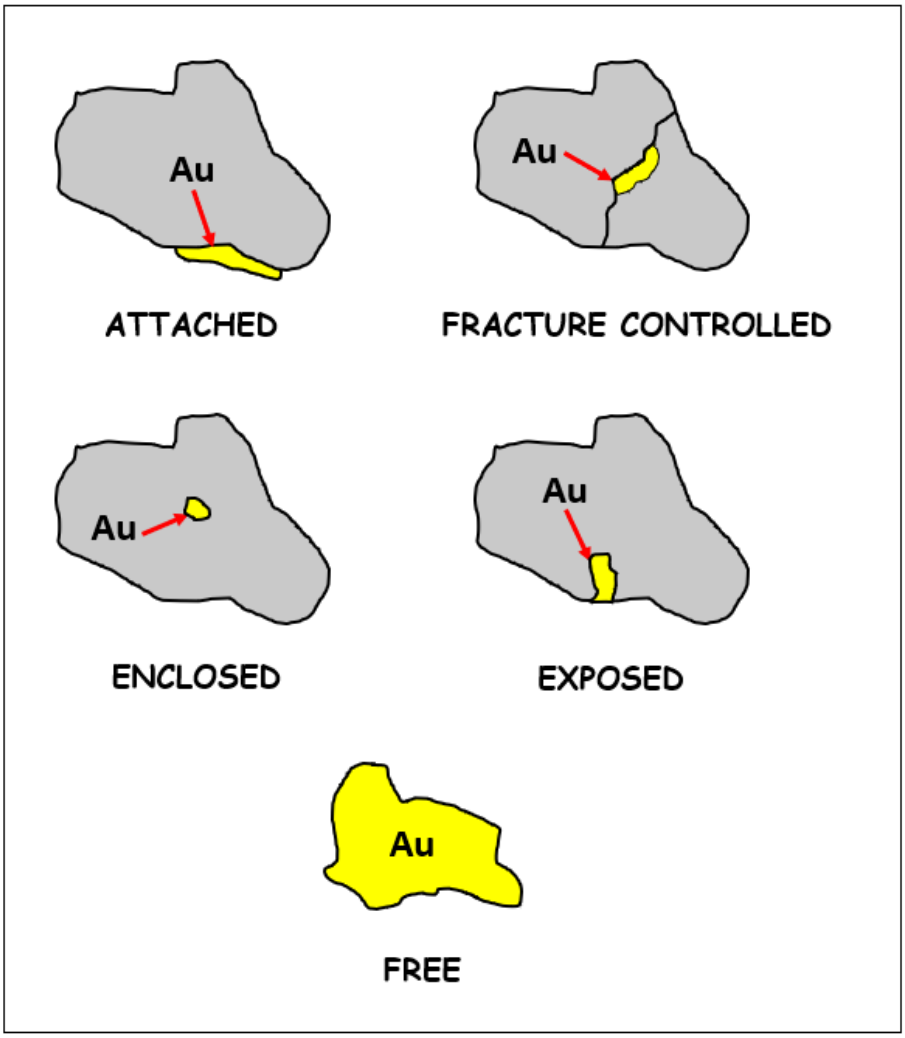

Figure 3.4 Schematic representation of spatial distribution categories for classifying gold-bearing (electrum) grains in the Big Easy Prospect.

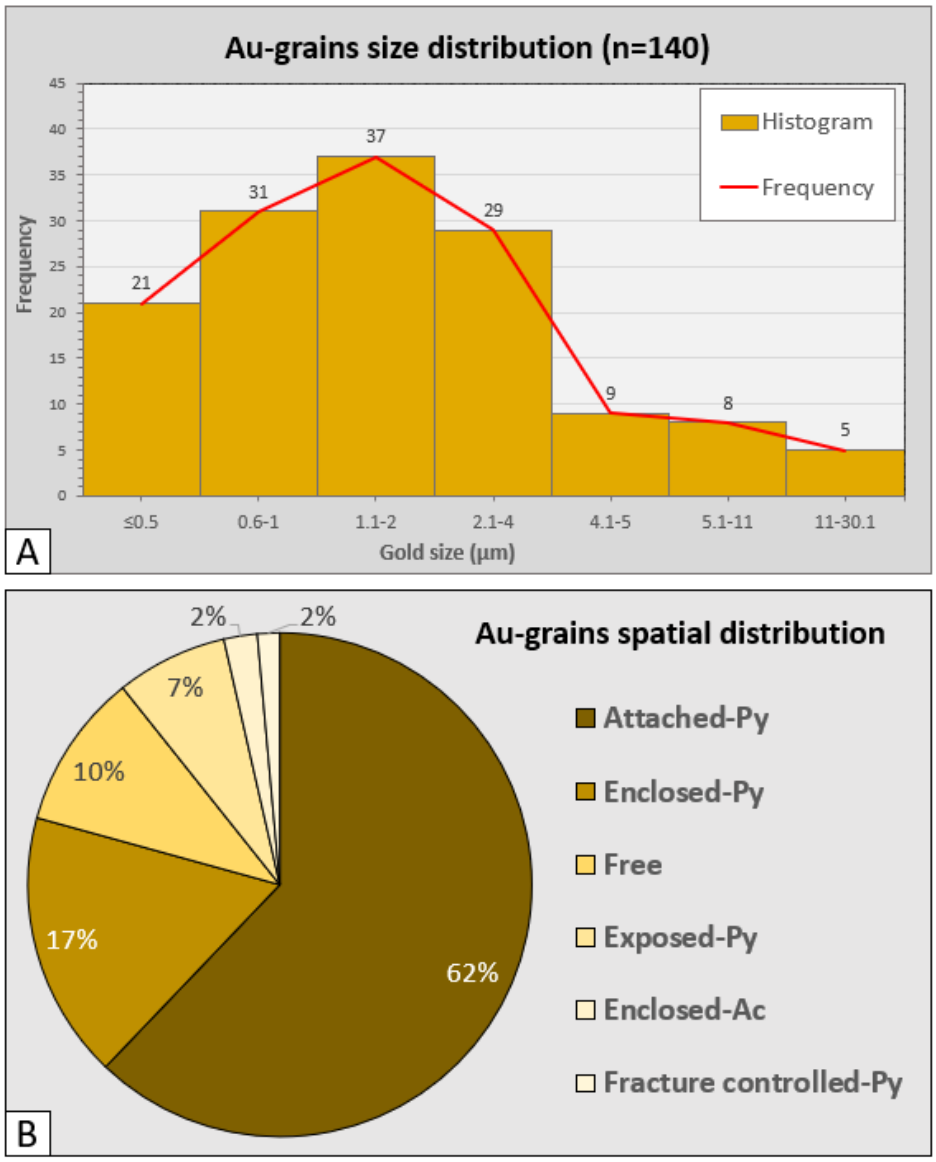

Figure 3.5 Gold-bearing grains distribution analysis of the Big Easy prospect. A) Grain size distribution, and B) Grain spatial distribution. Py: Pyrite, Ac: Acanthite.

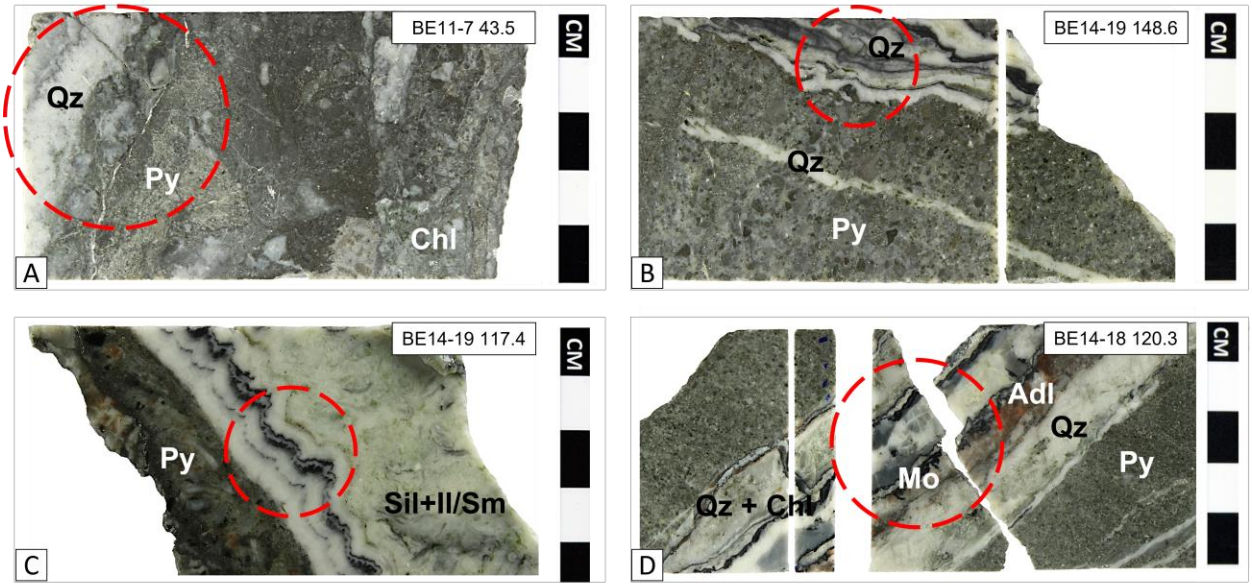

Figure 3.6 Polished core sections displaying characteristics of the four vein types identified at Big Easy: A) Type I: High Au (Electrum dominant). Sample shows pyritized, chloritized and silicified mudstone wallrock with some included subhedral quartz clasts. Vein type I is characterized by quartz and slightly crenulated pyrite bands. The 1.0 m interval (43.0-44.0 m) containing this sample (BE11-7 43.5) returned a value of 7645 ppb Au and 10 ppm Ag; B) Type II: High Au:Ag. Sample exhibits a coarser wallrock (between coarse sandstone and conglomerate/breccia) compared to type I example A, above. Vein type II is characterized by crustiform and somewhat sinuous bands of quartz with black bands containing silver minerals, such as native silver + acanthite + naumannite + aguilarite. The 0.2 m interval (148.6-148.8 m) containing this sample (BE14-19 148.6) returned a value of 6229 ppb Au and 98.7 ppm Ag; C) Type III: High Ag:Au (Ginguro). Sample shows characteristic distinctly crenulated Ginguro bands of black/dark grey silver minerals (native silver + acanthite ± aguilarite) as part of a thicker quartz-dominated vein. Pyrite is incipiently visible in the wallrock, but it is not visible in the quartz vein. The pale green alteration mineral visible in both vein and wallrock is interpreted as sericite/illite based on VIRS - TerraSpec^{TM} analysis (Clarke, 2013). The 0.14 m interval (117.4-117.54 m)

containing this sample (BE14-19 117.4) returned a value of 89 ppb Au and 7.9 ppm Ag; and D) Type IV: Molybdenite-rich. Sample displays a crustiform quartz vein with thinner banding composed of molybdenite and adularia. Wallrock is a pyritized fine-grained sedimentary rock, ranging from mudstone to fine sandstone. Dark green alteration mineral within vein is chlorite. The 0.2 m interval (120.3-120.5 m) containing this sample (BE14-18 120.3) returned a value of 1729 ppb Au, 34.3 ppm Ag and >220 ppm Mo. Qz: Quartz, Py: Pyrite, Chl: Chlorite, Sil: Silica, Ill: Illite, Sm: Smectite, Mo: Molybdenite, Adl: Adularia. Red circles indicate the zone of the core sample where veins were observed and described.

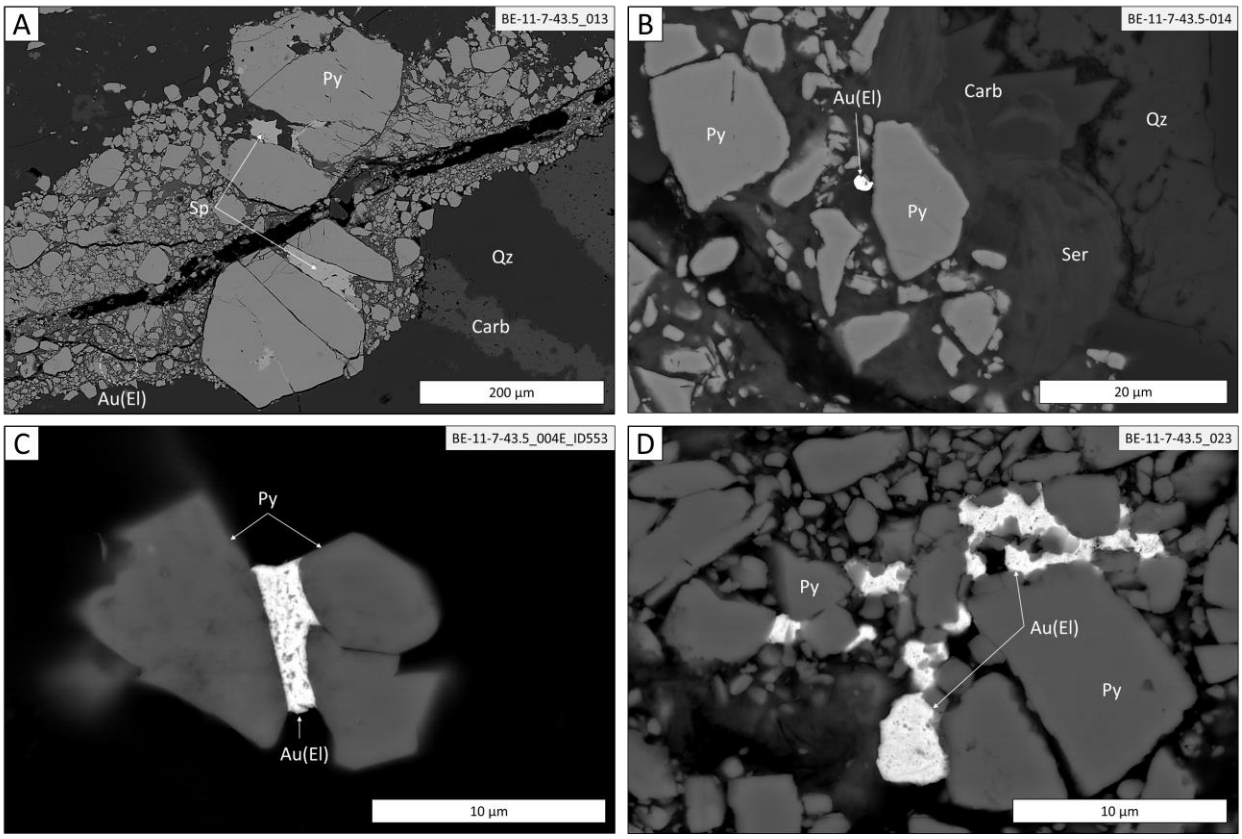

Figure 3.7 SEM-BSE images of Type I) High Au (Electrum dominant) sample (BE11-7 43.5; Figure 3.6A). A) Lower magnification view of vein texture dominated by euhedral to subhedral pyrite crystals with fracture-filling sphalerite and very fine isolated electrum grains. Gangue mineralogy is dominated by subparallel bands of quartz and carbonate; B) Close-up of subhedral pyrite crystals along the pyrite-rich portion of the vein. Electrum-free pyrite crystals are found within quartz, carbonate, and sericite matrix. A single isolated electrum grain is visible near the centre of the image; C) A porous anhedral intergranular electrum grain attached to pyrite; and D) Interstitial/overgrowth electrum associated with clustered pyrite crystals. The 1.0 m interval (43.0-44.0 m) containing this sample returned a value of 7645 ppb Au and 10 ppm Ag. Au(El): Electrum, Py: Pyrite, Sp: Sphalerite, Qz: Quartz, Carb: Carbonate, Ser: Sericite.

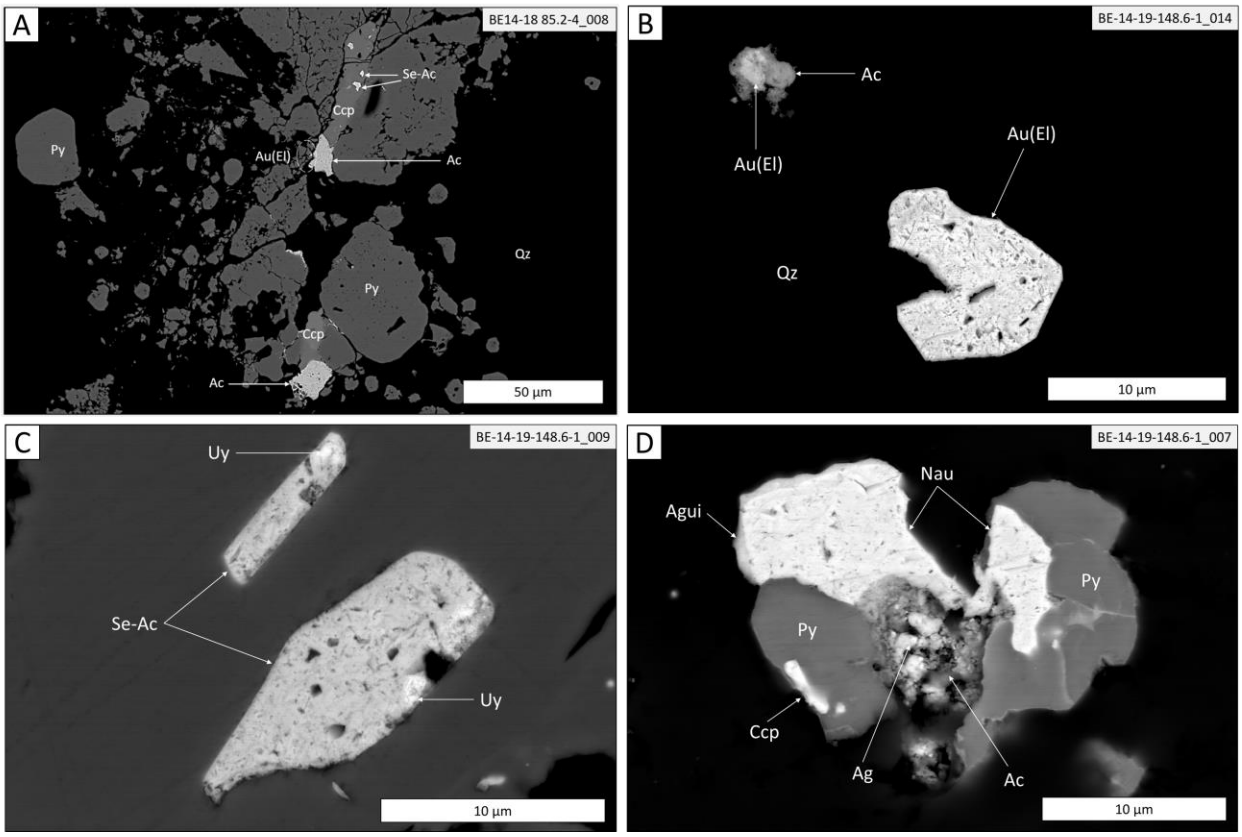

Figure 3.8 SEM-BSE images of Type II) High Au:Ag veins. A) General view of vein style mainly dominated by spongy anhedral pyrite crystals in a matrix of quartz. Chalcopyrite is intragranular to, or transects, pyrite, and is associated with acanthite. Chalcopyrite also contains small inclusions of seleniferous acanthite (Se-acanthite). The 0.5 m interval (84.8-85.3 m) containing this sample (BE14-18 85.2) returned a value of 421 ppb Au and 70.6 ppm Ag; B) Sample BE14-19 148.6. Electrum is mainly deported as isolated porous crystals, or intergrown with acanthite, within a quartz matrix; C) Porous Se-acanthite crystals included within pyrite. Rare uytenbogaardtite occurs here as inclusions (apparent vug fillings) within the Se-acanthite; D) Complex assemblages of Ag-S-Se minerals comprise irregular grains of aguilarite, naumannite, native silver, and acanthite. These surround and replace pyrite with inclusions of minor chalcopyrite. The 0.2 m interval (148.6-148.8 m) containing sample BE14-19 148.6 returned a

value of 6229 ppb Au and 98.7 ppm Ag. Au(El): Electrum, Ag: Native Silver, Ac: Acanthite, Se-Ac: Seleniferous Acanthite, Uy: Uytenbogaardtite, Agui: Aguilarite, Nau: Naumannite, Py: Pyrite, Ccp: Chalcopyrite, Qz: Quartz.

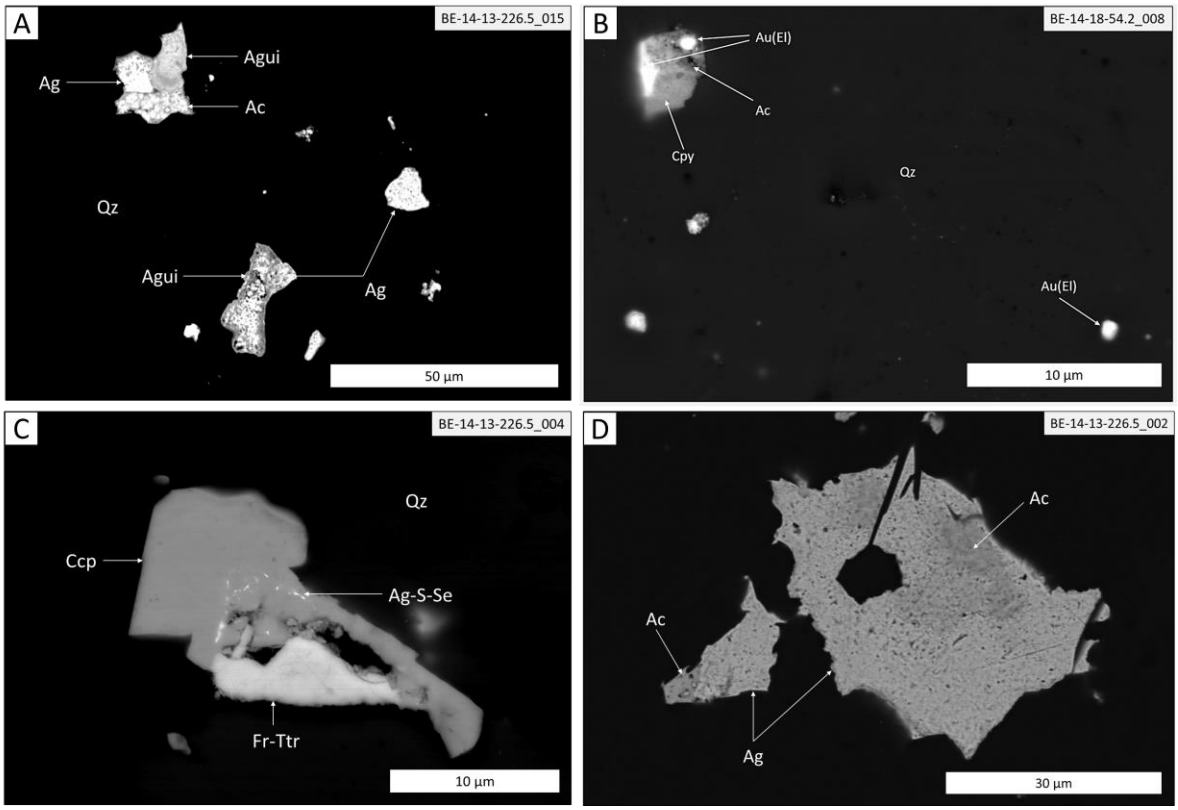

Figure 3.9 SEM-BSE images of Type III) High Ag:Au (Ginguro) veins. A) Isolated anhedral crystals of Ag-bearing minerals including aguilarite, acanthite, and native silver commonly occur within a quartz matrix (BE14-13 226.5); B) Minor electrum grains are dispersed in quartz matrix as isolated grains or in small clusters with acanthite and chalcopyrite (BE14-18 54.2); C) Subhedral chalcopyrite and an intermediate member of the freibergite–tetrahedrite series. Submicron grains of one or more Ag-S-Se minerals form an array included within the chalcopyrite crystals (BE14-13 226.5); and D) Anhedral native silver and acanthite comprise the most abundant components of the Type III Ginguro vein ore mineral assemblage (BE14-13 226.5). The 0.2 m interval (226.5-226.7 m) containing sample (BE14-13 226.5) returned a value of 9967 ppb Au and 1094 ppm Ag (A, C, and D); the 0.3 m interval (53.9-54.2 m) containing sample (BE14-18 54.2) returned a value of 3855 ppb Au and 119.6 ppm Ag (B). Ag: Native Silver, Ac: Acanthite, Agui: Aguilarite, Fr-Ttr: Freibergite–Tetrahedrite, Chalcopyrite, Ccp: Chalcopyrite, Qz: Quartz.

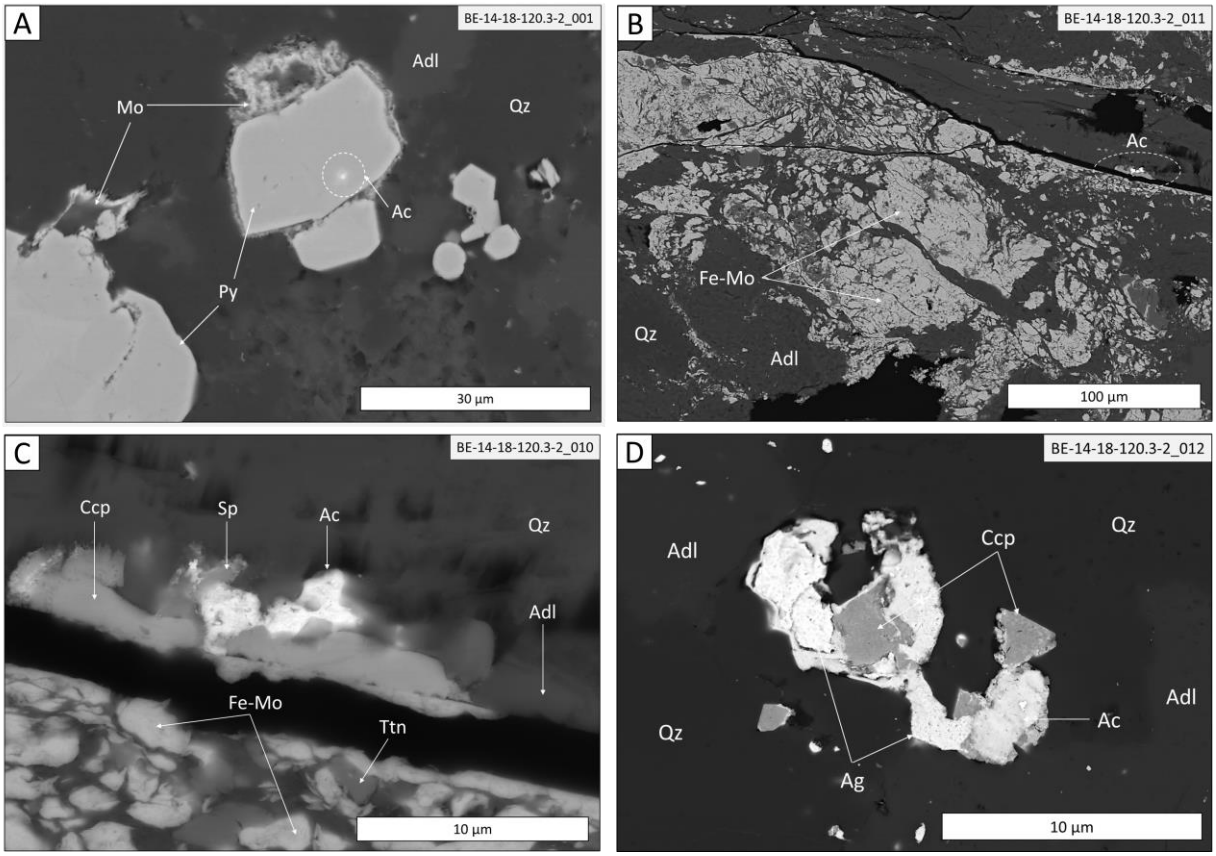

Figure 3.10 SEM images of Type IV) Molybdenite-rich vein (BE14-18 120.3; Figure 3.6D). A) Molybdenite exhibiting a feathery overgrowth texture around subhedral pyrite crystals. Very fine-grained acanthite occurs as an inclusion in pyrite. Gangue mineralogy is dominated by intergrowths of quartz and adularia; B) Clusters of irregular ferroan molybdenite (Fe-molybdenite) laths are the predominant texture for molybdenite in vein-type IV. Other minor ore minerals, including acanthite, are visible within the dotted oval; C) Close up of the area within the dotted oval of B), showing an assemblage of chalcopyrite, sphalerite, and acanthite. Minor titanite is associated with the Fe-molybdenite; and D) Mineral assemblage peripheral to the main molybdenite vein. Euhedral chalcopyrite crystals are surrounded and partially replaced by acanthite and native silver. The 0.2 m interval (120.3-120.5 m) containing this sample returned a value of 1729 ppb Au, 34.3 ppm Ag, and 7220 ppm Mo. Mo: Molybdenite, Fe-Mo: Fe-rich

Molybdenite, Ac: Acanthite, Ag: Native Silver, Py: Pyrite, Ccp: Chalcopyrite, Sp: Sphalerite, Adl: Adularia, Qz: Quartz, Ttn: Titanite.

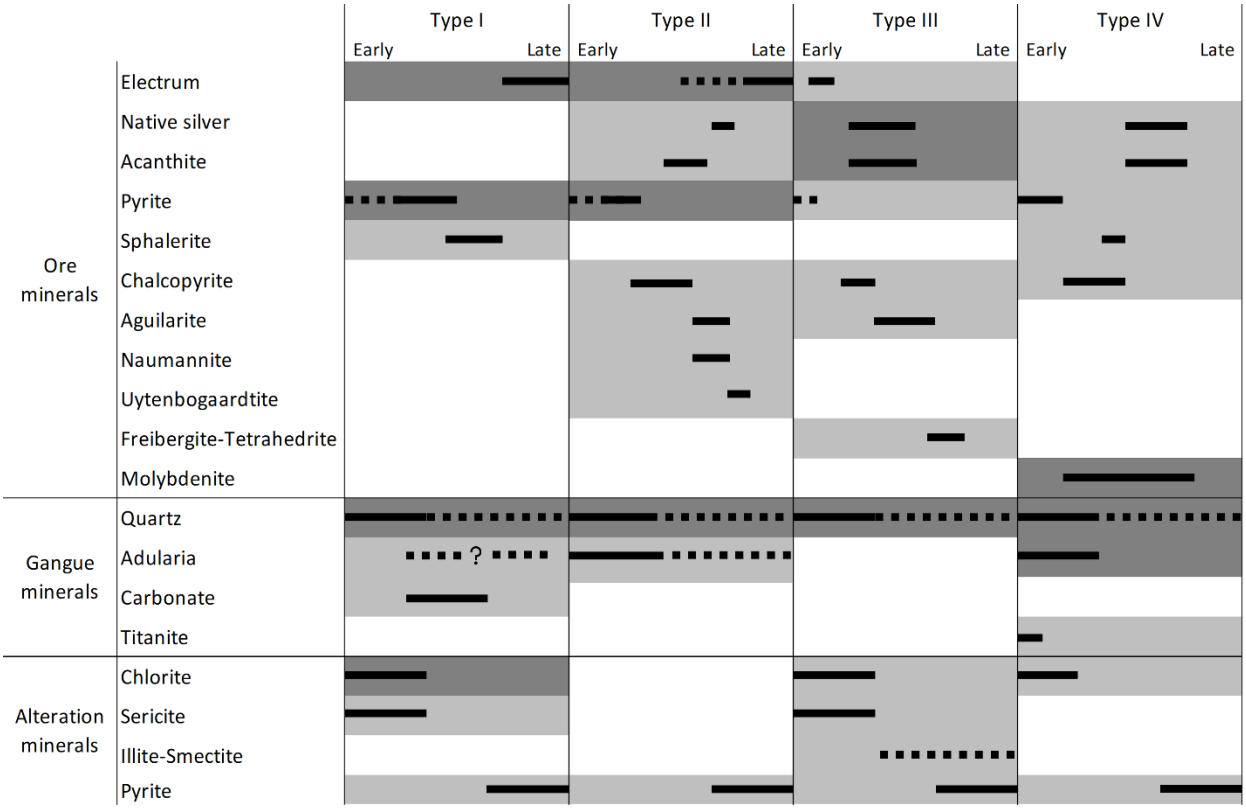

Figure 3.11 Paragenetic sequence exhibiting mineralogical variations between vein types. Minerals were divided into ore, gangue (non-ore vein minerals), and alteration minerals. Dominant minerals are displayed in dark grey and minor/secondary minerals in light grey.

Correlation	Ag-CLR	Au-CLR	As-CLR	Cu-CLR	Fe-CLR	Mo-CLR	Pb-CLR	Sb-CLR	Se-CLR	Zn-CLR
Ag-CLR	1	0.68	0.50	0.09	-0.37	0.42	0.03	0.09	-0.07	-0.27
Au-CLR	0.68	1	0.55	0.09	-0.33	0.35	-0.05	0.05	-0.04	-0.29
As-CLR	0.50	0.55	1	0.07	-0.17	0.49	0.04	-0.03	-0.16	-0.17
Cu-CLR	0.09	0.09	0.07	1	0.21	0.13	0.09	-0.18	-0.10	0.10
Fe-CLR	-0.37	-0.33	-0.17	0.21	1	-0.15	-0.01	-0.12	-0.12	0.54
Mo-CLR	0.42	0.35	0.49	0.13	-0.15	1	0.12	-0.22	-0.17	-0.10
Pb-CLR	0.03	-0.05	0.04	0.09	-0.01	0.12	1	-0.08	0.15	0.15
Sb-CLR	0.09	0.05	-0.03	-0.18	-0.12	-0.22	-0.08	1	0.10	-0.21
Se-CLR	-0.07	-0.04	-0.16	-0.10	-0.12	-0.17	0.15	0.10	1	-0.18
Zn-CLR	-0.27	-0.29	-0.17	0.10	0.54	-0.10	0.15	-0.21	-0.18	1

Figure 3.12 Pearson Correlation table generated with Principal Component Analysis (PCA) shows a strong positive correlation between Au and Ag (0.68), but a strong negative correlation between Fe and both Au (-0.33) and Ag (-0.37). Other significant correlations (> ±0.25) include positive correlations for As-Au (0.55), As-Ag (0.50), As-Mo (0.49), Mo-Ag (0.42), Mo-Au (0.35), and Fe-Zn (0.54), and negative correlations for Ag-Zn (-0.27), and Au-Zn (-0.29).

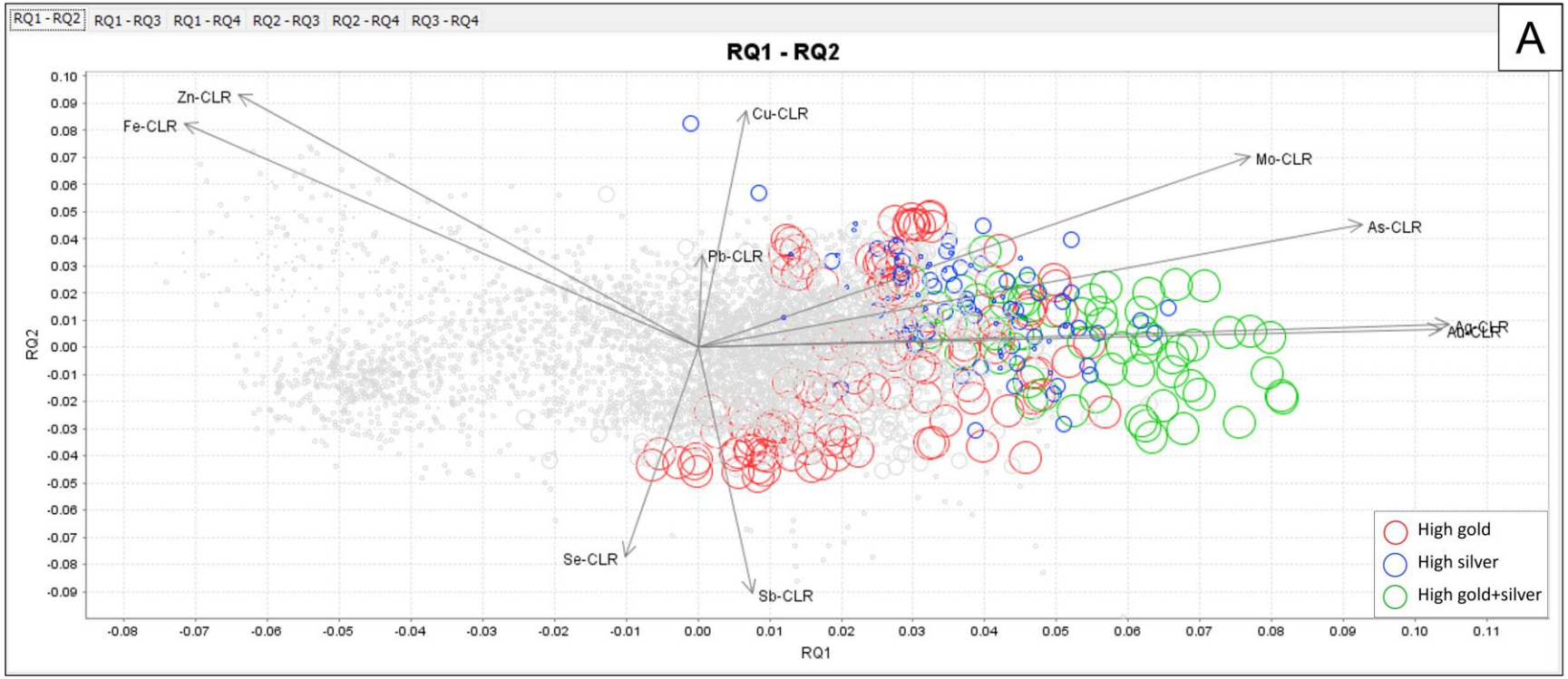
RQ1 - RQ2
RQ1 - RQ3
RQ1 - RQ4
RQ2 - RQ3
RQ2 - RQ4
RQ3 - RQ4
A
RQ1 - RQ2
Zn-CLR
Fe-CLR
Cu-CLR
Mo-CLR
As-CLR
Pb-CLR
Ag-CLR
Au-CLR
Se-CLR
Sb-CLR
High gold
High silver
High gold+silver
RQ1
RQ2

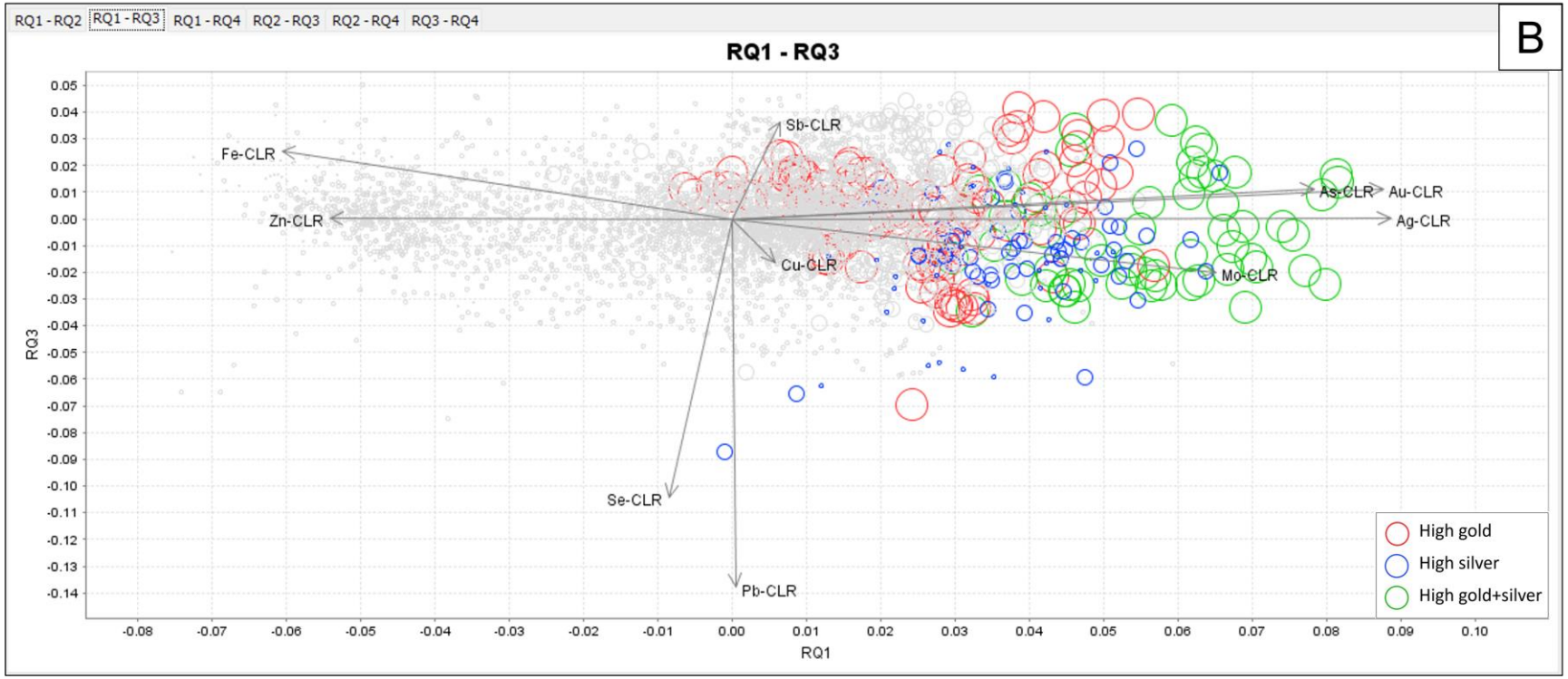
RQ1 - RQ2
RQ1 - RQ3
RQ1 - RQ4
RQ2 - RQ3
RQ2 - RQ4
RQ3 - RQ4
B
RQ1 - RQ3
Sb-CLR
Fe-CLR
Zn-CLR
As-CLR
Au-CLR
Ag-CLR
Cu-CLR
Mo-CLR
Se-CLR
Pb-CLR
High gold
High silver
High gold+silver
RQ3
RQ1

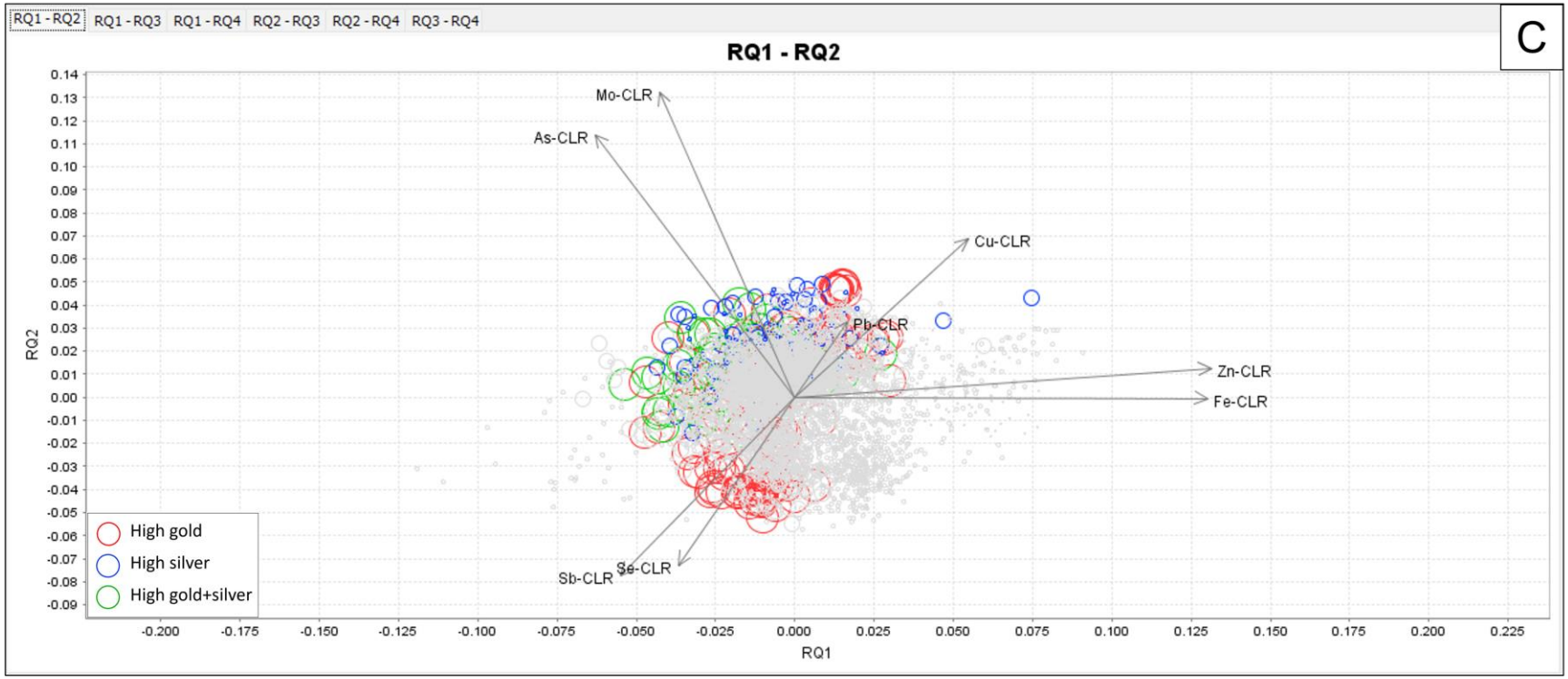
RQ1 - RQ2
RQ1 - RQ3
RQ1 - RQ4
RQ2 - RQ3
RQ2 - RQ4
RQ3 - RQ4
C
RQ1 - RQ2
Mo-CLR
As-CLR
Cu-CLR
Pb-CLR
Zn-CLR
Fe-CLR
Se-CLR
Sb-CLR
High gold
High silver
High gold+silver
RQ2
RQ1

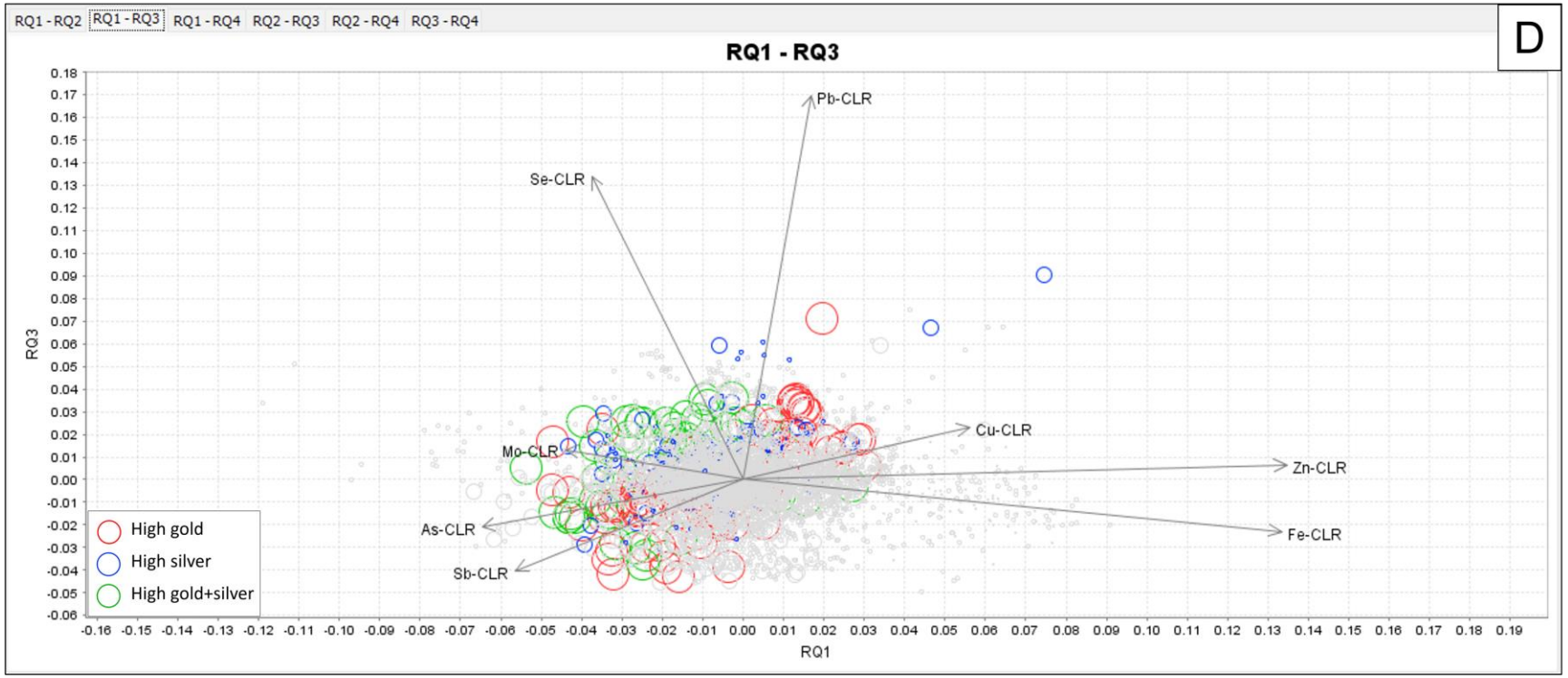

Figure 3.13 Principal Component Analysis (PCA) of Big Easy core sample assays (n=4249). Symbols are coded by *colour* for the following characteristics: High gold (red) = Au > 0.4 ppm; and High silver (blue) = Ag > 10 ppm; High gold + silver (green) have both these characteristics. Symbols are coded by *diameter* for Au concentration ranges: Small bubbles (<100 ppb), medium bubbles (100-400 ppb), and large bubbles (>400 ppb).

A) and B). PCA for element set Au, Ag, As, Cu, Fe, Mo, Pb, Sb, Se, and Zn. Cumulative variances for principal components (RQ): 46.4% for RQ1+RQ2 and 58.1% for RQ1+RQ2+RQ3 (see Figure 3.13A). In both RQ2 vs RQ1 and RQ3 vs RQ1 plots, samples with higher Au (and/or Ag) values are, as expected, dispersed along clustered Au-Ag vectors, and lie almost exclusively in the positive RQ1 portion of the plots. However, there are some informative additional features apparent. There are pronounced Mo and As vectors subparallel to the closely paired Au and Ag vectors in both plots. Samples with values below the legend thresholds for Au and Ag (0.4 ppm and 10 ppm, respectively) are dispersed in an opposite direction, along the Fe-Zn vector cluster into negative RQ1 space. In the RQ2 vs RQ1 plot, a population of high Au samples is dispersed toward an Sb(-Se) vector cluster.

C) and D). PCA for element set As, Cu, Fe, Mo, Pb, Sb, Se, and Zn (excluding Au and Ag). Cumulative variances for principal components (RQ): 44.7% for RQ1+RQ2 and 59.2% for RQ1+RQ2+RQ3 (see Figure 3.13B). Without the direct influence of Au and Ag as variables, similar features are still apparent. In the RQ2 vs RQ1 plot, a subpopulation of samples with higher Au are dispersed toward an Sb(-Se) cluster (similarly to the behavior observed in A). Samples with higher Ag are dispersed in a direction subparallel to the Mo-As vector cluster. In the RQ3 vs RQ1 plot, the behavior and relationship between variables and samples are not as clear. In both RQ2 vs RQ1 and RQ3 and RQ1 plots, samples below the legend thresholds for Au and Ag are, once again, dispersed toward the Fe-Zn vector cluster.

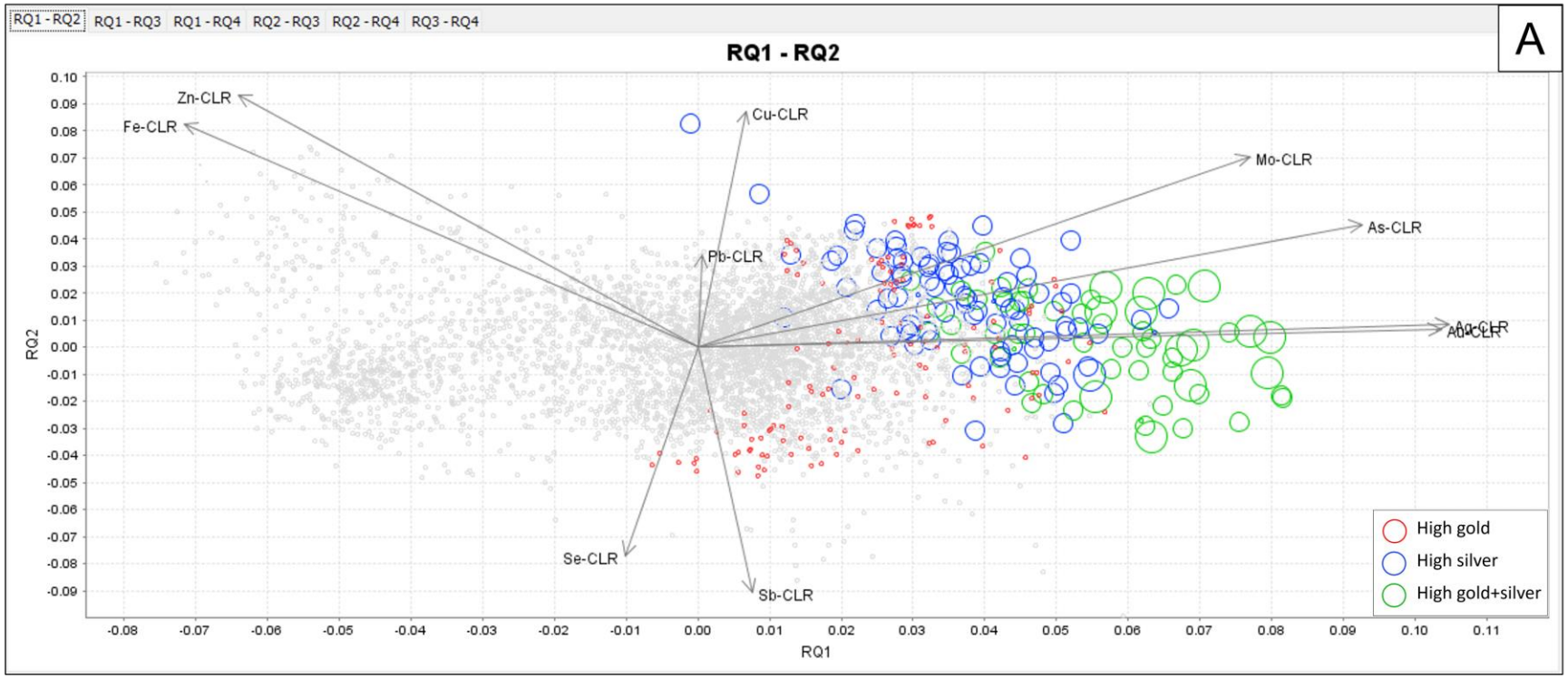
RQ1 - RQ2
RQ1 - RQ3
RQ1 - RQ4
RQ2 - RQ3
RQ2 - RQ4
RQ3 - RQ4
A
RQ1 - RQ2
Zn-CLR
Fe-CLR
Cu-CLR
Mo-CLR
As-CLR
Pb-CLR
Ag-CLR
Au-CLR
Se-CLR
Sb-CLR
High gold
High silver
High gold+silver
RQ1
RQ2

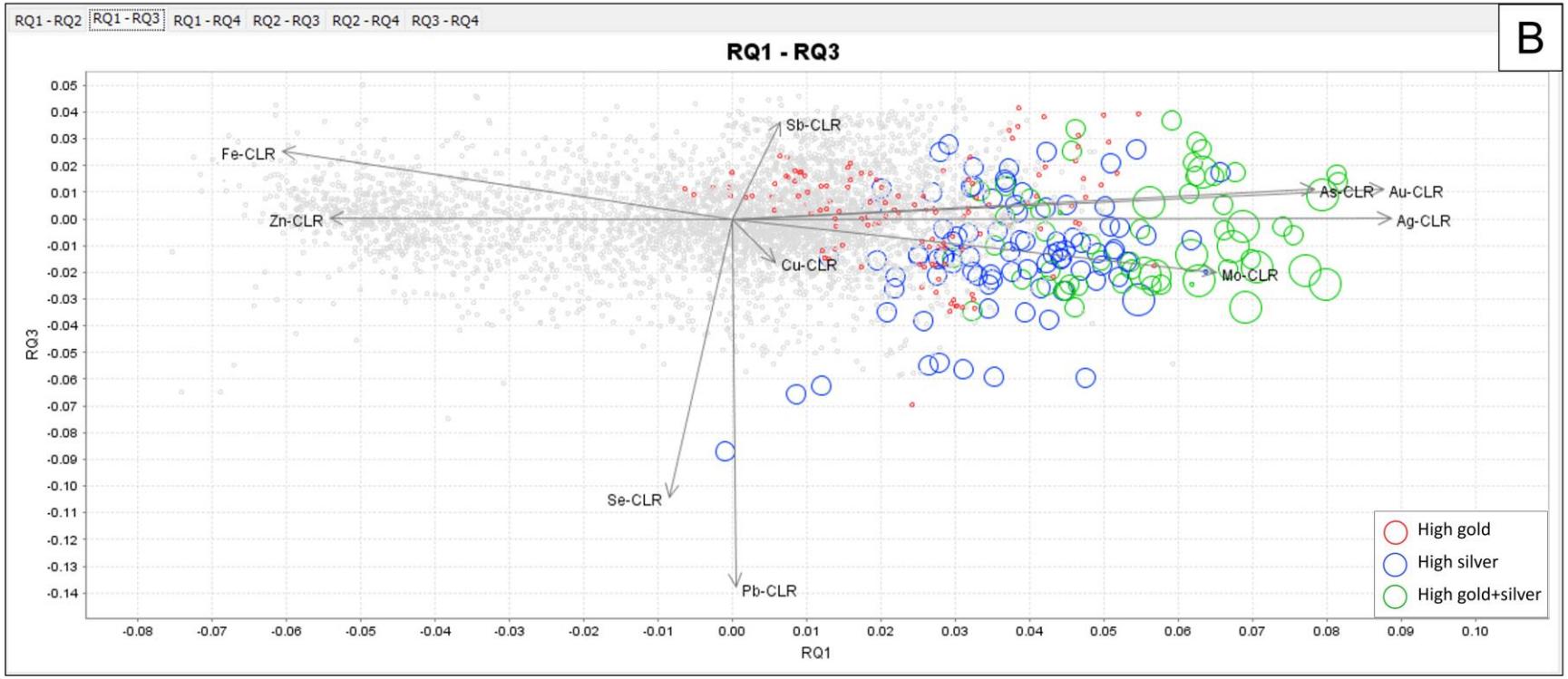
RQ1 - RQ2
RQ1 - RQ3
RQ1 - RQ4
RQ2 - RQ3
RQ2 - RQ4
RQ3 - RQ4
B
RQ1 - RQ3
Sb-CLR
Fe-CLR
Zn-CLR
As-CLR
Au-CLR
Ag-CLR
Cu-CLR
Mo-CLR
Se-CLR
Pb-CLR
High gold
High silver
High gold+silver
RQ3
RQ1

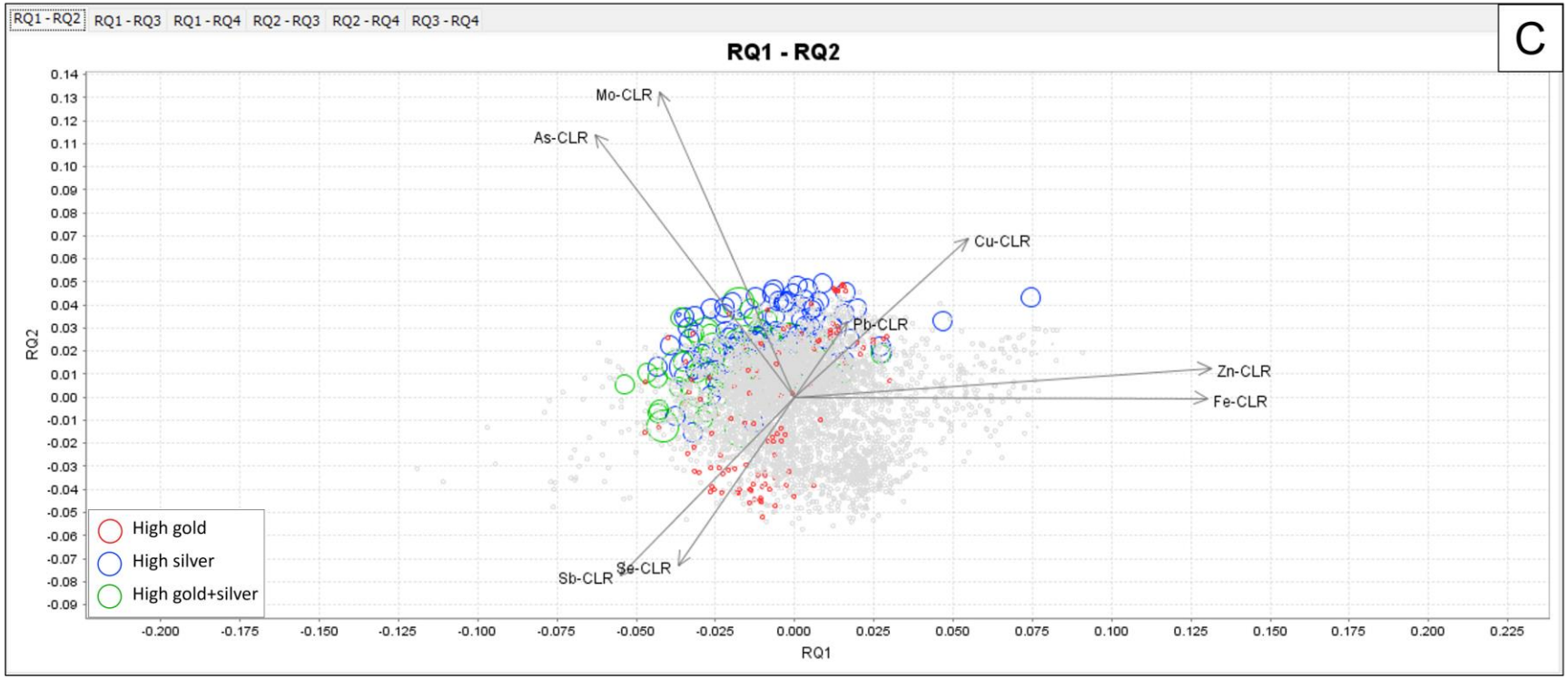
RQ1 - RQ2
RQ1 - RQ3
RQ1 - RQ4
RQ2 - RQ3
RQ2 - RQ4
RQ3 - RQ4
C
RQ1 - RQ2
Mo-CLR
As-CLR
Cu-CLR
Pb-CLR
Zn-CLR
Fe-CLR
Se-CLR
Sb-CLR
High gold
High silver
High gold+silver
RQ2
RQ1

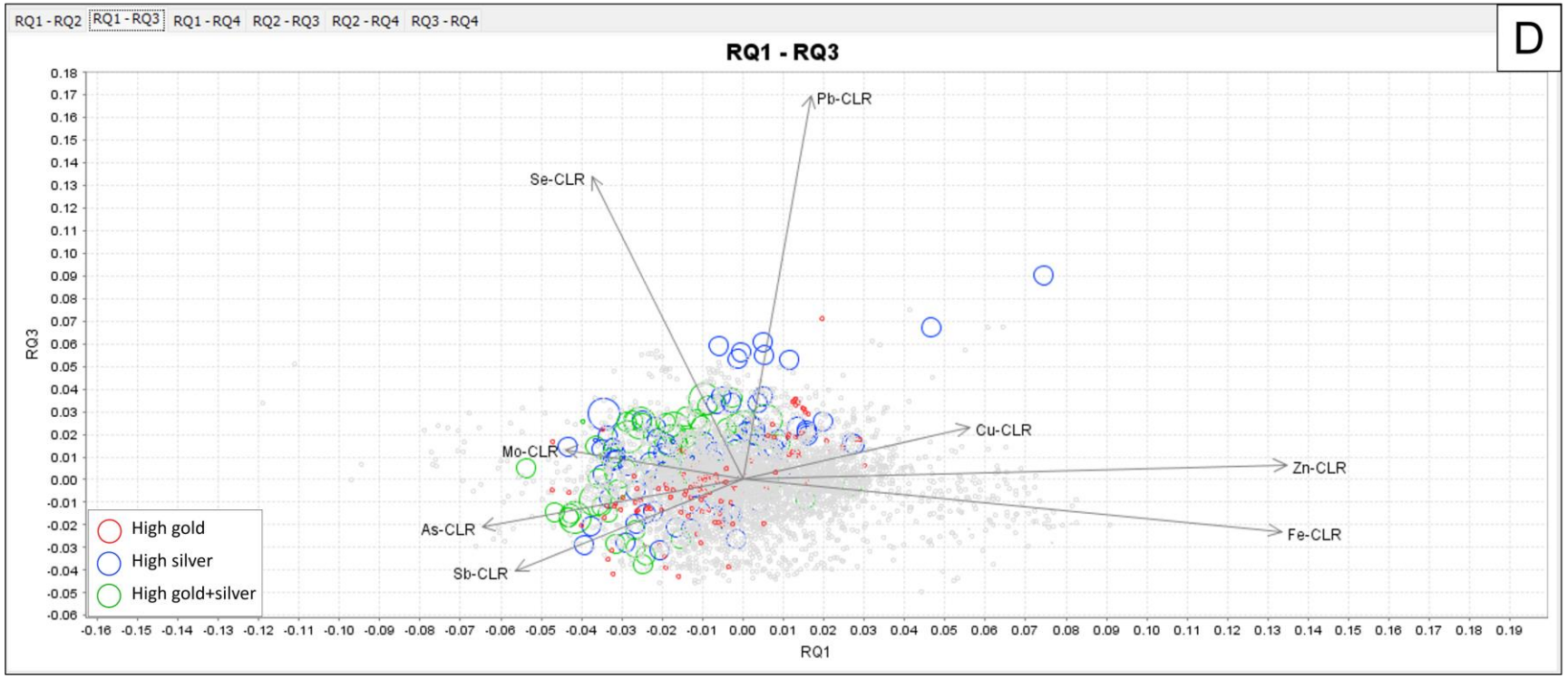

Figure 3.14 Principal Component Analysis (PCA) of Big Easy core sample assays (n=4249). The analysis is identical to that shown in Figure 3.13. Symbols are coded by *colour* as for Figure 3.13. Symbols are coded by *diameter* for Ag rather than Au concentration ranges: Small bubbles (<10 ppm), medium bubbles (10-100 ppm), and large bubbles (>100 ppm).

A) and B). PCA for element set Au, Ag, As, Cu, Fe, Mo, Pb, Sb, Se, and Zn. In both RQ2 vs RQ1 and RQ3 vs RQ1 plots, there is some apparent dispersal of higher Ag samples along Mo and As vectors. Samples below legend threshold values (0.4 ppm and 10 ppm,

respectively) are dispersed in an opposite direction toward Fe and Zn vectors. Additionally, in both RQ2 vs RQ1 and RQ3 vs RQ1 plots, Cu, Pb, Se, and Pb vectors do not exhibit a relationship (neither positive nor negative) with samples of high Ag values.

C) and D). PCA for element set As, Cu, Fe, Mo, Pb, Sb, Se, and Zn (excluding Au and Ag). Without the direct influence of Au and Ag as variables, some useful details are more apparent. In the RQ2 vs RQ1 plot of C) there is a dispersal of higher Ag samples along the Mo (±As) vector. In the RQ3 versus RQ1 plot of D) there is a small subpopulation of higher Ag samples dispersed along the Pb vector. Both plots show a small set of higher Ag outliers dispersed along the Cu vector.

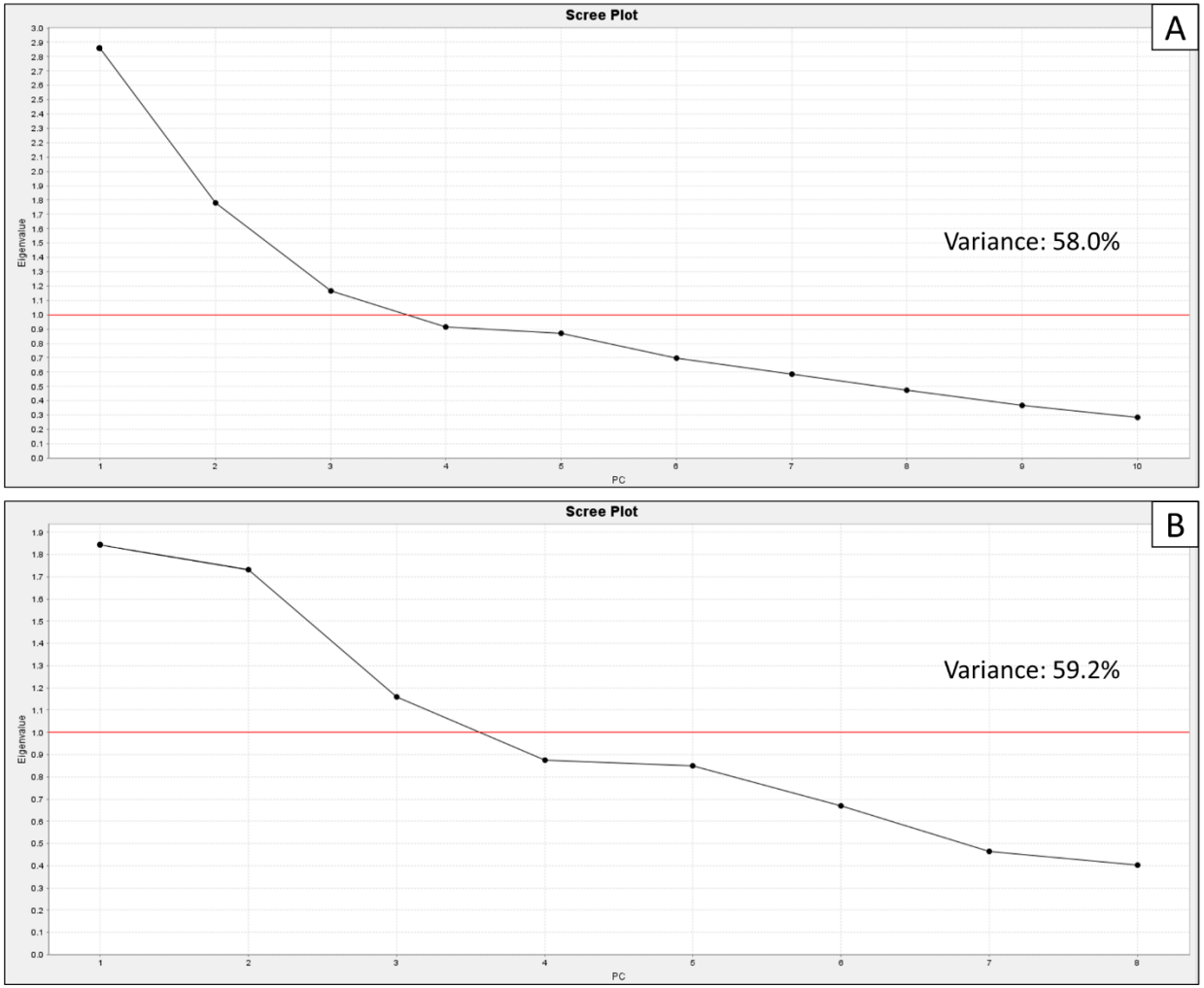

Figure 3.15 Scree plots for PCA analyses (Figures 3.13 and 3.14). A) Scree plot showing the dimensionality reduction for the PCA of Figures 3.13A-B and 3.14A-B (element set Au, Ag, As, Cu, Fe, Mo, Pb, Sb, Se, and Zn). Overall data can be explained sufficiently

using the first three Principal Components (PC), which define a cumulative overall variance of 58.0%, and are the only ones with eigenvalues that exceed 1.00. B) Scree plot showing the dimensionality reduction for the PCA of Figures 3.13C-D and 3.14C-D (element set As, Cu, Fe, Mo, Pb, Sb, Se, and Zn (excluding Au and Ag)). Similarly, overall data can be explained sufficiently using the first three Principal Components (PC), which define a cumulative overall variance of 59.2%, and are the only ones with eigenvalues that exceed 1.00.

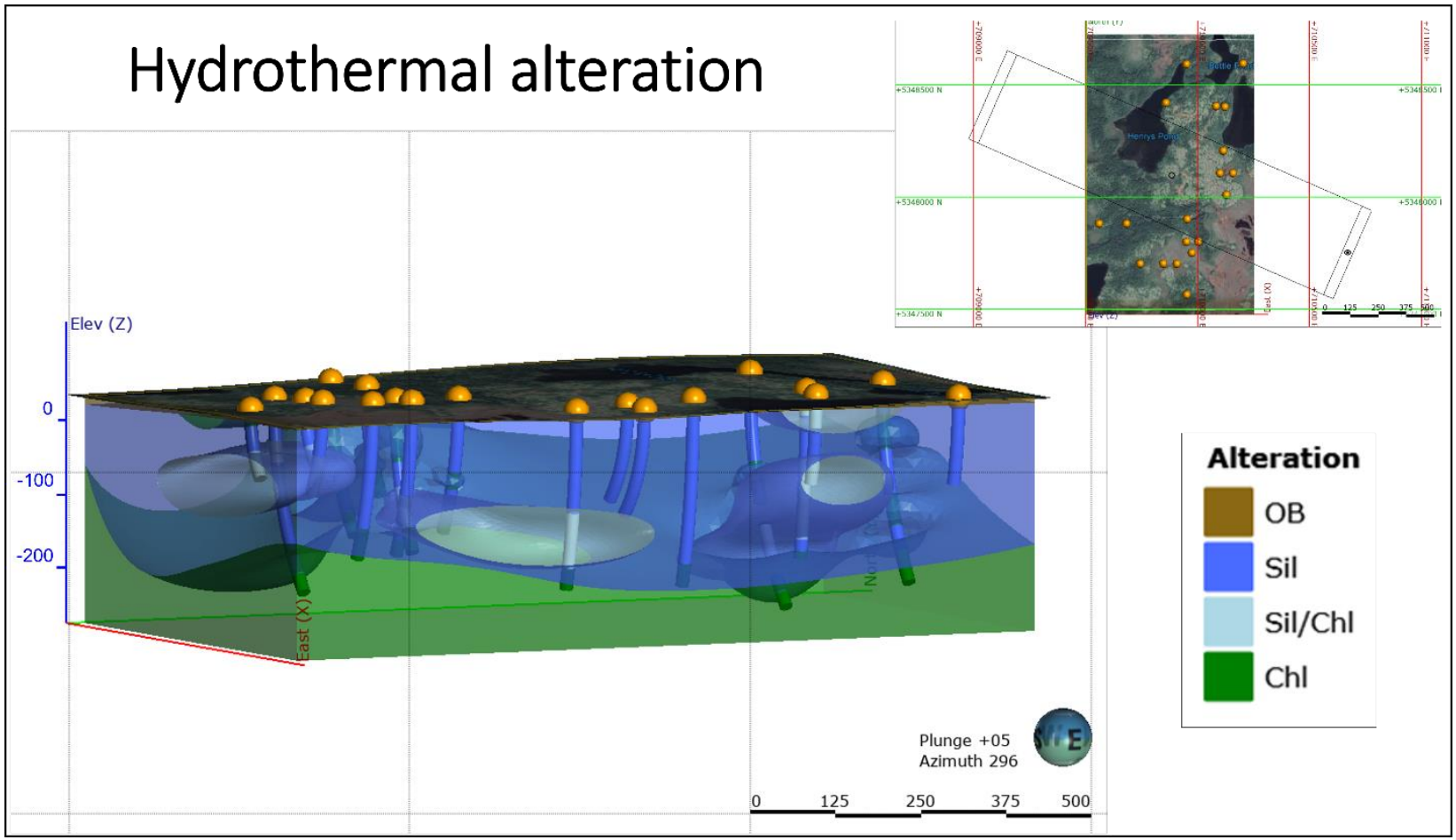

Figure 3.16 Generalized hydrothermal alteration model for Big Easy DDH data. OB: Overburden, Sil: Silica alteration, Sil/Chl: Silica and chlorite alteration, Chl: Chlorite alteration. Localized and minor alterations are not included in the model; these encompass quartz/chalcedony, adularia/sericite, illite/smectite, and carbonate, which are generally restricted to narrow vein selvages. Chlorite

alteration is largely restricted to the footwall of drilled volume. Silica alteration comprises a volumetrically extensive zone that encapsulates most of the Au-Ag mineralized veining studied herein.

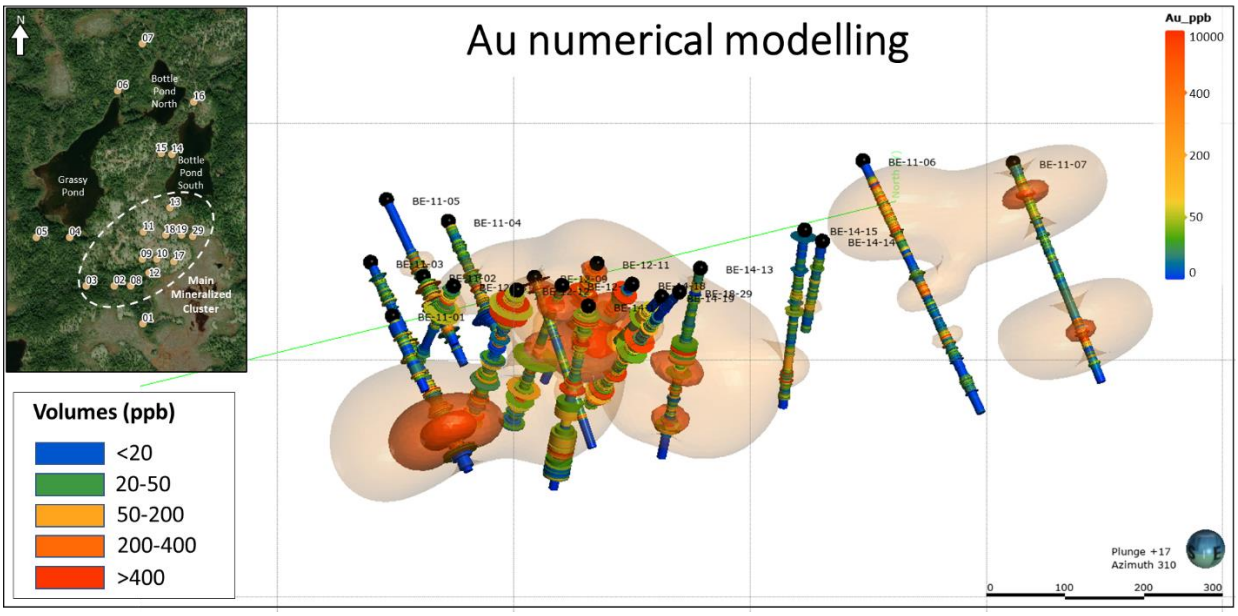

Figure 3.17 Generalized Au numerical model showing data from drilling programs. Volumes are colour coded for Au concentration ranges in ppb. A high-gold cluster located to the southeast of Grassy Pond (white dashed oval in inset map) currently represents the most prospective, and most explored, area on the Big Easy property. The interpolation method used for building numerical models (Figs. 3.17-3.20) was the linear variogram. The interpolated value at any specific point is the weighted sum of the data points in a finite interval, which means that any point in space that is more than the distance range of a data sample will have an interpolated value that is either zero or an estimate of the mean value.

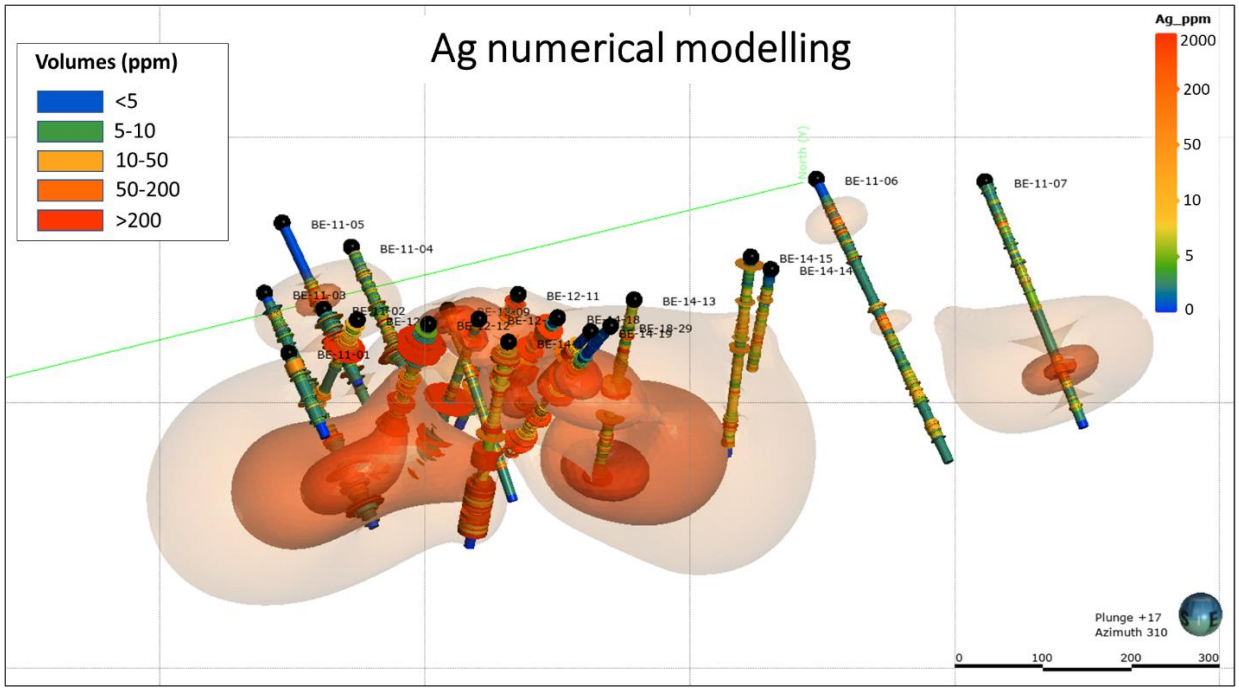

Figure 3.18 Generalized Ag numerical model showing data from drilling programs. Volumes are colour coded for Ag concentration ranges in ppm. The most prospective areas currently overlap with those in Figure 3.17 because of the strong positive correlation between gold and silver.

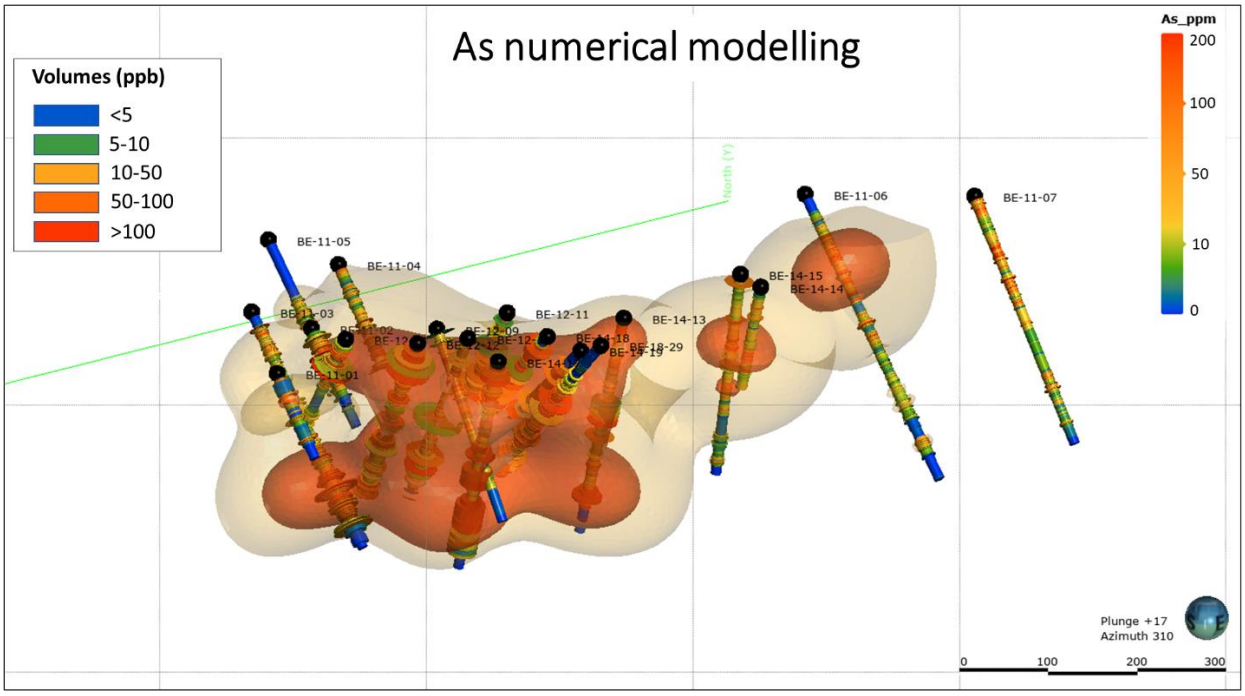

Figure 3.19 Generalized As numerical model showing data from drilling programs. Volumes are colour coded for As concentration ranges in ppm. A strong empirical spatial relationship between As and Au-Ag is found in the southeast portion of the drilled area, supporting the correlation observed in PCA analyses.

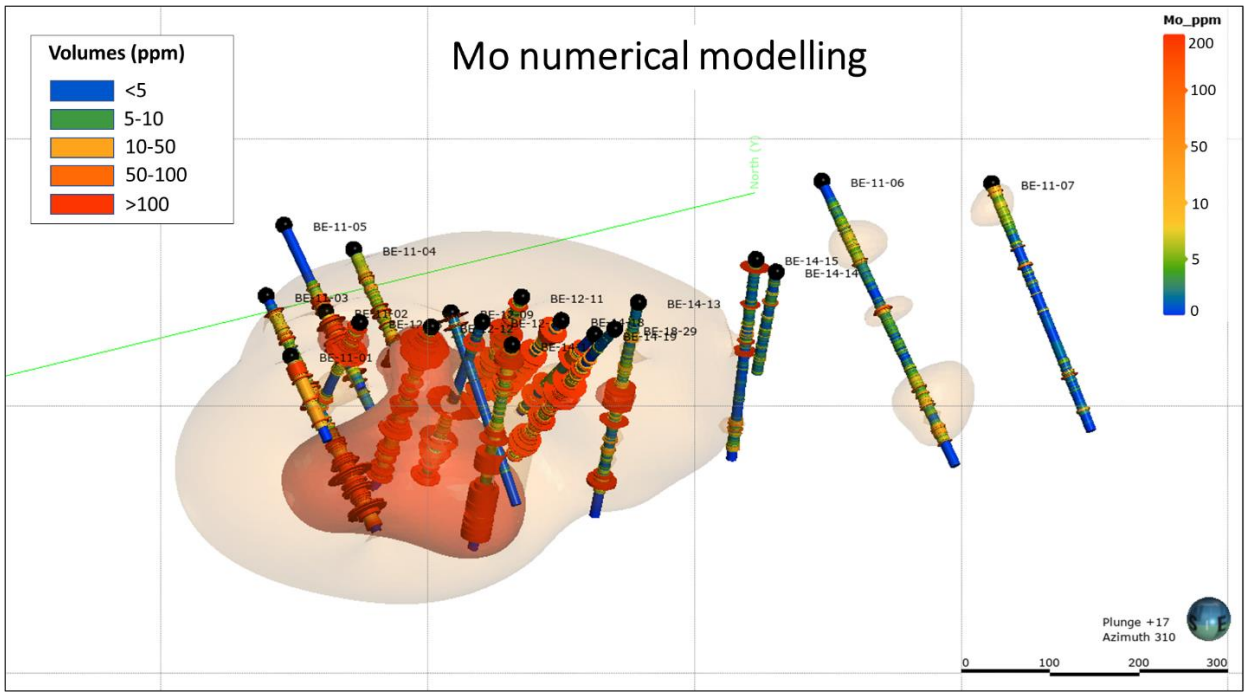

Figure 3.20 Generalized Mo numerical model showing data from drilling programs. Volumes are colour coded for Mo concentration ranges in ppm. A localized spatial relationship between Mo and As is observed in the southeast of the drilled area. A strong empirical spatial relationship also exists between Mo and Au-Ag in the southeast portion of the drilled area, although somewhat more volumetrically restricted (at the >5 ppm threshold) than that for As and Au-Ag, also supporting the correlation observed in PCA analyses.

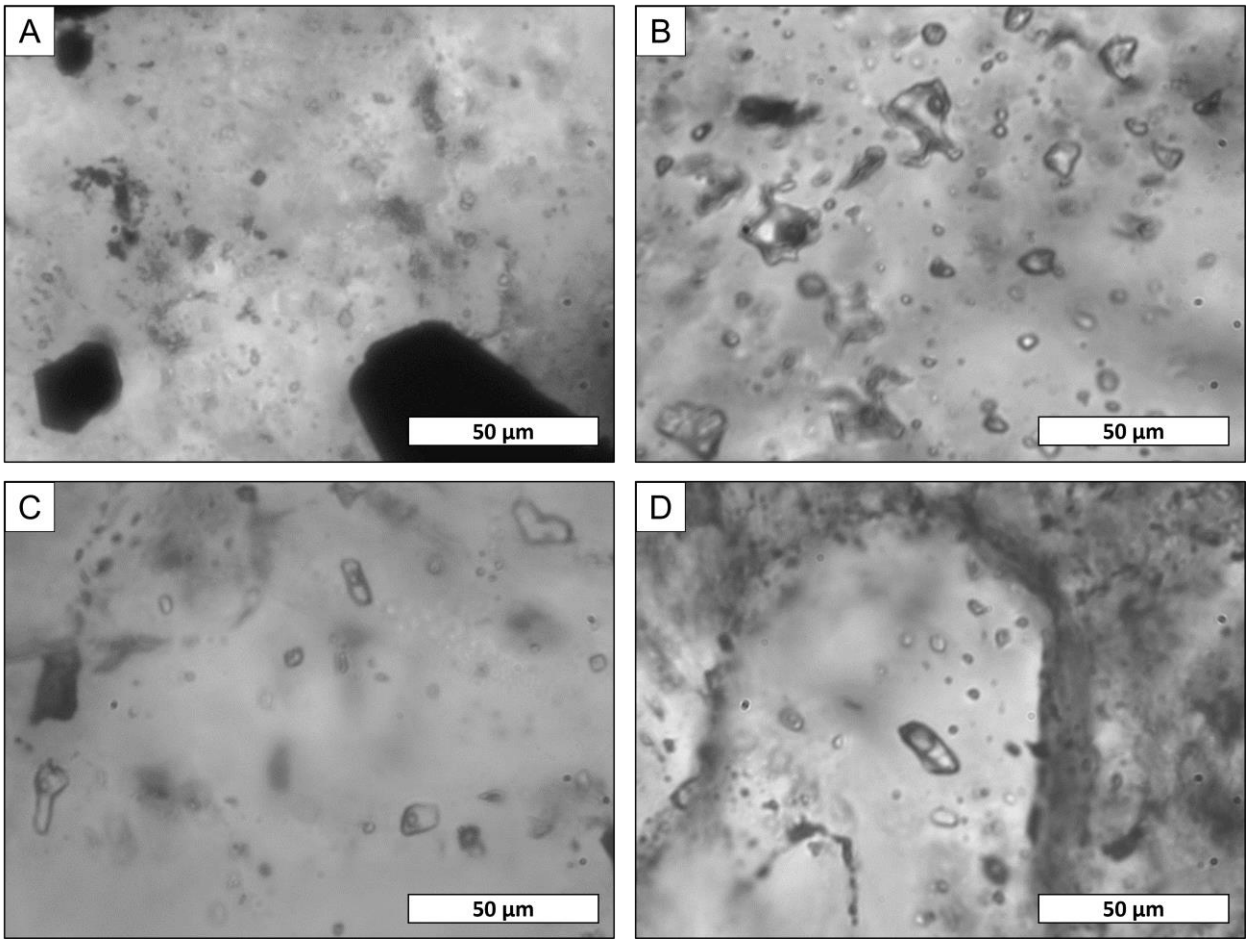

Figure 3.21 Photomicrographs of selected primary liquid-vapor (L-V) Fluid Inclusion Assemblages (FIAs) from mineralized quartz/adularia veins. A) Type I: High Au (Electrum dominant). High density of small (5 µm and less) primary two-phase fluid inclusions hosted in adularia with an L:V ratio close to 2:1; B) Type II: High Au:Ag. Primary fluid inclusions ranging from 15 to 25 µm hosted in quartz. Liquid proportion is higher than in type I, with an average L:V ratio of 5:1; C) Type III: High Ag:Au (Ginguro). These veins show the lowest population density of primary fluid inclusions. However, the quality is good enough to obtain reliable data. L:V ratio is close to 3:1; and D) Type IV: Molybdenite-rich. Largest primary inclusion of 25 µm with a tentative rare daughter crystal (possibly a negative quartz crystal host artifact) and an L:V ratio of 1:1, surrounded by the smallest (5 to 10 µm) L-V inclusions in a quartz crystal.

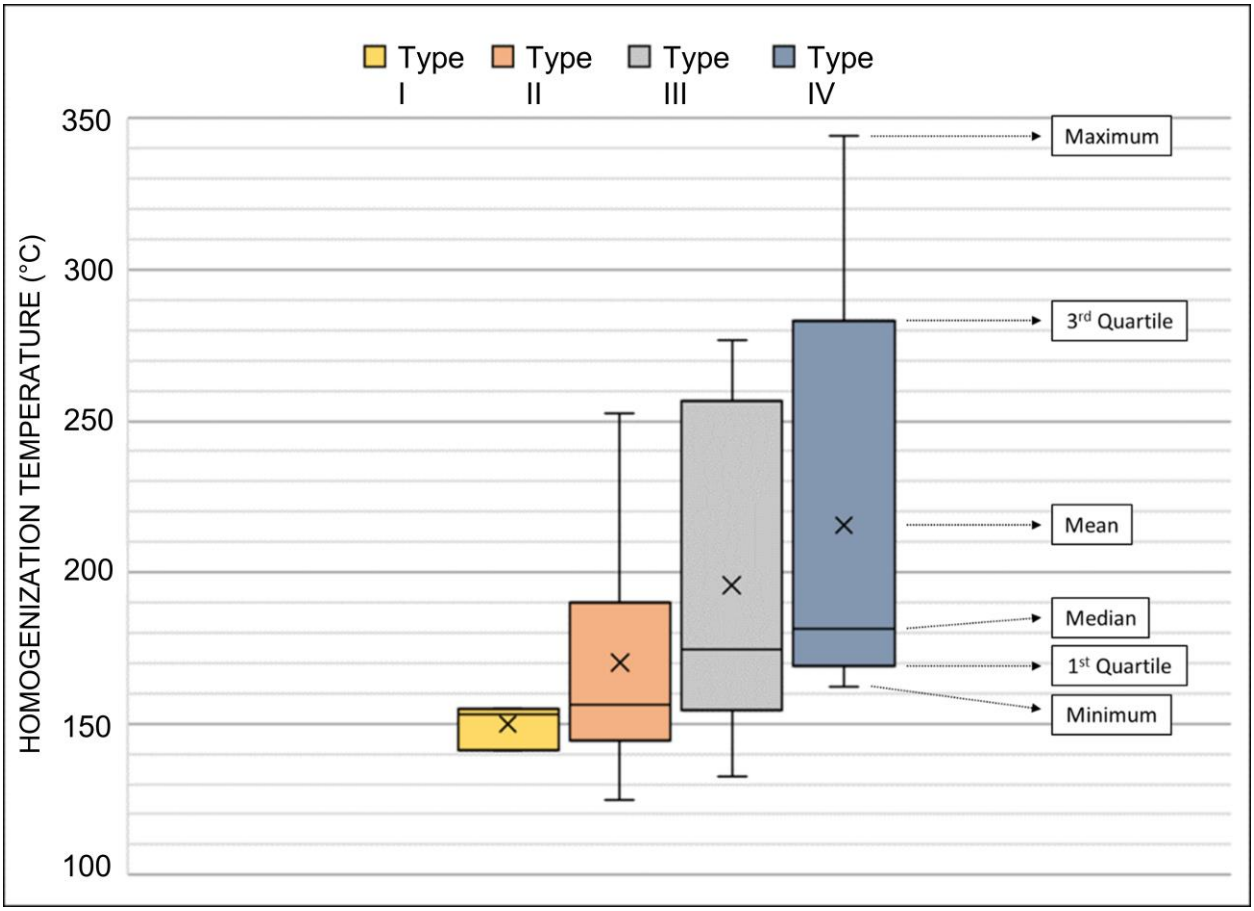

Figure 3.22 Homogenization temperatures for fluid inclusion assemblages from mineralized veins in the Big Easy prospect. Type I: High Au (Electrum dominant); Type II: High Au:Ag; Type III: High Ag:Au (Ginguro); and Type IV: Molybdenite-rich. Samples used here are listed in Table 3.2.

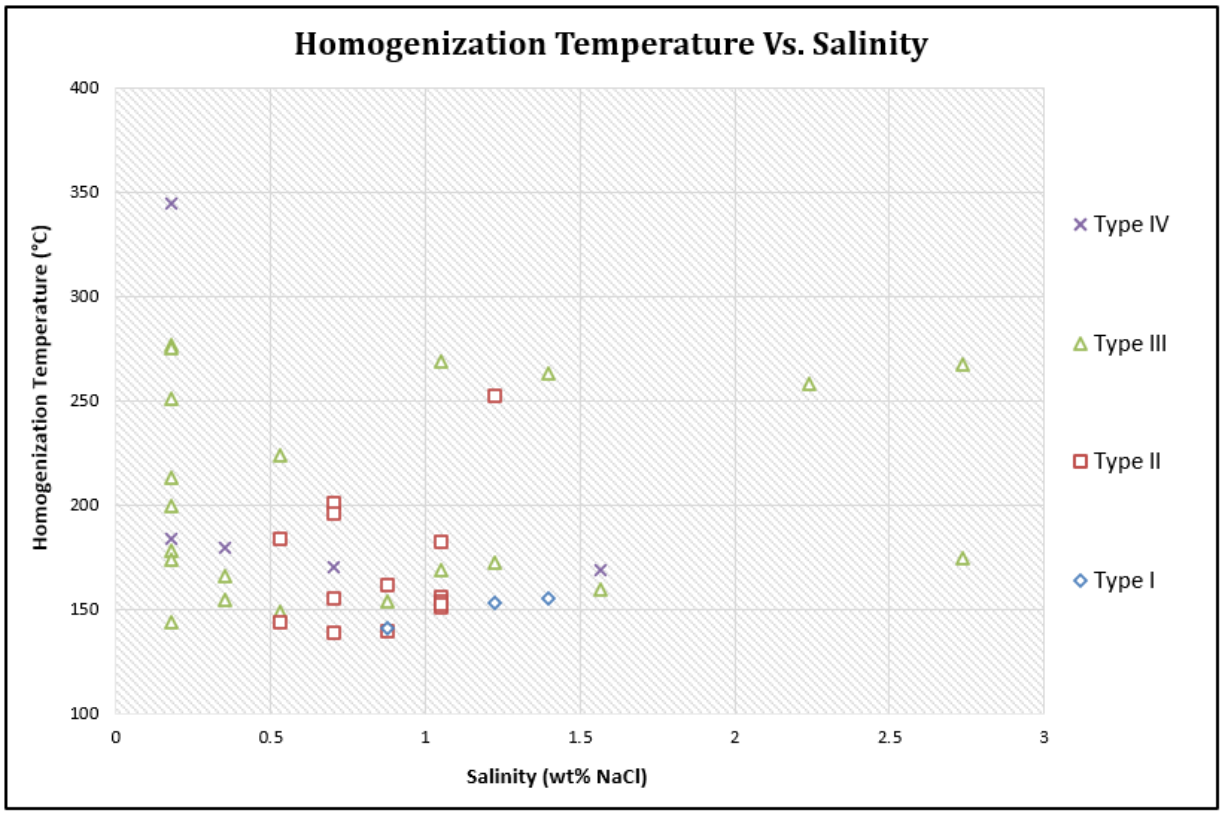

Figure 3.23 Homogenization temperature-salinity diagram for measured inclusions by Vein Type (I-IV). Plotting scheme adopted from Wilkinson (2001). Samples where freezing measurements were not possible (see Table 3.2) are not plotted here.

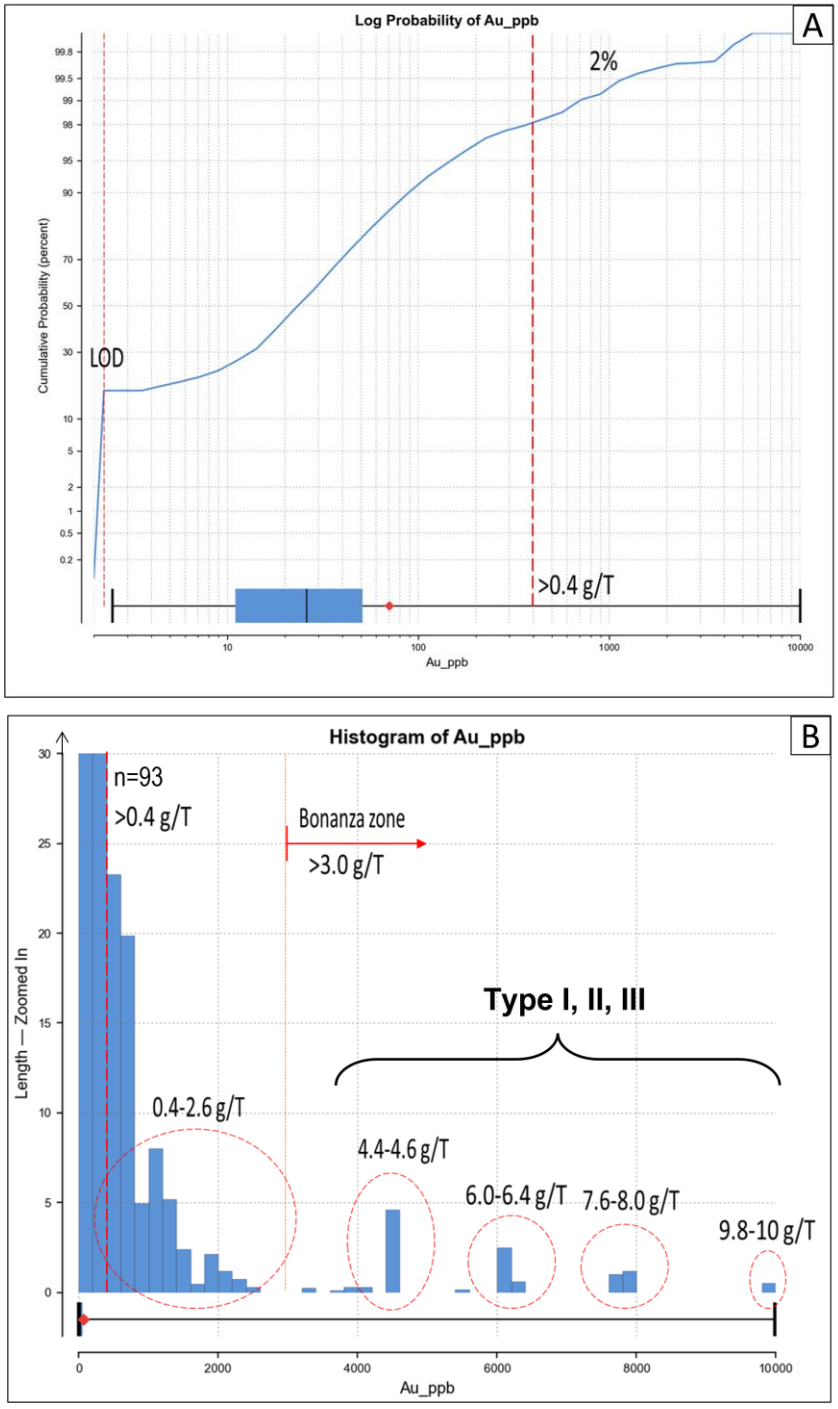

Figure 3.24 Plots for Au values in core assays (n=2946 samples). A) Log probability plot. Cut-off = 0.4 g/t. LOD: Limit of Detection; and B) Histogram of gold concentrations. Gold values >0.4

g/t are mainly concentrated in intervals containing vein types I, II, and III. The gold contribution of type IV veins is negligible in the existing database and is not labelled here.

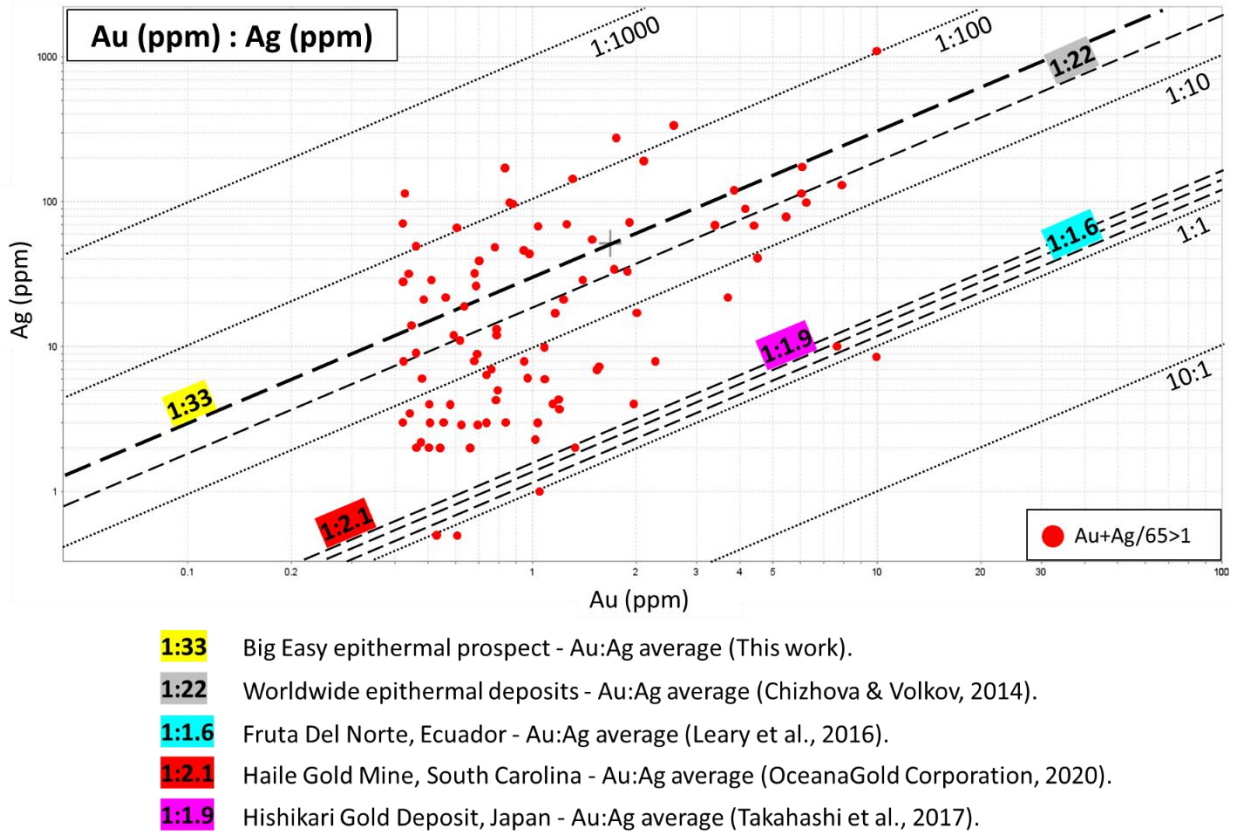

Figure 3.25 Comparison of Au:Ag ratios average between the Big Easy prospect and worldwide epithermal deposits (as compiled by Chizhova & Volkov, 2014), Fruta Del Norte, Haile Gold Mine, and Hishikari Gold Deposit. These latter statistics are largely based on mine production data. Data presented for Big Easy represent exploration drill core assays for which (Au+Ag/65) > 1 ppm, plotted as red dots.

Type I: BE11-07 43.5

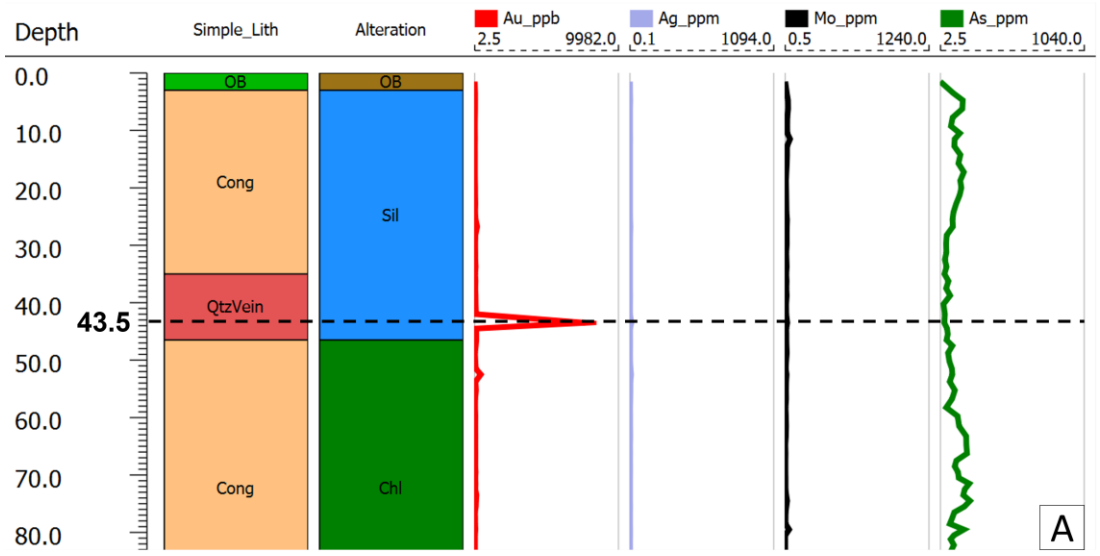

Type II: BE 14-19 148.6

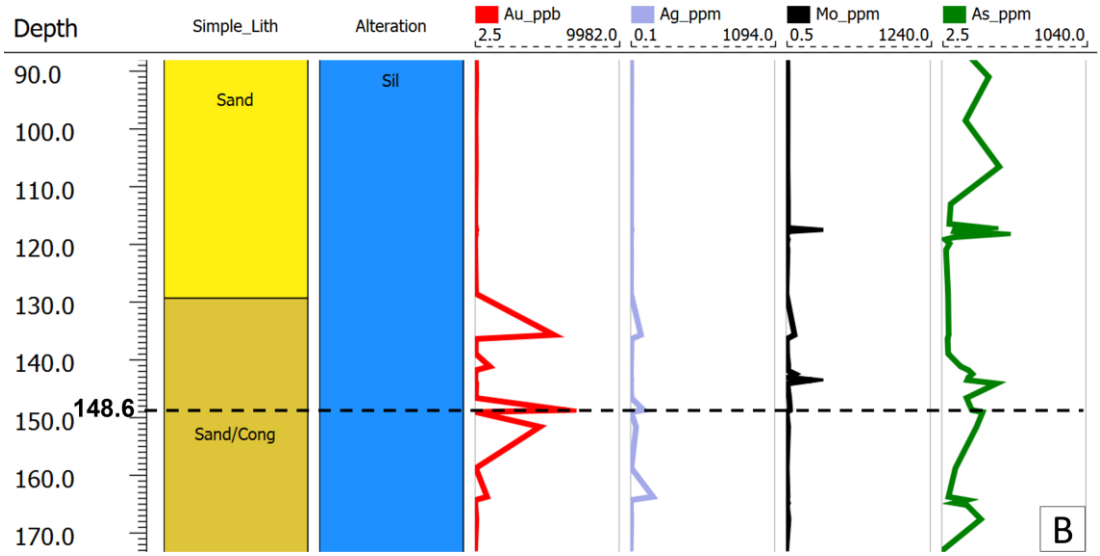

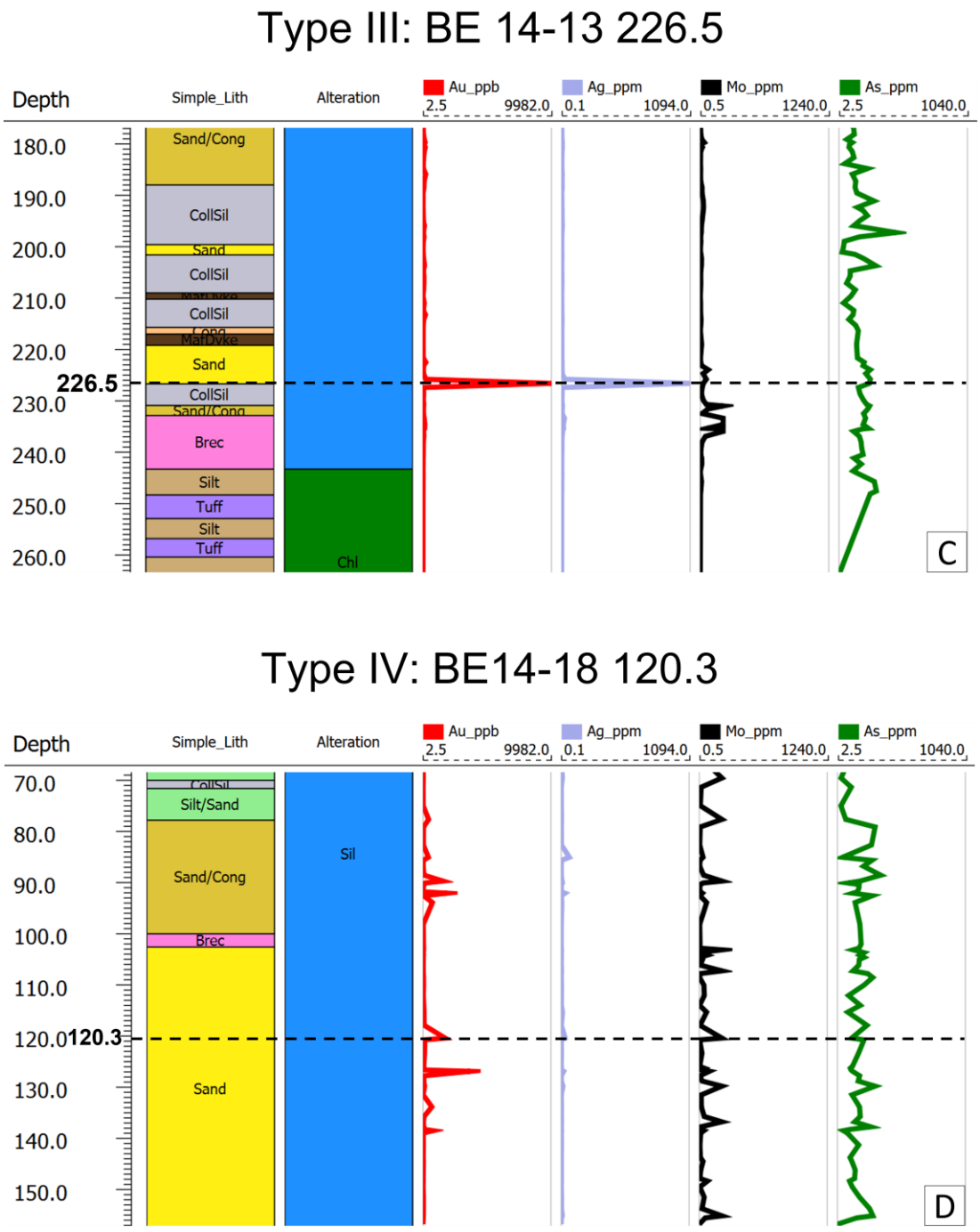

Figure 3.26 Drill hole correlation showing lithology, generalized hydrothermal alteration, and gold, silver, molybdenum, and arsenic values. A) Type I vein; B) Type II vein; C) Type III vein; and D) Type IV vein. OB: Overburden, Cong: Conglomerate, Sand: Sandstone, Sand/Cong:

Mixture of sandstone and conglomerate, CollSil: Colloform Silica, MafDyke: Mafic dyke, Brec: Breccia, Silt: Siltstone, Silt/Sand: Mixture of siltstone and sandstone, Sil: Silica alteration, Chl: Chlorite alteration.

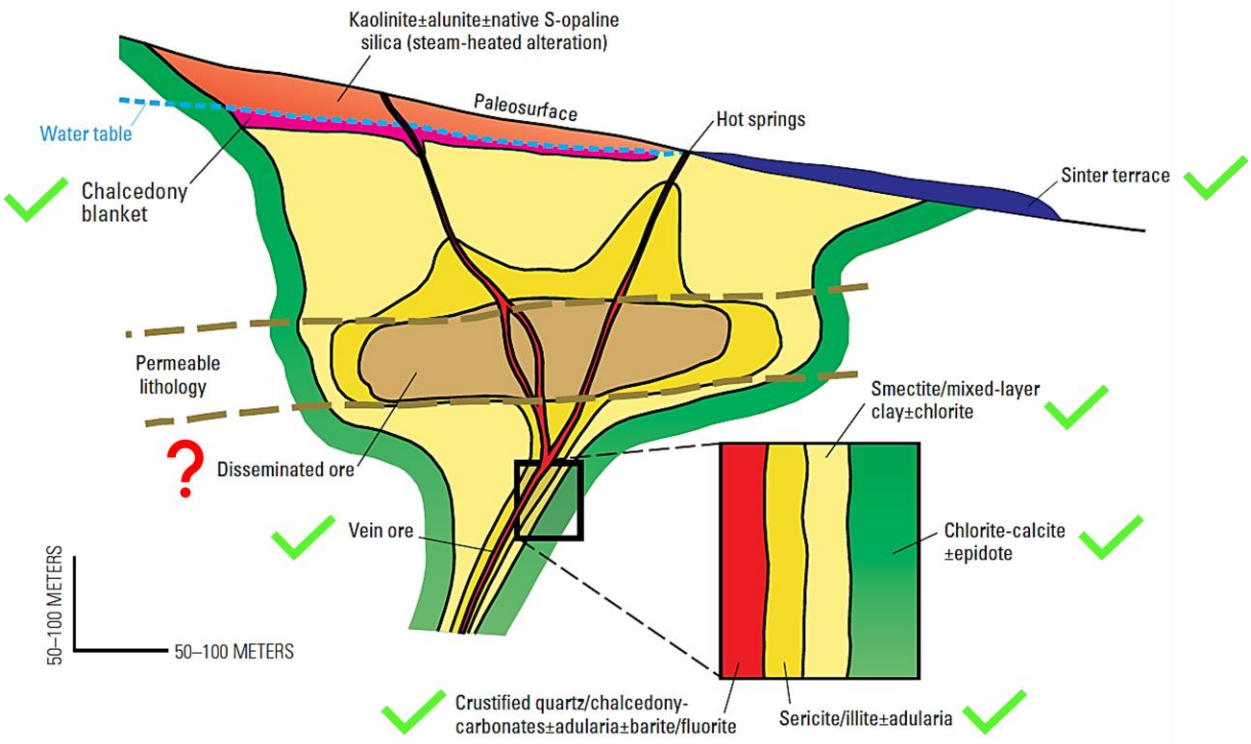

Figure 3.27 Classic low-sulfidation epithermal model showing typical mineralogical and structural characteristics. Those features found in Big Easy are selected with checkmarks. Modified from Hedenquist et al., 2000. Reproduced with permission (see Appendix 1).

Table 3.1 Samples selected for detailed petrography, SEM, and fluid inclusions analyses.

Sample #	DDH #	Depth (m)	Au (ppb)	Au (ppm)	Ag (ppm)	Au:Ag	As (ppm)	Cu (ppm)	Fe (%)	Pb (ppm)	Sb (ppm)	Se (ppm)	Zn (ppm)	Mo (ppm)	Description
159124	BE14-13 234.0	234.0	140	0.14	13.6	1:100	81	10	1.67	10	2.5	10	32	220	Core sample, hydrothermal breccia
159671	BE14-18 90.25	90.3	164	0.16	11.5	1:71	90	33	1.14	2.5	2.5	0.5	20	36	Core sample, crustiform vein
159693	BE14-18 115.15	115.2	89	0.09	12.1	1:143	87	33	1.72	5	11	0.5	54	71	Core sample, crustiform vein
159007	BE14-13 119.2	119.2	203	0.20	23.3	1:111	277	121	3.52	75	42	17	429	220	Core sample, cockade texture
948506	#11-10.8	10.8	4391	4.39	69	1:16	40	31	1.56	9	2.5	2.5	33	18	Petrography, host rock
159139	BE14-14 10.9	10.9	5	0.01	1	1:200	28	25	3.62	11	19	0.5	107	6	Petrography, host rock
553610	#9-5.45 / AX1	5.5	484	0.48	21	1:43	24	9	0.35	2	2.5	2.5	7	21	Petrography, host rock
159765	BE14-19 143.4	143.4	24	0.02	4.7	1:200	186	11	2.82	7	24	5	63	220	Petrography, host rock
721240	BE11-7 43.5	43.5	7645	7.65	10	1:1.3	30	6	0.9	11	2.5	10	26	18	Type I) High Au (Electrum dominant)
159667	BE14-18 85.2-4	85.2	421	0.42	70.6	1:167	45	12	0.94	9	2.5	0.5	48	37	Type II) High Au:Ag-rich
159768	BE14-19 148.6-1	148.6	6229	6.23	98.7	1:16	219	28	2.67	6	35	8	80	34	Type II) High Au:Ag-rich
159750	BE14-19 117.4	117.4	89	0.09	7.9	1:91	96	54	2.07	5	15	9	200	220	Type III) High Ag:Au (Ginguro), core sample
948504	#11-10.2	10.2	1909	1.91	72	1:37	20	11	0.83	11	2.5	2.5	23	25	Type III) High Ag:Au (Ginguro)
948842	#12-202.6A	202.6	7894	7.89	130	1:16	74	45	3.02	16	2.5	5	37	20	Type III) High Ag:Au (Ginguro)
948842	#12-203.4A	203.4	7894	7.89	130	1:16	74	45	3.02	16	2.5	5	37	20	Type III) High Ag:Au (Ginguro)
159658	BE14-18 54.2	54.2	3855	3.86	119.6	1:31	24	20	1.03	6	2.5	4	51	28	Type III) High Ag:Au (Ginguro)
159115	BE14-13 226.5A	226.5	9967	9.97	1094	1:111	64	26	2.43	43	2.5	21	225	29	Type III) High Ag:Au (Ginguro)
159115	BE14-13 226.5B	226.5	9967	9.97	1094	1:111	64	26	2.43	43	2.5	21	225	29	Type III) High Ag:Au (Ginguro)
159694	BE14-18 120.3-2	120.3	1729	1.73	34.3	1:20	118	16	2.18	6	2.5	0.5	62	7220	Type IV) Molybdenite-rich

Table 3.2 Summary of samples used in fluid inclusions microanalysis. *Type I vein contains the most difficult samples to study due to the small size of the fluid inclusions. Only one Fluid Inclusion Assemblage (FIA) was clearly measured. In some inclusions, salinity can not be calculated because of the lack of certainty in final melting ice temperatures.

Sample	Veinlet type	Chip	FIA	Phases	IF	Final Melting Ice T (°C) (Tm)	Homogenization T (°C)	Salinity (%)
BE11-7-43.5	Type I) High Au (Electrum dominant)*	V2	1	2	1	-0.7	153.2	1.2
					2	-0.8	155.1	1.4
					3	-0.5	141.3	0.9
BE14-18-85.2-4	Type II) High Au:Ag-rich	V1b	1	2	1	2.2	124.7	x
					2	3.5	173.6	x
					3	3.2	175.2	x
		V2	2	2	1	-0.6	151.2	1.1
					2	-0.6	182.4	1.1
					3	-0.7	252.6	1.2
					4	-0.5	162	0.9
			3	2	5	4.8	x	x
					6	-0.4	201.2	0.7
					7	-0.6	156.2	1.1
					8	-0.5	139.8	0.9
					9	-0.5	x	0.9
					10	-0.6	153.6	1.1
		V3	4	2	1	-0.4	195.7	0.7
				3(?)	2	-0.3	184.1	0.5
				2	3	-0.3	143.9	0.5
				3(?)	4	-0.4	155.2	0.7
				2	5	x	144.6	x
					6	x	210.1	x
					7	-0.4	138.9	0.7
					8	x	235.4	x
BE-14-19-148.6-1	Type II) High Au:Ag-rich	5-6	1	2	1	-0.6	x	1.1
					2	-0.5	x	0.9
					3	-0.6	142.8	1.1
					4	-0.6	152.1	1.1
#12-202.6A	Type III) High Ag:Au (Ginguro)	V3FI1	1	2	1	-0.8	263.1	1.4
					2	-1.3	258.4	2.2
					3	-0.9	159.4	1.6
					4	-1.6	174.8	2.7
					5	-0.7	172.6	1.2
					6	-0.6	168.9	1.1
		FI2	2	2	1	-1.6	267.3	2.7
					2	-0.6	268.9	1.1
					3	-0.1	251.1	0.2
					4	-0.2	165.7	0.4
		V2-FI1-2	3	2	1	-0.3	223.6	0.5
					2	-0.3	148.6	0.5
					3	-0.5	154.1	0.9
#11-10.2	Type III) High Ag:Au (Ginguro)	V3	1	2	1	-0.1	177.8	0.2
					2	-0.1	199.6	0.2
					3	-0.1	143.8	0.2
					4	-0.1	276.9	0.2
					5	x	136.8	x
					6	x	134.2	x
		V2	2	2	1	-0.1	173.8	0.2
					2	-0.1	213.1	0.2
					3	-0.1	275.5	0.2
					4	x	132.6	x
					5	-0.2	154.8	0.4
BE14-18 120.3-2	Type IV) Molybdenite-rich	V1F2	1	2	1	-0.1	344.3	0.2
					2	x	321.5	x
					3	-4.1	301.5	6.6
		V2F1	2	2	1	-0.2	179.6	0.4
					2	x	227.9	x
					3	-3.1	173.5	5.1
					4	x	184.6	x
					5	-0.1	183.5	0.2
					6	-0.9	168.8	1.6
		V1F1	3	2	1	-0.4	170.4	0.7
					2	x	167.8	x
					3	x	162.4	x

Table 3.3 Homogenization temperatures, final melting points, and salinity comparison for examples of low and intermediate-sulfidation epithermal gold/silver deposits globally. IS: Intermediate-Sulfidation.

Author	Deposit	Homogenization T (°C)			Salinity (wt% NaCl eq.)		
		From	To	Avg	From	To	Avg
Junco, 2022 (this work)	Big Easy Prospect	124.7	301.5	183.4	0.18	2.7	0.85
Etoh et al., 2002	Hishikari Gold Deposit, Japan	175	215		0.2	2.1	0.9
Shikazono, 2003	Au-Ag rich (Neogene vein deposits in Japan)	190	250		0	3	
Shikazono & Shimizu, 1992	Sado, Japan	190	305		1	2.5	
	Seigoshi, Japan	178	243		0	2.8	
	Yatani, Japan	209	273		0.5	1.5	
	Ohguchi, Japan	184	265		0	1.6	
	Todoroki, Japan	122	240		0.4	1.7	
	Koryu, Japan	140	300		0	1.4	
	Chitose, Japan	220	300		1	2	
	Kushikino, Japan	210	250		0.6	1.1	
Robinson & Norman, 1984	Creede Mining District - IS (lower levels), USA	170	260	238	6	13	9.8
	Creede Mining District - IS (upper levels), USA	140	200	170	3	10	6.5
Simpson et al., 2001	Golden Cross Epithermal Au-Ag deposit, New Zealand	150	240		0	2.4	
Mango et al., 2014	Guanajuato Epithermal District - IS, Mexico	200	300	258	0	3	
Canet et al., 2011	Bolaños Ag-Au-Pb-Zn epithermal deposit -IS, Mexico	224	241	232	7.6	9.2	8.3
Wallier et al., 2006	Roşia Montană Au-Ag deposit, Romania	200	270		0.2	3.4	
Volkov et al., 2012	Kupol Au–Ag Epithermal Deposit, Russia	211	276	233	0.5	2.1	1.5
	Dvoinoi Au–Ag Epithermal Deposit, Russia	154	251	196	0.8	0.1	0.9
	Arykvaam Au–Ag Epithermal Deposit, Russia	234	267	247	0.8	0.8	0.8

Table 3.4 Selected geochemical results for Big Easy samples. These are all existing data that exceed a gold cut-off of Au >400 ppb. Samples are ranked in descending order of Au concentration.

Sample Number	Program	DDH #	Au (ppb)	Au (ppm)	Ag (ppm)	Au+(Ag/65)	Ag/Au	Al (%)	As (ppm)	Ba (ppm)	Be (ppm)	Bi (ppm)	Ca (%)	Cd (ppm)	Co (ppm)	Cr (ppm)	Cu (ppm)	Fe (%)	K (%)	Mg (%)	Mn (ppm)	Mo (ppm)	Na (%)	Ni (ppm)	P (%)	Pb (ppm)	Sb (ppm)	Se (ppm)	Sn (ppm)	Sr (ppm)	Ti (%)	V (ppm)	W (ppm)	Zn (ppm)
159115	2014	BE-14-13	9967	9.967	1094	26.80	109.8	4.31	64	5	0.5	1.0	0.11	1.5	5	200	26	2.43	0.39	1.12	520	29	0.25	8	0.01	43	2.5	21	10	4	1.16	55	5	225
159044	2014	BE-14-13	9982	9.982	9	10.11	0.9	5.50	46	15	1.4	1.0	0.21	0.5	7	94	13	2.69	0.32	1.19	962	17	0.20	10	0.05	9	42	0.5	10	4	1.97	70	5	78
948842	2012	BE-12-12	7894	7.894	130	9.89	16.5	0.52	74	7	1.0	0.5	0.30	2.0	10	73	45	3.02	0.20	0.33	337	20	0.03	83	0.05	16	2.5	5	5	3	1.19	34	5	37
619682	2011	BE-11-03	6052	6.052	174	8.73	28.8	1.75	182	8	6.0	18	0.48	5.0	17	33	79	7.58	0.22	0.78	419	172	0.02	45	0.08	26	2.5	13	5	4	4.69	61	14	90
721240	2011	BE-11-07	7645	7.645	10	7.80	1.3	0.16	30	5	1.0	0.5	0.20	2.0	2	52	6	0.90	0.08	0.08	110	18	0.01	84	0.01	11	2.5	10	5	14	0.05	24	5	26
619685	2011	BE-11-03	6043	6.043	114	7.80	18.9	1.49	139	7	2.0	17	0.43	2.0	10	30	240	6.09	0.17	0.67	445	66	0.02	34	0.06	26	2.5	16	5	4	0.91	39	14	99
159768	2014	BE-14-19	6229	6.229	99	7.75	15.8	4.71	219	22	0.9	1.0	0.20	0.9	11	131	28	2.67	0.45	1.24	625	34	0.27	10	0.05	6	35	8	10	5	3.14	79	5	80
721359	2011	BE-11-07	2569	2.569	335	7.72	130.4	0.73	24	3	4.0	12	1.65	2.0	11	32	26	2.08	0.07	0.43	762	0.5	0.02	48	0.07	46	2.5	2.5	5	16	0.05	67	5	29
159758	2014	BE-14-19	5463	5.463	79	6.67	14.4	2.92	52	16	3.2	1.0	0.05	0.3	12	145	32	1.79	0.44	0.44	155	72	0.23	9	0.01	2.5	15	10	10	4	0.61	94	5	87
553611	2012	BE-12-09	1755	1.755	276	6.00	157.3	0.24	19	4	1.0	0.5	0.06	2.0	1	38	115	0.65	0.15	0.14	138	309	0.02	49	0.01	4	2.5	22	5	1.5	0.05	11	5	76
159658	2014	BE-14-18	3855	3.855	120	5.70	31.0	2.53	24	12	0.6	2.0	0.05	0.3	3	173	20	1.03	0.44	0.35	152	28	0.17	8	0.01	6	2.5	4	10	4	0.48	37	5	51
553813	2012	BE-12-10	4135	4.135	90	5.52	21.8	0.33	58	4	1.0	0.5	0.09	2.0	5	19	13	1.02	0.07	0.35	244	90	0.01	26	0.01	2	6	2.5	5	1.5	0.70	29	5	28
948506	2012	BE-12-11	4391	4.391	69	5.45	15.7	0.50	40	5	1.0	13	0.03	2.0	4	70	31	1.56	0.09	0.33	300	18	0.03	52	0.01	9	2.5	2.5	5	1.5	0.44	34	5	33
159770	2014	BE-14-19	4492	4.492	41	5.13	9.2	3.77	253	15	0.6	1.0	0.19	1.1	12	162	26	2.87	0.45	1.04	422	17	0.26	18	0.05	5	15	8	10	4	2.90	53	5	44
553810	2012	BE-12-10	2113	2.113	191	5.05	90.4	0.29	93	5	1.0	3.0	0.08	2.0	4	31	17	1.15	0.11	0.24	189	109	0.01	42	0.01	2	2.5	6	5	1.5	0.61	25	5	46
553804	2012	BE-12-10	3396	3.396	68	4.44	20.0	0.21	77	4	1.0	0.5	0.11	2.0	4	27	8	1.08	0.11	0.14	117	68	0.01	33	0.03	2	2.5	2.5	5	1.5	0.63	32	5	17
159699	2014	BE-14-18	3695	3.695	22	4.03	5.9	5.36	126	17	0.9	1.0	0.16	0.6	8	139	22	2.18	0.39	1.31	867	98	0.23	10	0.04	8	2.5	0.5	10	5	2.64	113	5	60
553622	2012	BE-12-09	1312	1.312	144	3.53	109.8	0.28	70	5	1.0	0.5	0.04	2.0	3	53	83	1.19	0.13	0.21	179	156	0.02	46	0.01	8	2.5	8	5	1.5	0.23	21	5	39
159772	2014	BE-14-19	834	0.834	170	3.46	204.3	4.13	51	24	0.6	1.0	0.07	0.3	4	167	32	1.17	0.71	0.78	279	12	0.30	9	0.02	2.5	16	6	10	5	1.03	31	5	53
948504	2012	BE-12-11	1909	1.909	72	3.02	37.7	0.31	20	4	1.0	0.5	0.06	2.0	2	63	11	0.83	0.09	0.25	191	25	0.03	34	0.02	11	2.5	2.5	5	1.5	0.19	21	5	23
553855	2012	BE-12-10	2279	2.279	8	2.40	3.5	0.74	286	8	2.0	3.0	0.37	6.0	18	38	29	6.70	0.19	0.59	553	8	0.03	38	0.05	16	2.5	2.5	5	4	0.89	77	5	182
159675	2014	BE-14-18	1891	1.891	33	2.40	17.5	3.74	129	11	0.6	1.0	0.13	1.9	6	156	18	1.92	0.34	0.92	492	31	0.18	9	0.03	2.5	2.5	0.5	10	6	1.40	95	5	57
619677	2011	BE-11-03	878	0.878	97	2.37	110.5	0.79	74	7	1.0	14	0.23	2.0	2	36	51	2.37	0.19	0.27	146	26	0.02	53	0.03	22	5	12	5	3	0.69	20	13	42
948844	2012	BE-12-12	860	0.86	98	2.37	114.0	0.27	115	6	1.0	0.5	0.23	2.0	5	86	125	2.97	0.20	0.08	116	137	0.03	117	0.05	24	2.5	2.5	5	3	0.28	23	5	32
619704	2011	BE-11-03	1493	1.493	55	2.34	36.8	1.18	89	8	1.0	17	0.19	2.0	3	33	64	3.02	0.17	0.51	230	39	0.02	41	0.05	14	2.5	14	5	1.5	0.92	29	12	55
948841	2012	BE-12-12	1261	1.261	70	2.34	55.5	0.50	378	20	1.0	10	0.11	4.0	7	80	91	6.72	0.40	0.13	169	35	0.02	135	0.02	26	9	2.5	5	5	0.21	41	5	50
553619	2012	BE-12-09	2015	2.015	17	2.28	8.4	0.21	36	2	1.0	0.5	0.02	2.0	2	28	31	0.78	0.05	0.20	136	17	0.01	23	0.01	2	2.5	2.5	5	8	0.05	22	5	18
159694	2014	BE-14-18	1729	1.729	34	2.26	19.8	4.87	118	19	1.2	1.0	0.18	0.5	9	143	16	2.18	0.41	1.15	652	220	0.21	13	0.04	6	2.5	0.5	57	5	3.20	108	5	62
553624	2012	BE-12-09	427	0.427	114	2.18	267.0	0.22	39	3	1.0	6.0	0.07	2.0	2	68	515	0.82	0.13	0.14	106	121	0.02	49	0.02	10	2.5	2.5	5	1.5	0.23	34	5	51
619681	2011	BE-11-03	1040	1.04	67	2.07	64.4	1.70	232	9	4.0	19	0.66	5.0	23	35	79	7.90	0.26	0.66	356	176	0.02	46	0.10	28	2.5	12	5	5	6.91	72	15	76
553847	2012	BE-12-10	1972	1.972	4	2.03	2.0	0.32	101	7	1.0	0.5	0.26	2.0	12	41	15	3.19	0.19	0.19	181	4	0.03	43	0.05	7	2.5	2.5	5	1.5	0.76	26	5	52
619705	2011	BE-11-03	1399	1.399	29	1.85	20.7	1.17	72	5	1.0	17	0.17	2.0	2	28	116	2.45	0.15	0.53	227	122	0.02	36	0.03	18	2.5	11	5	1.5	1.04	35	12	49
159670	2014	BE-14-18	1562	1.562	7	1.67	4.6	4.40	187	15	0.9	3.0	0.19	2.8	10	115	13	2.40	0.40	1.07	584	220	0.17	13	0.03	2.5	2.5	0.5	10	7	2.24	126	5	58
721361	2011	BE-11-07	981	0.981	44	1.66	44.9	0.30	50	5	1.0	11	0.44	2.0	4	33	7	1.27	0.12	0.13	174	2	0.02	40	0.02	38	5	2.5	5	3	0.05	19	5	29
721348	2011	BE-11-07	1549	1.549	7	1.66	4.5	0.32	138	2	1.0	15	0.70	30.0	12	50	13	2.14	0.06	0.16	269	11	0.02	74	0.05	1053	2.5	2.5	5	3	0.05	37	5	626
619706	2011	BE-11-03	944	0.944	46	1.65	48.7	1.93	46	6	2.0	16	0.27	2.0	2	26	70	3.43	0.16	1.02	443	484	0.02	32	0.06	17	2.5	7	5	3	1.58	63	14	68
159656	2014	BE-14-18	604	0.604	67	1.63	110.4	2.74	83	13	5.9	1.0	0.08	0.8	7	141	21	1.13	0.51	0.23	109	32	0.19	7	0.02	2.5	2.5	0.5	10	4	0.14	50	5	56
721362	2011	BE-11-07	1234	1.234	21	1.56	17.0	0.24	236	2	1.0	18	0.39	7.0	6	53	7	4.75	0.04	0.09	165	19	0.02	65	0.15	40	14	2.5	5	3	0.05	73	5	185
948676	2012	BE-12-12	782	0.782	48	1.52	61.4	0.28	236	10	1.0	3.0	0.06	2.0	5	55	14	1.47	0.25	0.09	50	443	0.02	52	0.01	7	2.5	2.5	5	1.5	0.14	84	5	43
159667	2014	BE-14-18	421	0.421	71	1.51	167.7	3.85	45	32	0.9	1.0	0.06	1.1	3	223	12	0.94	0.79	0.35	178	37	0.24	23	0.01	9	2.5	0.5	10	9	0.61	50	5	48
948507	2012	BE-12-11	1162	1.162	17	1.42	14.6	1.13	70	9	1.0	14	0.12	2.0	9	40	18	2.77	0.14	0.98	755	5	0.02	27	0.03	11	2.5	2.5	5	3	1.12	69	5	66
553485	2011	BE-11-03	1334	1.334	2	1.36	1.5	0.36	18	6	1.0	16	0.21	2.0	2	34	13	2.58	0.13	0.06	102	11	0.02	44	0.02	5	2.5	13	5	3	0.28	7	13	25
159067	2014	BE-14-13	701	0.701	39	1.30	55.2	5.26	145	5	1.4	1.0	0.33	1.8	12	93	15	3.94	0.18	1.24	861	24	0.18	12	0.12	9	49	0.5	10	4	1.55	77	5	74
159659	2014	BE-14-18	1192	1.192	4	1.26	3.6	3.54	207	10	0.9	2.0	0.13	3.4	9	154	12	2.55	0.50	0.51	226	30	0.22	12	0.03	2.5	2.5	0.5	10	6	1.38	53	5	66
159587	2014	BE-14-17	1201	1.201	4	1.26	3.1	3.21	291	11	0.8	4.0	0.16	5.4	15	133	22	3.49	0.39	0.50	208	220	0.20	12	0.04	6	2.5	0.5	78	5	1.31	55	5	66

553820	2012	BE-12-10	1086	1.086	10	1.24	9.2	0.56	81	7	1.0	2.0	0.06	2.0	8	41	21	2.12	0.18	0.48	291	10	0.02	57	0.02	6	2.5	2.5	5	1.5	0.05	49	5	38
619853	2011	BE-11-05	460	0.46	49	1.21	106.5	0.85	90	18	1.0	0.5	0.32	2.0	10	24	65	3.31	0.23	0.53	838	47	0.02	30	0.06	22	2.5	6	5	10	0.71	30	5	102
553849	2012	BE-12-10	1146	1.146	4	1.21	3.5	0.30	123	8	1.0	0.5	0.16	2.0	18	42	18	2.79	0.24	0.09	50	4	0.04	66	0.02	7	2.5	2.5	5	1.5	0.19	15	5	57
619790	2011	BE-11-04	1087	1.087	6	1.18	5.5	0.67	139	12	1.0	0.5	0.15	2.0	9	36	64	2.87	0.20	0.37	457	52	0.02	50	0.03	9	2.5	2.5	5	7	0.75	34	5	40
619686	2011	BE-11-03	682	0.682	32	1.17	46.9	1.24	124	7	2.0	19	0.31	2.0	8	31	154	5.66	0.21	0.46	318	115	0.02	45	0.06	29	2.5	12	5	4	1.36	39	12	83
619687	2011	BE-11-03	687	0.687	26	1.09	37.8	1.31	143	7	2.0	16	0.49	2.0	8	23	165	4.83	0.20	0.49	286	269	0.02	34	0.11	45	2.5	14	5	4	2.57	58	16	87
553853	2012	BE-12-10	1037	1.037	3	1.08	2.9	0.55	102	6	1.0	0.5	0.33	2.0	9	34	15	2.59	0.15	0.61	419	3	0.03	38	0.05	7	2.5	2.5	5	1.5	0.37	40	5	60
948815	2012	BE-12-12	948	0.948	8	1.07	8.4	0.48	49	5	1.0	0.5	0.23	2.0	7	72	15	1.83	0.17	0.31	281	29	0.03	89	0.06	8	2.5	2.5	5	4	0.82	25	5	30
553842	2012	BE-12-10	1052	1.052	1	1.07	1.0	0.44	311	9	1.0	0.5	0.09	2.0	8	34	12	2.67	0.22	0.38	275	1	0.03	42	0.02	8	2.5	2.5	5	1.5	0.05	21	5	55
159038	2014	BE-14-13	969	0.969	6	1.06	6.3	4.81	140	24	0.9	2.0	0.25	1.7	7	141	11	2.76	0.34	1.09	765	22	0.23	16	0.07	13	37	6	10	5	2.00	65	5	58
159761	2014	BE-14-19	1019	1.019	2	1.05	2.3	5.50	139	43	0.9	1.0	0.16	0.3	6	99	11	2.31	0.69	1.18	539	19	0.31	7	0.03	5	19	0.5	10	13	2.52	67	5	48
553912	2012	BE-12-10	788	0.788	13	0.99	16.5	0.48	91	8	1.0	2.0	0.33	2.0	7	48	18	2.43	0.18	0.41	363	16	0.01	60	0.07	15	5	2.5	5	4	0.80	30	5	55
721371	2011	BE-11-07	786	0.786	12	0.97	15.3	0.24	33	5	1.0	10	0.36	2.0	0.5	52	7	0.89	0.11	0.09	132	2	0.02	44	0.01	22	2.5	2.5	5	3	0.05	16	5	24
619673	2011	BE-11-03	510	0.51	29	0.96	56.9	1.22	184	9	3.0	16	0.62	2.0	9	31	189	5.81	0.29	0.33	229	244	0.02	48	0.09	44	6	13	5	8	3.29	43	15	85
619675	2011	BE-11-03	440	0.44	32	0.93	72.7	1.07	131	9	2.0	15	0.37	2.0	7	43	138	4.61	0.21	0.38	266	151	0.02	64	0.05	27	2.5	11	5	4	2.31	37	15	67
619703	2011	BE-11-03	636	0.636	19	0.93	29.9	0.98	74	5	1.0	12	0.21	2.0	3	30	120	2.66	0.13	0.44	195	30	0.02	34	0.05	17	2.5	15	5	1.5	1.23	28	11	45
159655	2014	BE-14-18	561	0.561	22	0.90	38.9	3.40	131	11	0.8	1.0	0.28	1.9	8	107	18	2.01	0.45	0.62	355	17	0.19	12	0.12	5	2.5	0.5	10	6	0.29	62	5	79
619788	2011	BE-11-04	838	0.838	3	0.88	3.6	1.02	112	13	1.0	0.5	0.24	2.0	12	24	21	3.31	0.25	0.65	695	16	0.02	31	0.05	11	2.5	5	5	8	0.93	39	5	58
619789	2011	BE-11-04	798	0.798	5	0.87	6.3	0.86	106	14	1.0	0.5	0.19	2.0	11	30	20	2.99	0.21	0.51	653	21	0.02	41	0.04	9	2.5	6	5	8	0.98	48	5	65
948816	2012	BE-12-12	760	0.76	7	0.87	9.2	0.54	71	8	1.0	0.5	0.39	2.0	12	61	17	3.11	0.22	0.35	309	31	0.03	71	0.09	12	2.5	2.5	5	6	1.72	38	5	47
159708	2014	BE-14-18	788	0.788	4	0.85	5.5	4.17	51	14	0.6	1.0	0.13	0.3	3	148	10	1.32	0.77	0.56	202	45	0.25	7	0.02	7	2.5	0.5	38	6	3.02	84	5	34
619674	2011	BE-11-03	423	0.423	28	0.85	66.2	1.08	185	9	2.0	14	0.38	2.0	10	46	130	5.92	0.28	0.27	192	62	0.02	74	0.06	26	2.5	13	5	5	2.68	37	13	75
159677	2014	BE-14-18	736	0.736	6	0.83	8.7	5.50	146	10	1.1	3.0	0.33	2.2	12	98	17	3.16	0.27	1.63	1011	72	0.17	12	0.12	2.5	2.5	0.5	10	5	1.87	183	5	91
553916	2012	BE-12-10	691	0.691	9	0.83	13.0	0.35	85	7	1.0	28	0.29	2.0	7	55	31	2.50	0.25	0.18	181	27	0.02	78	0.06	13	5	2.5	5	4	0.28	22	5	50
553610	2012	BE-12-09	484	0.484	21	0.81	43.4	0.09	24	2	1.0	7.0	0.01	2.0	0.5	7	9	0.35	0.05	0.05	50	21	0.01	8	0.01	2	2.5	2.5	5	1.5	0.05	4	5	7
553809	2012	BE-12-10	680	0.68	8	0.80	11.8	0.31	80	6	1.0	0.5	0.13	2.0	5	27	6	1.18	0.13	0.23	198	8	0.01	35	0.02	3	2.5	2.5	5	1.5	0.97	31	5	30
721073	2011	BE-11-06	618	0.618	11	0.79	17.8	0.53	55	7	1.0	1.0	0.78	2.0	4	31	20	2.69	0.10	0.28	308	10	0.01	44	0.10	46	2.5	6	5	8	0.05	20	5	67
553851	2012	BE-12-10	734	0.734	3	0.78	4.1	0.31	67	9	1.0	3.0	0.16	2.0	8	51	15	2.49	0.24	0.12	107	3	0.03	53	0.02	6	2.5	2.5	5	3	0.11	14	5	39
619678	2011	BE-11-03	593	0.593	12	0.78	20.2	0.82	173	6	2.0	22	0.30	2.0	7	43	63	5.22	0.17	0.28	181	34	0.02	61	0.05	21	2.5	6	5	1.5	1.62	24	13	140
159703	2014	BE-14-18	696	0.696	3	0.74	4.2	5.23	182	20	0.9	1.0	0.21	0.8	9	125	12	2.46	0.50	1.17	673	21	0.24	12	0.05	7	11	0.5	69	6	3.39	103	5	54
948535	2012	BE-12-11	662	0.662	2	0.69	3.0	0.18	12	3	1.0	0.5	0.01	2.0	1	15	6	0.48	0.05	0.11	50	57	0.01	20	0.01	5	2.5	2.5	5	1.5	0.30	15	5	9
159222	2014	BE-14-14	626	0.626	3	0.67	4.6	4.37	103	5	0.5	2.0	0.22	0.9	10	124	69	2.95	0.22	1.11	548	3	0.18	18	0.06	8	2.5	0.5	10	3	1.47	167	5	39
619845	2011	BE-11-05	447	0.447	14	0.66	31.3	0.66	74	19	1.0	0.5	0.27	2.0	14	30	20	1.63	0.41	0.05	50	13	0.03	53	0.02	7	2.5	7	5	10	0.93	22	5	24
619694	2011	BE-11-03	578	0.578	4	0.64	6.9	1.90	164	8	2.0	17	0.25	2.0	7	30	92	5.89	0.22	0.98	418	65	0.02	44	0.06	34	2.5	11	5	3	1.20	76	13	104
948616	2012	BE-12-11	608	0.608	1	0.62	0.8	1.02	77	8	1.0	14	0.34	2.0	10	44	12	3.25	0.19	0.91	673	44	0.02	63	0.06	10	2.5	2.5	5	4	0.51	53	5	65
159050	2014	BE-14-13	461	0.461	9	0.60	19.7	5.50	390	5	1.3	4.0	0.26	4.1	15	84	26	4.85	0.17	1.37	1118	47	0.18	15	0.07	11	59	0.5	10	3	1.97	153	5	112
553914	2012	BE-12-10	554	0.554	3	0.60	5.4	0.17	39	3	1.0	0.5	0.22	2.0	2	45	10	1.08	0.11	0.10	109	12	0.01	64	0.02	11	5	6	5	1.5	0.19	10	5	19
553793	2012	BE-12-10	480	0.48	6	0.57	12.5	0.58	131	7	1.0	0.5	0.10	2.0	7	27	13	3.45	0.14	0.49	335	6	0.01	30	0.04	5	2.5	2.5	5	1.5	0.46	63	5	81
721143	2011	BE-11-06	541	0.541	2	0.57	3.7	0.48	44	17	1.0	5.0	0.33	2.0	6	27	12	1.69	0.17	0.27	274	17	0.01	35	0.04	5	2.5	2.5	5	5	0.05	20	5	39
553792	2012	BE-12-10	504	0.504	4	0.57	7.9	0.26	77	7	1.0	0.5	0.04	4.0	4	29	13	1.89	0.12	0.16	50	4	0.01	36	0.02	6	2.5	2.5	5	1.5	0.05	23	5	405
948505	2012	BE-12-11	504	0.504	3	0.55	6.0	1.18	52	7	1.0	0.5	0.14	2.0	9	53	20	2.66	0.14	0.99	832	5	0.03	33	0.03	8	2.5	2.5	5	1.5	0.99	74	5	71
721248	2011	BE-11-07	423	0.423	8	0.55	18.9	0.69	88	8	1.0	0.5	0.84	2.0	14	57	18	3.42	0.11	0.67	528	12	0.01	83	0.11	12	2.5	8	5	22	0.12	53	5	47
948623	2012	BE-12-11	529	0.529	1	0.54	0.9	0.70	133	8	1.0	9.0	0.25	2.0	9	31	16	3.06	0.16	0.73	536	25	0.01	41	0.04	10	2.5	2.5	5	4	0.54	37	5	61
553818	2012	BE-12-10	502	0.502	2	0.53	4.0	0.22	30	3	1.0	0.5	0.08	2.0	3	16	4	0.61	0.08	0.17	122	2	0.01	22	0.01	2	2.5	2.5	5	1.5	0.59	22	5	8
159588	2014	BE-14-17	477	0.477	2	0.51	4.6	3.14	209	12	0.8	4.0	0.15	4.2	8	110	16	3.12	0.46	0.26	114	29	0.25	9	0.02	6	2.5	0.5	10	5	1.83	39	5	60
159664	2014	BE-14-18	441	0.441	4	0.49	7.9	2.84	70	15	0.3	2.0	0.07	1.1	5	195	9	1.23	0.42	0.59	246	220	0.17	11	0.02	5	2.5	0.5	10	4	0.84	61	5	32
553778	2012	BE-12-09	463	0.463	2	0.49	4.3	0.56	50	6	1.0	10	0.25	2.0	10	58	20	2.26	0.26	0.28	265	2	0.06	79	0.05	10	2.5	2.5	5	3	0.75	21	5	49
948806	2012	BE-12-12	422	0.422	3	0.47	7.1	0.89	86	5	1.0	0.5	0.49	2.0	15	55	152	3.50	0.19	0.96	601	34	0.02	59	0.11	15	2.5	2.5	5	4	1.46	61	5	73

Chapter 4: Summary of conclusions and recommendations for future work

4.1 SUMMARY OF KEY CONCLUSIONS.

Based on the observations and results of this research project, a series of conclusions were reached regarding the style, timing, and paleoenvironment of ore mineralization, composition of mineralizing fluids, deportment of gold and silver, and possible geochemical pathfinders in the Big Easy occurrence:

- Big Easy is a well-preserved example of a low-sulfidation epithermal system of Late Neoproterozoic age. It shows most of the features characteristic of this class of ore deposit, including silica sinter formation in the upper parts of the system, high Ag/Au ratios, gold mineralization predominantly deported as electrum, mineral indicators like naumannite, aguilarite, and uytenbogaardtite (suggesting a silver- selenium-rich low-temperature (low sulfidation) environment), veins predominated by quartz ± adularia, mineralizing fluid temperatures from 125 °C to 260 °C (with temperatures as high as 321°C in type IV veins), and salinities below 2.7 wt.% NaCl eq..

- The mineralization of the Big Easy prospect is predominantly hosted in epiclastic sandstones and conglomerates rocks of the Musgravetown Group, rather than the volcaniclastic rocks more typical of the other known epithermal occurrences in the Avalon Zone. We hypothesize that the host rocks are equivalents of the Rocky Harbour Formation of the Musgravetown Group based on the age interpretation of ca. 573Ma (and definitively >566 Ma) for the Big Easy mineralization. This implies a distinctive local tectonic setting

within a broader volcanic arc paleoenvironment of the late Neoproterozoic in the Avalon Zone during the period of peak volcano-plutonic activity at ca 585-570 Ma.

- There is a strong implication (consistent with the model of Feiss et al., 1993) that the peak period for epithermal precious metal deposition in the Late Neoproterozoic, especially in the Burin-Bonavista region (western Avalon Zone), coincided with the incipient re-extension of a host volcanic arc, yielding regionally extensive epiclastic sediments (e.g., Grandy's Pond Arenite Belt) in the flanks of the evolving basin, as well as more localized intracaldera accumulations. Both of these could potentially host epithermal mineralization. Subsequent rapid subsidence to below sea level and consequent rapid accumulation of marine sediments within the submerged extensional basin would further explain the exceptional preservation of the mineralization at Big Easy.

- Mineralization is concentrated within discrete hydrothermal veins that traverse previously silicified/pyritized epiclastic rocks. The mineralization can be classified into four main types of veins, each with a characteristic ore mineral assemblage, suggesting multiple mineralization events. Four different Au- and Ag-bearing vein styles include: Type I) Electrum dominant (High Au) – (electrum, pyrite, sphalerite); Type II) High Au:Ag – (electrum, native silver, acanthite, naumannite, aguilarite, uytenbogaardtite, pyrite); Type III) Ginguro (High Ag:Au) – (native silver, acanthite, aguilarite, freibergite-tetrahedrite, pyrite); and Type IV) Molybdenite-rich (molybdenite, native silver, acanthite).

- Gold is mainly deported as electrum grains, with very minor uytenbogaardtite. These grains are mostly attached to or enclosed within, pyrite crystals in type I and type II veins,

with an average grain size of 1.2 μm. Larger free grains, reaching 30 μm, are found in veins type II and III, but in lesser amounts. The data presented here on gold deportment and texture will be of value for any future geometallurgical assessment.

- Geological and numerical models, geochemical core analysis, vein paragenesis, PCA analysis, and fluid inclusion microthermometry, represent powerful tools for understanding the system's mineralization. Integrated SEM-BSE-EDX, PCA, and numerical modelling analysis allow the understanding of the relationships between potential pathfinder elements and ore mineral assemblages observed in the veins. The negative correlation between Fe-Zn and Au-Ag bearing samples is explained by the pervasive presence of ambient (pre-veining) pyrite throughout the epiclastic host rocks. This pyrite formed before or during the induration of the epiclastic sediments, and before the veins were emplaced in fractures in indurated rocks. The formation of pyrite was accompanied by extensive silicification and produced a large volume indicator envelope for vein mineralization. It thus represents a useful tool for district-scale prospection and exploration. Strong correlations from PCA analysis, Pearson correlation values, numerical modeling, and drill hole graphic log analysis are observed for Mo-As. Halos containing high Mo and As values were identified enveloping Au and Ag mineralized vein areas in the numerical models of drill intersections, and represent a valuable geochemical indicator for future exploration programs.

- Globally, and through time, the tectonic setting for epithermal deposits is diverse, with a combination of physical processes occurring within a variety of very dynamic paleoenvironments. The Big Easy prospect's local tectonic and lithological characteristics

should serve to expand potential exploration targets for other epithermal gold deposits, especially those hosted in non-volcanic rocks, throughout the Avalon Zone.

4.2 RECOMMENDATIONS FOR FUTURE WORK.

Although considerable headway has been gained in the understanding of gold-silver mineralization in the Big Easy prospect, further work is recommended, including:

- Detailed whole-rock lithogeochemistry and Sm-Nd isotope analysis – to compare regional volcanic rocks with the epiclastic sediment lithologies – will help to clarify the more specific volcanic source(s) of the sediments, as well as the timing of deposition and its relationship with the local tectonic setting. The Avalon Zone is a complex terrane, but renewed mapping, and paleoenvironmental reconstruction, using models incorporating the most recent data will further clarify the tectonic evolution of this terrane, and the greater Burin-Bonavista region in particular.

- Structural modeling – perhaps including oriented diamond drilling - that can be tied to the four distinct vein types described in this study, in an attempt to predict their disposition, especially the high Au vein type I. Characterization of regional and local structures may be helpful in delineating the extent of the intracaldera regime proposed in this study as the context for ore mineralization.

- As diamond drilling and/or surface trenching continues, vigilance with respect to possible cross-cutting relationships between the four vein types recognized and described here – in order to establish their relative timing.

- Refinement of geological, numerical, and alteration models, including drill core lithologies and geochemistry from current and future drill programs.